Energy dissipation in photoactive molecular systems: from gas to condensed phase

Miquel Huix-Rotllant

amU
Aix Marseille Université

NNT : 2024AIXM0001

Habilitation à diriger des recherches

Soutenue à AMU — Aix-Marseille Université
le 26 juin 2025 par

Miquel HUIX-ROTLLANT

Energy dissipation in photoactive molecular systems: from gas to condensed phase

Discipline
Sciences Chimiques

Spécialité
Chimie théorique

École doctorale
ED 250 Sciences Chimiques

Laboratoire/Partenaires de recherche
Institut de Chimie Radicalaire

Composition du jury

Aurélien De La Lande Directeur de Recherche	Rapporteur University Paris Saclay
Denis Jacquemin Professeur	Rapporteur University de Nantes
François Maurel Professeur	Rapporteur University Paris Cité
Elise Dumont Professeur	Membre du jury University Côte d'Azur
Maylis Orio Directrice de Recherche	Présidente du jury Aix-Marseille University
Cheol Ho Choi Professeur	Membre invité Kyungpook National University
Nicolas Ferré Professeur	Tuteur Aix-Marseille University

ICR Institut Chimie Radicalaire

cnrs

Contents

Avant-propos

Ce manuscrit présente un aperçu de mon parcours de recherche ainsi que des projets scientifiques financés que j'ai dirigés ou auxquels j'ai contribué depuis ma nomination en tant que chercheur au CNRS en octobre 2015. Il met en lumière mes contributions à la photochimie théorique et décrit les principales orientations de recherche que j'ai suivies au cours de la dernière décennie. De plus, ce manuscrit expose les objectifs scientifiques et les projets que je souhaite explorer dans les années à venir. La plupart des résultats présentés ici ont été publiés dans des revues à comité de lecture ou sont en préparation pour publication.

L'habilitation est structurée en plusieurs sections. La première section inclut mon curriculum vitae, soulignant mon engagement dans le financement de projets, l'encadrement de jeunes chercheurs, l'enseignement ainsi que mes responsabilités administratives. Les sections suivantes offrent des résumés concis des recherches que j'ai menées en tant que chercheur indépendant au sein de mon groupe. Bien que j'aie abordé une variété de sujets, j'ai choisi de me concentrer sur deux axes principaux : la dynamique du croisement intersystème et les processus de redistribution d'énergie responsables des transitions de spin ultrarapides, ainsi que le développement de nouvelles méthodologies pour étudier la réactivité en phase condensée. Enfin, dans la dernière section, je présente mes objectifs de recherche pour l'avenir et les directions scientifiques que je prévois de suivre.

Foreword

This manuscript provides an overview of my research journey and the funded scientific projects I have led or contributed to since my appointment as a CNRS researcher in October 2015. It highlights my contributions to theoretical photochemistry and outlines the key research directions I have pursued over the past decade. Additionally, the manuscript presents the scientific goals and projects I aim to explore in the coming years. Most of the results discussed here have been published in peer-reviewed journals or are in preparation for publication.

The habilitation is structured into several sections. The first section includes my curriculum vitae, emphasizing my involvement in project funding, mentoring young researchers, teaching, and administrative responsibilities. The following sections provide concise synopses of the research I have conducted as an independent investigator within my group. While I have explored a range of topics, I have chosen to focus on two key areas: the dynamics of intersystem crossing and the energy redistribution processes that drive ultrafast spin transitions, as well as the development of new methodologies for studying condensed-phase reactivity. In the final section, I outline my research objectives for the future and the scientific directions I plan to pursue.

1 Curriculum Vitæ

Miquel Huix-Rotllant

Website: huixrotllant.github.io
Email: miquel.huix-rotllant@cnrs.fr
Orcid: 0000-0002-2131-7328
GitHub: github.com/huixrotllant

1.1 Education

Université Joseph Fourier — Grenoble, FR
Ph.D. in Computational Chemistry — 2008–2012
Thesis: *Improved correlation kernels for linear-response time-dependent density-functional theory*

Universitat Rovira i Virgili — Tarragona, CT
M.Sc. in Computational Chemistry — 2006–2008

Universitat de Girona — Girona, CT
B.Sc. in Chemistry — 2002–2006

1.2 Experience

CNRS / Aix-Marseille University — Marseille, FR
Chargé de Recherche/Institut de Chimie Radicalaire — 2015–Now

Göthe Universität Frankfurt — Frankfurt, GE
Humboldt fellow/Institut für Physikalische und Theoretische Chemie — 2014–2015
Topic: *Quantum dynamics of photactive organic semiconductors*

CEA Saclay — Giff sur Yvette, FR
Postdoctorate/Laboratoire Francis Perrin — 2013
Topic: *DNA photodamage by time-resolved fluorescence spectroscopy*

CNRS / Aix-Marseille University — Marseille, FR
Postdoctorate/Institut de Chimie Radicalaire — 2012–2013
Topic: *Theoretical study of radical photopolymerization*

1.3 Mentoring

Post-doctorant fellows

20. Dr. Ellena Black • ANR MAPPLE (2025-2026)
19. Dr. Renato Dias da Cunha • ANR MAPPLE (2025-2026)
18. Dr. Simone Bonfrate • ANR ULTRARCHEA (2025)
17. Dr. Thomas Fay • ANR MAPPLE (2024-2025)
16. Dr. Darío Barreiro Laje • ANR ULTRARCHEA (2023-2024)
15. Dr. Gustavo Adolfo Cárdenas • ANR ULTRARCHEA (2022-2023)
14. Dr. Marc Alías Rodríguez • ANR MULTICROSS (2022-2024)
13. Dr. Swarnendu Bhattacharyya • ANR MULTICROSS (2021-2022)
12. Dr. Padmabati Mondal • ANR BIOMAGNET (2017-2018)

Ph.D. students

11. Ms. Isabel Eder • MESRI • Co-Director: Nicolas Ferré (2024-2027)
10. Mr. Woojin Park • NSF Korea • Exchange program. Director: Cheol Ho Choi (2024)
9. Mr. Simone Bonfrate • MESRI • Co-director: Nicolas Ferré (2021-2024)
8. Mr. Karno Schwinn • ANR BIOMAGNET • Co-director: Nicolas Ferré (2017-2020)

Master students

7. Ms. Anis Abdelbari • Master 2, Aix-Marseille Université (2025)
6. Ms. Abdul Qadeer • Master 2, University of Valencia (2025)
5. Ms. Dulce Trejo • Master 1, University of Toulouse (2024)
4. Ms. Yvonne Kettler • Master 2, Goethe University Frankfurt (2015)
3. Mr. Karno Schwinn • Master 2, Goethe University Frankfurt (2015)

Bachelor students

2. Mr. Omar Guireev • Licence 2, Aix-Marseille Université (2024)
1. Ms. Johanna Guazelli • Licence 3, Aix-Marseille Université (2022)

1.4 Research Grants

1. **ANR-PRCi FEMTO-Switch** (Role: partner) 2024 – 2026
   A Combined Theoretical and Experimental Study of FEMTOsecond Biomimetic Photo-SWITCHes – Towards Rational Design Principles
2. **ANR-PRC MAPPLE** ANR-22-CE29-0014 (Role: partner) 2022 – 2026
   MAssively Parallelized Polarizable Linear-scaling QM/MM for Enzymatic catalysis
3. **ANR-PRCi ULTRArchea** ANR-21-CE11-0029 (Role: participant) 2021 – 2025
   Ultrafast structural dynamics of Archaerhodopsin-3 in its fluorescent state

4. **Région Sud - A*Midex** (Role: coordinator) 2022 – 2023
   Quantum computing with organic radicals
5. **PHC Star** (Role: coordinator) 2019 – 2021
   New density functional based methods for excited states
6. **ANR-PRCi Multicross** ANR-19-CE29-0018 (Role: partner) 2017 – 2021
   Multiple trajectories towards excited states
7. **ANR-JCJC Biomagnet** ANR-16-CE29-0008 (Role: coordinator) 2017 – 2021
   On the quest of a biological compass: magnetic field effects on the cryptochrome protein

1.5 Teaching

1. Density functional theory for excited states (2h Course + 2h TP) (2025)
2. Dynamics in the excited states (2h Course + 2h TP) (2024)
3. Dynamics in the excited states (2h Course) (2022)
4. Density functional theory for excited states (2h Course) (2021)
5. Density functional theory for excited states (2h Course) (2020)

1.6 Scientific event organization

1. Perspectives “Moyens de Calcul” – 50 participants – Organizer (2 days, Marseille, 2025)
2. Theoretical chemistry for Atmospheric Chemistry – 50 participants – Organizer (2 days, Marseille, 2025)
3. Plenary days GDR XFEL – 50 participants – Organizer (2 days, Marseille, 2024)
4. Theory around XFEL – 50 participants – Organizer (3 days, Marseille, 2024)
5. Quantum chemistry for high-performance computing – 20 participants – Organizer (1 days, Marseille, 2024)
6. Excited States: Bridging Scales – 50 participants – Organizer (3 days, Marseille, 2016)

1.7 Scientific and Administrative activities

- Member of the Laboratory Council at the Institute of Radical Chemistry (2019-Now).
- Board member of the GDR XFEL (2023-Now).
- Board member of the GDR Thémosia (2024-Now).
- Selection Comitte MCF (iSm2 - Theory) May 2022
- Thesis jury - Enzo Monino - (University of Toulouse) 2023
- Thesis jury - Marc Alías-Rodríguez - (University Rovira i Virgili) 2018
- Thesis jury - Claudia Climent - (University of Barcelona) 2016
- Reviewer: (JACS, JCTC, JCP, Chem. Sci., Nat. Comm., JPC, ChemPhysChem, etc.)
- Funding reviewer: (ANR, ERC, etc.)

1.8 Communications

Oral communications

- *Theoretical insights in the photophysical mechanism of thymine from the eyes of time-resolved X-ray spectroscopy* Plenary days GDR XFEL (Marseille, 2024)
- *Theoretical chemistry insights on photoreactivity of organic molecules studied at ICR* ICR Scientific day (Marseille, 2024)
- *Quantum dynamics of intersystem crossing* Perspective on Exited States Thémosia (Nantes, 2024)
- *Quantum dynamics of intersystem crossing* ESPA (Tarragona, 2024)
- *Coherent photolysis of carbon monoxide in myoglobin* Group Seminar (Marseille, 2024)
- *Coherent photolysis of carbon monoxide in myoglobin* French BIC (Marseille, 2024)
- *Accurate time-resolved X-ray spectroscopy from mixed-reference spin-flip TDDFT* Thémosia Sud-Est (Lyon, 2024)
- *Coherent photolysis of carbon monoxide in myoglobin* Theory around XFEL (Marseille, 2024)
- *Electrostatic potential fitted multipoles for efficient QM/MM embedding* Workshop "HPC for quantum chemistry" (Marseille, 2024)
- *Electrostatic embedding QM/MM in periodic boundary conditions* 11th OpenMolcas (Bologna, 2023)
- *GAMESS-US/Tinker interface* Sorbonne University (Paris, 2023)
- *Photolyse du monoxyde de carbone dans la myoglobine* CNRS Campus Michel-Ange (Paris, 2023)
- *Photochemistry of FeII(bpy)3 via wavepacket dynamics* NHISS (Jeju, 2022)
- *Time-resolved X-ray absorption with spin-flip TDDFT* Plenary days GDR XFEL (Paris, 2022)
- *Ultrafast intersystem crossing in xanthone from wavepacket dynamics* NHISS (Jeju, 2021)
- *Laboratoire de Chimie Théorique Institut de Chimie Radicalaire* Journées des Théoriciens (Marseille, 2021)
- *Advances in ESPF QM/MM methodology for excited states* Computational Photochemistry (online, 2021)
- *Le rôle principal des vibrations moléculaires dans les protéines photoactives* Journées des CR (Marseille, 2021)
- *On-the-fly excited state dynamics in complex media* CECAM Solvent (online, 2021)

- *Efficient analytic hessian of electrostatic embedding QM/MM*
  Universitat Rovira i Virgili (Tarragona, 2020)
- *Linear scaling electrostatic embedding QM/MM based on electrostatic potential fitted atomic charges*
  NHISS (online, 2020)
- *Analytic Hessians of QM/MM ESPF*
  10th OpenMolcas (online, 2020)
- *Advances in electrostatic embedding QM/MM using electrostatic potential fitted charges*
  Group Meeting (Marseille, 2020)
- *Linear scaling electrostatic embedding QM/MM based on electrostatic potential fitted atomic charges*
  Journées "Théorie, Modélisation et Simulation" (online, 2020)
- *DFT for excited states: Progress in LR-TDDFT*
  GDR N-Body (Lille, 2020)
- *Charge derivatives with QM/MM ESPF method*
  University of Siena (Siena, 2019)
- *Ultrafast heme-CO photolysis and spin crossover via nonadiabatic quantum dynamics*
  Quantum BioInorganic Chemistry (Marseille, 2019)
- *Recent advances on analytic charge derivatives of QM/MM ESPF method*
  Perspectives RCTF (Nantes, 2019)
- *Ultrafast carbon monoxide photolysis and heme spin-crossover in myoglobin via nonadiabatic quantum dynamics*
  Kyungpook State University (Daegu, 2019)
- *Ultrafast carbon monoxide photolysis and heme spin-crossover in myoglobin via nonadiabatic quantum dynamics*
  Conference Light and Molecules (Marseille, 2019)
- *Wavepacket dynamics for organometallic complexes*
  ANR Multicross (Rennes, 2019)

1.9 Publications

Submitted articles

65. Miquel Huix-Rotllant, Woojin Park, and Cheol Ho Choi. “Assessing Spin-flip Time-Dependent Density-Functional Based Tight-Binding For Describing Photoisomerisation Reactions”. In: *Theoretical Chemistry Accounts* (2025).

64. Simone Bonfrate, Woojin Park, Dulce Trejo-Zamora, Cheol Ho Ferré Nicolas Choi, and Miquel Huix-Rotllant. “Assessment of free energies from electrostatic embedding density functional tight binding-based/molecular mechanics in periodic boundary conditions”. In: *Journal of Computational Chemistry* (2025).

Accepted articles

63. Woojin Park, Seunghoon Lee, Konstantin Komarov, Vladimir Mironov, Hiroya Nakata, et al. "MRSF-TDDFT: A New Tool in Quantum Chemistry for Better Understanding Molecules and Materials". In: *Bulletin of the Korean Chemical Society* (2025). DOI: 10.1002/bkcs.70011.

62. Thomas Fay, Nicolas Ferré, and Miquel Huix-Rotllant. "Efficient Polarizable QM/MM Using the Direct Reaction Field Hamiltonian with Electrostatic Potential Fitted Multipole Operators". In: *J. Chem. Theory Comput.* (2024). DOI: 10.1021/acs.jctc.4c01219.

61. Darío Barreiro-Lage, Vincent Ledentu, Jacopo D'Ascenzi, Miquel Huix-Rotllant, and Nicolas Ferré. "Investigating the origin of Automatic Rhodopsin Modeling outliers using the microbial *Gloeobacter* rhodopsin as testbed". In: *J. Phys. Chem. B* 128 (2024), pp. 12368–12378. DOI: 10.1021/acs.jpcb.4c05962.

60. Vladimir Mironov, Konstantin Komarov, Jingbai Li, Igor Gerasimov, Hiroya Nakata, et al. "OpenQP: A Quantum Chemical Platform Featuring MRSF-TDDFT with an Emphasis on Open-Source Ecosystem". In: *J. Chem. Theor. Comput.* 20 (2024), pp. 9464–9477. DOI: 10.1021/acs.jctc.4c01117.

59. Woojin Park, Juwon Oh, Jinseok Kim, Seunghoon Lee, Ji Heon Kim, et al. "Temperature Controlled Decay and Pendulum Dynamics of Green Fluorescent Protein (GFP) Chromophore". In: *J. Chem. Phys. Lett.* 15 (2024), pp. 11468–11475. DOI: 10.1021/acs.jpclett.4c02761.

58. Arona Fall, Guillaume Tintori, Marion Rollet, Yuxi Zhao, Miquel Huix-Rotllant, et al. "α-Trifluoromethylated quinolines as air-stable and safe PET-donor for radical polymerizations". In: *Macromol. Rapid Commun.* (2024). DOI: 10.1002/marc.202400710.

57. W. Park, A. Lashakripour, K. Komarov, S. Lee, M. Huix-Rotllant, et al. "Toward Consistent Predictions of Core/Valence Ionization Potentials and Valence Excitation Energies by MRSF-TDDFT". in: *Journal of Chemical Theory and Computation* 20 (2024), pp. 5679–5694. DOI: 10.1021/acs.jctc.4c00640.

56. Marc Alías-Rodríguez and Miquel Huix-Rotllant. "Control of the iron-tris(2,2-bipyridine) light-induced excited-state trapping via external electromagnetic fields". In: *ChemPhysChem* 25 (2024), e202400471. DOI: 10.1002/cphc.202400471.

55. Simone Bonfrate, Nicolas Ferré, and Miquel Huix-Rotllant. "Analytic gradients for the electrostatic embedding QM/MM in periodic boundary conditions using particle-mesh Ewald sums and electrostatic potential fitted charge operators". In: *Journal of Chemical Theory and Computation* 20 (2024), pp. 4338–4349. DOI: 10.1021/acs.jctc.4c00201.

54. Thomas R.M. Barends, Swarnendu Bhattacharyya, Alexander Gorel, Giorgio Schiro, Camila Bacellar, et al. "Influence of pump laser fluence on ultrafast structural changes in myoglobin". In: *Nature* 626 (2024), pp. 905–911. DOI: 10.1038/s41586-024-07032-9.

53. Elisa Pieri, Oliver Weingart, Miquel Huix-Rotllant, Vincent Ledentu, Marco Garavelli, et al. "Modeling pH-Dependent Biomolecular Photochemistry". In: *Journal of Chemical Theory and Computation* 20.2 (2024), pp. 842–855. DOI: 10.1021/acs.jctc.3c00980.

52. J. M. González-Sánchez, M. Huix-Rotllant, N. Brun, J. Morin, C. Demelas, et al. "Direct formation of HONO through aqueous-phase photolysis of organic nitrates". In: *Atmospheric Chemistry and Physics* 23.23 (2023), pp. 15135–15147. DOI: 10.5194/acp-23-15135-2023.

51. Leonardo Barneschi, Emanuele Marsili, Laura Pedraza-González, Daniele Padula, Luca De Vico, et al. "Assessment of the Electron Correlation Treatment on the Quantum-Classical Dynamics of Retinal Protonated Schiff Base Models: XMS-CASPT2, RMS-CASPT2, and REKS Methods". In: *Journal of Chemical Theory and Computation* 19.22 (2023), pp. 8189–8200. DOI: 10.1021/acs.jctc.3c00879.

50. Konstantin Komarov, Woojin Park, Seunghoon Lee, Miquel Huix-Rotllant, and Cheol Ho Choi. "Doubly Tuned Exchange–Correlation Functionals for Mixed-Reference Spin-Flip Time-Dependent Density Functional Theory". In: *Journal of Chemical Theory and Computation* 19.21 (2023), pp. 7671–7684. DOI: 10.1021/acs.jctc.3c00884.

49. Gustavo Cárdenas, Vincent Ledentu, Miquel Huix-Rotllant, Massimo Olivucci, and Nicolas Ferré. "Automatic Rhodopsin Modeling with Multiple Protonation Microstates". In: *The Journal of Physical Chemistry A* 127 (2023), pp. 9365–9380. DOI: 10.1021/acs.jpca.3c05413.

48. Marc Alías-Rodríguez, Simone Bonfrate, Woojin Park, Nicolas Ferré, Cheol Ho Choi, et al. "Solvent Effects and pH Dependence of the X-ray Absorption Spectra of Proline from Electrostatic Embedding Quantum Mechanics / Molecular Mechanics and Mixed-Reference Spin-Flip Time-dependent Density-Functional Theory". In: *The Journal of Physical Chemistry A* 127 (2023), pp. 10382–10392. DOI: 10.1021/acs.jpca.3c05070.

47. Marc Alías-Rodríguez, Swarnendu Bhattacharyya, and Miquel Huix-Rotllant. "Ultrafast Spin Crossover Photochemical Mechanism in $[Fe^{II}(2,2\prime\text{-bipyridine})_3]^{2+}$ Revealed by Quantum Dynamics". In: *The Journal of Physical Chemistry Letters* (2023), pp. 8571–8576. DOI: 10.1021/acs.jpclett.3c02201.

46. Giovanni Li Manni, Ignacio Fdez. Galván, Ali Alavi, Flavia Aleotti, Francesco Aquilante, et al. "The OpenMolcas *Web*: A Community-Driven Approach to Advancing Computational Chemistry". In: *Journal of Chemical Theory and Computation* (2023). DOI: 10.1021/acs.jctc.3c00182.

45. Simone Bonfrate, Nicolas Ferré, and Miquel Huix-Rotllant. "An efficient electrostatic embedding QM/MM method using periodic boundary conditions based on particle-mesh Ewald sums and electrostatic potential fitted charge operators". In: *The Journal of Chemical Physics* 158.2 (2023). DOI: 10.1063/5.0133646.

44. Miquel Huix-Rotllant, Karno Schwinn, Vladimir Pomogaev, Maryam Farmani, Nicolas Ferré, et al. "Photochemistry of Thymine in Solution and DNA Revealed by an Electrostatic Embedding QM/MM Combined with Mixed-Reference Spin-Flip TDDFT". in: *Journal of Chemical Theory and Computation* 19.1 (2022), pp. 147–156. DOI: 10.1021/acs.jctc.2c01010.

43. Michael Filatov, Marco Paolino, Robin Pierron, Andrea Cappelli, Gianluca Giorgi, et al. "On the fluorescence enhancement of arch neuronal optogenetic reporters". In: *Nature Communications* 13.1 (2022). DOI: 10.1038/s41467-022-33993-4.

42. Michael Filatov, Marco Paolino, Robin Pierron, Andrea Cappelli, Gianluca Giorgi, et al. "Towards the engineering of a photon-only two-stroke rotary molecular motor". In: *Nature Communications* 13.1 (2022). DOI: 10.1038/s41467-022-33695-x.

41. Woojin Park, Marc Alías-Rodríguez, Daeheum Cho, Seunghoon Lee, Miquel Huix-Rotllant, et al. "Mixed-Reference Spin-Flip Time-Dependent Density Functional Theory for Accurate X-ray Absorption Spectroscopy". In: *Journal of Chemical Theory and Computation* 18.10 (2022), pp. 6240–6250. DOI: 10.1021/acs.jctc.2c00746.

40. Roger-Charles Tissier, Baptiste Rigaud, Pierre Thureau, Miquel Huix-Rotllant, Maguy Jaber, et al. "Stressing the differences in alizarin and purpurin dyes through UV-visible light absorption and ^{1}H-NMR spectroscopies". In: *Physical Chemistry Chemical Physics* (2022). DOI: 10.1039/d2cp00520d.

39. Marc Alías-Rodríguez, Miquel Huix-Rotllant, and Coen de Graaf. "Quantum dynamics simulations of the thermal and light-induced high-spin to low-spin relaxation in $Fe(bpy)_3$ and $Fe(mtz)_6$". In: *Faraday Discussions* (2022). DOI: 10.1039/d2fd00027j.

38. Marc Alías-Rodríguez, Coen de Graaf, and Miquel Huix-Rotllant. "Ultrafast Intersystem Crossing in Xanthone from Wavepacket Dynamics". In: *Journal of the American Chemical Society* 143.51 (2021), pp. 21474–21477. DOI: 10.1021/jacs.1c07039.

37. Miquel Huix-Rotllant. "Photochemistry of Thymine in Protic Polar Nanomeric Droplets Using Electrostatic Embeding TD-DFT/MM". in: *Molecules* 26.19 (2021). ISSN: 1420-3049. DOI: 10.3390/molecules26196021.

36. Woojin Park, Seunghoon Lee, Miquel Huix-Rotllant, Michael Filatov, and Cheol Ho Choi. "Impact of the Dynamic Electron Correlation on the Unusually Long Excited-State Lifetime of Thymine". In: *The Journal of Physical Chemistry Letters* 12.18 (2021), pp. 4339–4346. DOI: 10.1021/acs.jpclett.1c00712.

35. Miquel Huix-Rotllant, Karno Schwinn, and Nicolas Ferr'e. "Infrared spectroscopy from electrostatic embedding QM/MM: local normal mode analysis of infrared spectra of arabidopsis thaliana plant cryptochrome". In: *Phys. Chem. Chem. Phys.* 23 (2021), pp. 1666–1674. DOI: 10.1039/D0CP06070D.

34. Miquel Huix-Rotllant and Nicolas Ferré. "Analytic Energy, Gradient, and Hessian of Electrostatic Embedding QM/MM Based on Electrostatic Potential-Fitted Atomic Charges Scaling Linearly with the MM Subsystem Size". In: *J. Chem. Theory Comput.* 17.1 (2021), pp. 538–548.

33. Padmabati Mondal, Karno Schwinn, and Miquel Huix-Rotllant. "Impact of the redox state of flavin chromophores on the UV–vis spectra, redox and acidity constants and electron affinities". In: *Journal of Photochemistry and Photobiology A: Chemistry* 387 (2020), p. 112164. ISSN: 1010-6030. DOI: https://doi.org/10.1016/j.jphotochem.2019.112164.

32. Karno Schwinn, Nicolas Ferré, and Miquel Huix-Rotllant. "Efficient Analytic Second Derivative of Electrostatic Embedding QM/MM Energy: Normal Mode Analysis of Plant Cryptochrome". In: *Journal of Chemical Theory and Computation* 16.6 (2020), pp. 3816–3824. DOI: 10.1021/acs.jctc.9b01145.

31. Karno Schwinn, Nicolas Ferré, and Miquel Huix-Rotllant. "Efficient Analytic Second Derivative of Electrostatic Embedding QM/MM Energy: Normal Mode Analysis of Plant Cryptochrome". In: *J. Chem. Theory Comput.* 16 (2020), pp. 3816–3824.

30. Karno Schwinn, Nicolas Ferré, and Miquel Huix-Rotllant. "Analytic QM/MM atomic charge derivatives avoiding the scaling of coupled perturbed equations with the MM subsystem size". In: *J. Chem. Phys.* 151 (2019), p. 041102. DOI: 10.1063/1.5115125.

29. Padmabati Mondal and Miquel Huix-Rotllant. "Theoretical insights into the formation and stability of radical oxygen species in cryptochrome". In: *Phys. Chem. Chem. Phys.* (2019), pp. 8874–8882. DOI: 10.1039/C9CP00782B.

28. Elisa Pieri, Vincent Ledentu, Miquel Huix-Rotllant, and Nicolas Ferr'e. "Sampling the protonation states: the pH-dependent UV absorption spectrum of a polypeptide dyad". In: *Phys. Chem. Chem. Phys.* 20 (2018), pp. 23252–23261. DOI: 10.1039/C8CP03557A.

27. Konstantin Falahati, Hiroyuki Tamura, Irene Burghardt, and Miquel Huix-Rotllant. "Ultrafast carbon monoxide photolysis and heme spin-crossover in myoglobin via nonadiabatic quantum dynamics". In: *Nature Communications* 9.1 (2018). DOI: 10.1038/s41467-018-06615-1.

26. Konstantin Falahati, Hiroyuki Tamura, Irene Burghardt, and Miquel Huix-Rotllant. "Ultrafast Carbon Monoxide Photolysis and Heme Spin-crossover in Myoglobin via Nonadiabatic Quantum Dynamics". In: *Nat. Comm.* 9 (2018), p. 4502.

25. Ignacio Vayá, Johanna Brazard, Miquel Huix-Rotllant, Arun K. Thazhathveetil, Frederick D. Lewis, et al. "High-Energy Long-Lived Mixed Frenkel–Charge-Transfer Excitons: From Double Stranded $(AT)_n$ to Natural DNA". in: *Chemistry – A European Journal* 22.14 (2016), pp. 4904–4914. DOI: 10.1002/chem.201504007.

24. Miquel Huix-Rotllant, Irene Burghardt, and Nicolas Ferré. "Population of triplet states in acetophenone: A quantum dynamics perspective". In: *Comptes Rendus Chimie* 19.1-2 (2016), pp. 50–56. DOI: 10.1016/j.crci.2015.10.002.

23. Miquel Huix-Rotllant, Irene Burghardt, and Nicolas Ferré. "Population of triplet states in acetophenone: A quantum dynamics perspective". In: *Comptes Rendus Chimie* 19 (2016), pp. 50–56.

22. Hiroyuki Tamura, Miquel Huix-Rotllant, Irene Burghardt, Yoann Olivier, and David Beljonne. "First-Principles Quantum Dynamics of Singlet Fission: Coherent versus Thermally Activated Mechanisms Governed by Molecular π Stacking". In: *Physical Review Letters* 115.10 (2015). DOI: 10.1103/physrevlett.115.107401.

21. Miquel Huix-Rotllant, Hiroyuki Tamura, and Irene Burghardt. "Concurrent Effects of Delocalization and Internal Conversion Tune Charge Separation at Regioregular Polythiophene-Fullerene Heterojunctions". In: *The Journal of Physical Chemistry Letters* 6.9 (2015), pp. 1702–1708. DOI: 10.1021/acs.jpclett.5b00336.

20. Miquel Huix-Rotllant, Johanna Brazard, Roberto Improta, Irene Burghardt, and Dimitra Markovitsi. "Stabilization of Mixed Frenkel-Charge Transfer Excitons Extended Across Both Strands of Guanine-Cytosine DNA Duplexes". In: *The Journal of Physical Chemistry Letters* 6.12 (2015), pp. 2247–2251. DOI: 10.1021/acs.jpclett.5b00813.

19. Michael Filatov, Miquel Huix-Rotllant, and Irene Burghardt. "Ensemble density functional theory method correctly describes bond dissociation, excited state electron transfer, and double excitations". In: *The Journal of Chemical Physics* 142.18 (2015). DOI: 10.1063/1.4919773.

18. Miquel Huix-Rotllant and Nicolas Ferré. "Triplet state photochemistry and the three-state crossing of acetophenone within time-dependent density-functional theory". In: *The Journal of Chemical Physics* 140.13 (2014). DOI: 10.1063/1.4869802.

17. Miquel Huix-Rotllant and Nicolas Ferré. "Theoretical Study of the Photochemical Initiation in Nitroxide-Mediated Photopolymerization". In: *The Journal of Physical Chemistry A* 118.25 (2014), pp. 4464–4470. DOI: 10.1021/jp501773n.

16. Miquel Huix-Rotllant, Elise Dumont, Nicolas Ferré, and Antonio Monari. "Photophysics of Acetophenone Interacting with DNA: Why the Road to Photosensitization is Open". In: *Photochemistry and Photobiology* 91.2 (2014), pp. 323–330. DOI: 10.1111/php.12395.

15. Alexander Nikiforov, Jose A. Gamez, Walter Thiel, Miquel Huix-Rotllant, and Michael Filatov. "Assessment of approximate computational methods for conical intersections and branching plane vectors in organic molecules". In: *The Journal of Chemical Physics* 141.12 (2014). DOI: 10.1063/1.4896372.

14. Samer Gozem, Federico Melaccio, Alessio Valentini, Michael Filatov, Miquel Huix-Rotllant, et al. "Shape of Multireference, Equation-of-Motion Coupled-Cluster, and Density Functional Theory Potential Energy Surfaces at a Conical Intersection". In: *Journal of Chemical Theory and Computation* 10.8 (2014), pp. 3074–3084. DOI: 10.1021/ct500154k.

13. Michael Filatov and Miquel Huix-Rotllant. "Assessment of density functional theory based ΔSCF (self-consistent field) and linear response methods for longest wavelength excited states of extended π-conjugated molecular systems". In: *The Journal of Chemical Physics* 141.2 (2014). DOI: 10.1063/1.4887087.

12. Miquel Huix-Rotllant, Michael Filatov, Samer Gozem, Igor Schapiro, Massimo Olivucci, et al. "Assessment of Density Functional Theory for Describing the Correlation Effects on the Ground and Excited State Potential Energy Surfaces of a Retinal Chromophore Model". In: *Journal of Chemical Theory and Computation* 9.9 (2013), pp. 3917–3932. DOI: 10.1021/ct4003465.

11. Miquel Huix-Rotllant, Didier Siri, and Nicolas Ferré. "Theoretical study of the photochemical generation of triplet acetophenone". In: *Physical Chemistry Chemical Physics* 15.44 (2013), p. 19293. DOI: 10.1039/c3cp52703d.

10. M.E. Casida and M. Huix-Rotllant. "Progress in Time-Dependent Density-Functional Theory". In: *Annual Review of Physical Chemistry* 63.1 (2012), pp. 287–323. DOI: 10.1146/annurev-physchem-032511-143803.

9. Miquel Huix-Rotllant, Andrei Ipatov, Angel Rubio, and Mark E. Casida. "Assessment of dressed time-dependent density-functional theory for the low-lying valence states of 28 organic chromophores". In: *Chemical Physics* 391.1 (2011), pp. 120–129. DOI: 10.1016/j.chemphys.2011.03.019.

8. Miquel Huix-Rotllant, Bhaarathi Natarajan, Andrei Ipatov, C. Muhavini Wawire, Thierry Deutsch, et al. "Assessment of noncollinear spin-flip Tamm–Dancoff approximation time-dependent density-functional theory for the photochemical ring-opening of oxirane". In: *Physical Chemistry Chemical Physics* 12.39 (2010), p. 12811. DOI: 10.1039/c0cp00273a.

7. Miquel Huix-Rotllant, Ajanta Deka, Alexei V. Matveev, Sergey I. Bosko, Lyudmila V. Moskaleva, et al. "Characterization of optical spectra of interacting systems: Application to oxide-supported metal clusters". In: *International Journal of Quantum Chemistry* 108.15 (2008), pp. 2978–2990. DOI: 10.1002/qua.21853.

6. Sean Bonness, Bernard Kirtman, Miquel Huix, Angel J. Sanchez, and Josep M. Luis. "Simulation of photoelectron spectra with anharmonicity fully included: Application to the $\tilde{X}A_2^2 \leftarrow \tilde{X}A_1^1$ band of furan". In: *The Journal of Chemical Physics* 125.1 (2006). DOI: 10.1063/1.2210479.

Book chapters

5. Seunghoon Lee, Miquel Huix-Rotllant, and Cheol Ho Choi. "Time-dependent DFT: development of TDDFT, applications, and future perspectives". In: ed. by Aleksey Kuznetsov. Density Functional Theory. Elsevier, 2025. Chap. 3.

4. Miquel Huix-Rotllant, Nicolas Ferré, and Mario Barbatti. "Time-Dependent Density Functional Theory: From Fundamentals to Non-adiabatic Dynamics". In: ed. by Leticia González and Roland Lindh. Quantum Chemistry and Dynamics of Excited States: Methods and Applications. Wiley, 2020. Chap. 2, pp. 13–46. DOI: 10.1002/9781119417774.ch2.

3. Miquel Huix-Rotllant, Alexander Nikiforov, Walter Thiel, and Michael Filatov. "Description of Conical Intersections with Density Functional Methods". In: Density-Functional Methods for Excited States. Springer International Publishing, 2015, pp. 445–476. DOI: 10.1007/128_2015_631.

2. Mark E. Casida and Miquel Huix-Rotllant. “Many-Body Perturbation Theory (MBPT) and Time-Dependent Density-Functional Theory (TD-DFT): MBPT Insights About What Is Missing In, and Corrections To, the TD-DFT Adiabatic Approximation”. In: Density-Functional Methods for Excited States. Springer International Publishing, 2015, pp. 1–60. DOI: 10.1007/128_2015_632.

Book edition

1. Nicolas Ferré, Michael Filatov, and Miquel Huix-Rotllant, eds. *Density-Functional Methods for Excited States*. Springer International Publishing, 2016. DOI: 10.1007/978-3-319-22081-9.

2 Research works

Table of Contents

2.1 Quantum dynamics of intersystem crossing

2.1.1 Introduction

In this first set of examples of my work, I focused on the description of intersystem crossing (ISC), a radiationless transition between electronic states of different total spin multiplicity.[1] In intersystem crossings, vibrations can play a major role. The coupling between different multiplicities is a spin-forbidden transition, absent in the approximate molecular Hamiltonian including non-relativistic time-independent Born-Oppenheimer approximation frequently used in quantum chemistry.[2] In the following works, we include the spin-orbit (SO) interaction via the Breit-Pauli Hamiltonian, which is the simplest way of including such relativistic effects.[3]

Intersystem crossing transitions are usually slow process (nanosecond to millisecond), but can be accelerated to the ultrafast regime (femtosecond to picosecond) due to the coupling with vibrations.[4] In essence, the first order kinetic rate of intersystem crossing between a singlet (S) and a triplet (T) is given by the simple Fermi's Golden Rule formula,[5]

$$k_{ST}^{1} = \frac{2\pi}{\hbar} \left| \langle \Psi_S | \hat{H}_{SO} | \Psi_T \rangle \right|^2 \delta \left(E_T - E_S \right) \tag{2.1}$$

in which $\hat{H}_{SO}$ is the spin-orbit Hamiltonian, and Ψ_S and Ψ_T the electronic wavefunctions of the singlet and triplet states. This rate is directly proportional to the strength of the spin-orbit coupling, following thus the El-Sayed's rule.[6] In the literature, several groups have reported vibronic spin-orbit effects, that would not only allow El-Sayed's forbidden transitions, but also accelerate spin-orbit coupling to an ultrafast regime.[7] The vibronic spin-orbit transitions were computed with first-order Fermi golden rule, invoking a Herzberg-Teller-like mechanism of vibronic spin-orbit. In essence, in the first-order

formula one can include a Taylor expansion of the spin-orbit Hamiltonian,

$$\hat{H}_{SO}(R) = \hat{H}_{SO}(R_0) + \sum_i \frac{\partial \hat{H}_{SO}(R)}{\partial R_i} (R_i - R_0) + \cdots, \tag{2.2}$$

that could in principle accelerate the spin-orbit coupling. These derivative can be computed analytically in the Breit-Pauli Hamiltonian, which contains only a one-electron spin-orbit term that explicitly depends on the nuclear coordinates,

$$H_{el}^{SO} = \frac{\hbar e^2}{2m_e^2 c^2} \sum_i^{N_{el}} \hat{s}_i \cdot \sum_A^{N_{nuc}} \frac{Z_A(\mathbf{r}_i - \mathbf{R}_A) \times \hat{p}_i}{|\mathbf{r}_i - \mathbf{R}_A|^3}. \tag{2.3}$$

In the literature, these derivatives were computed numerically directly applied to the matrix elements of the spin-orbit coupling. This introduces extra terms in the Taylor expansion due to the derivative of adiabatic wavefunctions, which can mix wavefunctions and accelerate the spin-orbit coupling to unrealistic ultrafast regime. The electronic first-order kinetic rate is the same as in Eq. 2.1. The vibronic spin-orbit coupling can be then obtained as a second-order kinetic rate considering,

$$k_{ST}^2 = \frac{2\pi}{\hbar} \left| \sum_{T' \neq T} \frac{\langle \Psi_S | \hat{H}_{SO} | \Psi_{T'} \rangle \langle \Psi_{T'} | \hat{H}_{NAC} | \Psi_T \rangle}{E_{T'} - E_S} \right|^2 \delta(E_T - E_S) \tag{2.4}$$

$$+ \frac{2\pi}{\hbar} \left| \sum_{S' \neq S} \frac{\langle \Psi_S | \hat{H}_{NAC} | \Psi_{S'} \rangle \langle \Psi_{S'} | \hat{H}_{SOC} | \Psi_T \rangle}{E_{S'} - E_S} \right|^2 \delta(E_T - E_S) \tag{2.5}$$

$$\tag{2.6}$$

in which the sum over index T' and S' runs over states of triplet and singlet multiplicity states respectively. In this formula, forbidden spin-orbit transitions ($\langle \Psi_S | \hat{H}^{SOC} | \Psi_T \rangle = 0$) from a singlet initial state S to a triplet final state T could become allowed by the presence of intermediate triplet states T' that have simultaneously a strong SO and a strong NAC with the initial singlet and the final triplet respectively, and the intermediate singlet states S' that have simultaneously a strong NAC and a strong SO with the initial singlet and final state respectively.

Vibronic rate theory was extensively used in the literature to compute intersystem crossing rates of many photochemical processes like intersystem crossing, delayed fluorescence, etc.[8–12] However, it is arguable that rate theory is valid for ultrafast vibronic intersystem crossing processes, in which non-equilibrium effects are important. A most robust approach is the real-time propagation of nuclear wavepackets on potential energy surfaces defined by vibronic Hamiltonians containing non-adiabatic and spin-orbit couplings. This is has the advantage that is non-perturbative, considering thus all non-equilibrium effects and couplings of any strength. In a series of studies, I extended linear vibronic coupling model Hamiltonians to describe spin-orbit coupling, giving detailed mechanistic origin of ultrafast intersystem crossing in organic and organometallic complexes.[13–19] In the following, I will describe briefly the methodology and main results of such studies.

2.1.2 Methodology

Multi-configuration time-dependent Hartree (MCTDH) method is an efficient way of solving the time-resolved Schrödinger equation for a nuclear wavepacket. The method has been lengthy discussed in the literature[20] and only a brief explanation will be given here. MCTDH is based on the following wave function *Ansatz* to solve the time-dependent Schrödinger equation.

$$\Psi(q_1, ..., q_f, t) = \sum_J A_J(t) \Phi_J(q_1, ..., q_f, t) \tag{2.7}$$

where f are the degrees of freedom for the system, J is a composite index $J = j_1 ... j_f$, A_J are the time-dependent coefficients and Φ_J the time and coordinate-dependent Hartree products of single-particle-functions (SPFs).

$$\Phi_J = \prod_{k=1}^{f} \varphi_{jk}(Q_k, t) \tag{2.8}$$

At the same time, the SPFs are formed by linear combinations of primitive basis, called discrete variable representation (DVR). The DVR corresponds to the lowest energy solutions of the harmonic oscillator of each coordinate.

$$\varphi_j^{(k)}(Q_k, t) = \sum_{k=1}^{n_k} a_{kj}^{(k)}(t)\chi_j^{(k)}(Q_k) \tag{2.9}$$

The multi-set formalism has been used to study the different electronic states. In this approach, a different wave function is employed for each electronic state.

$$\Psi(q_1, q_2, ..., \alpha, t) = \sum_{\alpha=1}^{\sigma} \Psi^{(\alpha)}(q_1, q_2, ..., \alpha, t)|\alpha\rangle \tag{2.10}$$

where α runs over the different electronic states.

The efficiency of MCTDH relies in a particular potential form of the Hamiltonian, $V(\boldsymbol{Q}) = V(Q_1)V(Q_2)\cdots V(Q_N)$. The total vibronic hamiltonian for intersystem crossing has the general form,

$$\boldsymbol{H}(\boldsymbol{Q}) = [\boldsymbol{T}(\boldsymbol{Q}) + \boldsymbol{V}(\boldsymbol{Q})]\,\mathbf{1} + \boldsymbol{H}^{\mathrm{NA}}(\boldsymbol{Q}) + \boldsymbol{H}^{\mathrm{SO}}(\boldsymbol{Q})\,. \tag{2.11}$$

The terms in the model Hamiltonian can be grouped in three different types: the diagonal elements $\boldsymbol{T}(\boldsymbol{Q})$ and $\boldsymbol{V}(\boldsymbol{Q})$, the non-adiabatic couplings $\boldsymbol{H}^{\mathrm{NA}}(\boldsymbol{Q})$ and the spin-orbit couplings $\boldsymbol{H}^{\mathrm{SO}}(\boldsymbol{Q})$. The coordinates Q are the normal modes mass and frequency weighted coordinates of the ground state. The off-diagonal elements contain the mean-field Breit-Pauli spin-orbit coupling between singlets and triplets and among triplets, computed at the CASSCF level of theory.[21] The non-adiabatic couplings are of the form $\alpha_{IJ} \times Q$, in which α_{IJ} is a parameter coupling states I and J electronic states of the same multiplicity, fitted by performing 1 performing 1D cuts along normal modes to reproduce the adiabatic electronic structure calculations.

The diagonal terms include the nuclear kinetic energy and the diabatic potentials. The expression for the nuclear kinetic energy expressed in mass-frequency-weighted coordinates for the electronic state I is a harmonic oscillator model (in a.u.), in which the kinetic energy operator is given by

$$\boldsymbol{T}(\boldsymbol{Q}_I) = -\frac{1}{2}\nabla\boldsymbol{Q}_I{}^T\boldsymbol{W}_I\nabla\boldsymbol{Q}_I \tag{2.12}$$

while the diabatic potential is assumed harmonic and the shape that takes is the following form,

$$\boldsymbol{V}(\boldsymbol{Q}_I) = E(0)\mathbf{1} + \frac{1}{2}\boldsymbol{Q}_I{}^T\boldsymbol{W}_I\boldsymbol{Q}_I\,. \tag{2.13}$$

In both equations, the matrix elements $[\mathrm{W}_I]_{ij}=\delta_{ij}\omega_i$ are the diagonal matrix of normal mode frequencies, and the normal mode coordinates $\mathbf{Q}_I=\mathbf{W}_\mathrm{I}^{1/2}\mathbf{L}_\mathrm{I}\mathbf{M}^{1/2}\Delta\mathbf{R}$, in which $\boldsymbol{L}$ are the eigenvectors of the internal Hessian matrix, $\mathbf{M}^{1/2} = \delta_{ij}m_i^{1/2}$ is the atomic mass metric and $\Delta\mathbf{R}$=$\mathbf{R}$-$\mathbf{R}_{\mathrm{ref}}$ is the Cartesian coordinate difference with the reference.

In the case of iron complexes, the potentials are fitted performing a Taylor expansion up to fifth order and extra functions like exponential and Morse potentials to improve the fit of dissociative or highly anharmonic potentials. In the case of xanthone, we developed a new model Hamiltonian including Duschinsky rotations, as I will detail in the following. This is a convenient way to express the excited state normal mode coordinates in terms of a common reference coordinate system. As reference, we take the $1^1\mathrm{A}_1$ normal modes coordinates as reference, symbolized hereafter as Q (i.e., without any subscript). For this purpose, we introduce the projection of excited-to-reference normal coordinates

through the Duschinsky rotation matrices, expressed as

$$\boldsymbol{Q}_I = \boldsymbol{W}_I{}^{1/2}\left(\boldsymbol{W}^{-1/2} J_I \boldsymbol{Q} + \boldsymbol{D}_I\right) \tag{2.14}$$

is introduced with this aim and allows to re-write the expression of all the states in the basis of the ground state. In the above expression, $\mathbf{J}_\mathrm{I}$=$\mathbf{L}_\mathrm{I}\mathbf{L}^\mathrm{T}$ is a square matrix that contains the normal mode mixing between the state I and the reference state and $\mathbf{D}_\mathrm{I}$ is the displacement vector between the state I minimum geometry and the reference state geometry expressed in the normal modes of the latter.

The nuclear kinetic energy operator can be expressed in the ground state normal modes.

$$\boldsymbol{T}(\boldsymbol{Q}) = -\frac{1}{2}\left(\frac{\partial}{\partial \boldsymbol{Q}}\right)^T \boldsymbol{J}_I \boldsymbol{W} \boldsymbol{J}_I{}^T \left(\frac{\partial}{\partial \boldsymbol{Q}}\right) \tag{2.15}$$

The diabatic potentials in the common coordinate system take the following expression:

$$\boldsymbol{V}(\boldsymbol{Q}) = E(0)\mathbf{1} + \frac{1}{2}\boldsymbol{Q}^T(\boldsymbol{J}_I^T \boldsymbol{W}_I^2 \boldsymbol{W}^{-1} \boldsymbol{J}_I)\boldsymbol{Q} + \boldsymbol{D}_I{}^T \boldsymbol{W}_I{}^2 \boldsymbol{W}^{-1/2} \boldsymbol{J}_I \boldsymbol{Q} + \frac{1}{2}\boldsymbol{D}_I^T \boldsymbol{W}_I^2 \boldsymbol{D}_I \tag{2.16}$$

2.1.3 Xanthone

Note: Reprinted (adapted) with permission from Journal of the American Chemical Society 2021 143 (51), 21474-21477. Copyright 2021 American Chemical Society.

Xanthone is an aromatic ketone exhibiting one of the fastest intersystem crossings among organic molecules. The results discussed in this section are based on the article entitled *Ultrafast Intersystem Crossing in Xanthone from Wavepacket Dynamics* , J. Am. Chem. Soc. 2021, 143, 51, 21474–21477. This work was performed in collaboration with a visiting PhD student (Marc Alías-Rodríguez, that later became post-doctoral fellow in my group) from the Universitat Rovira i Virgili in Tarragona.[15]

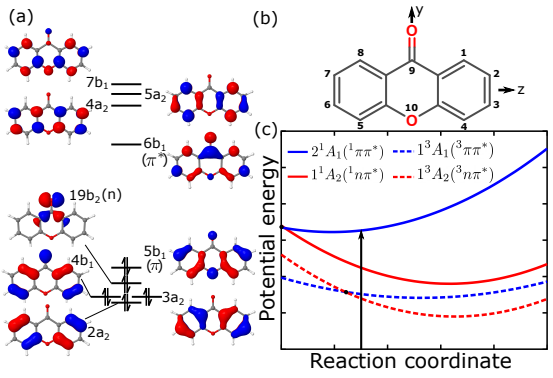

Figure 2.1: (a) the 5 highest occupied and 4 lowest unoccupied orbitals with C_{2v} labels and common name in parenthesis. (b) structure of 9H-xanthen-9-one (xanthone) with number and Cartesian axis orientation. (c) schematic diabatic potential energy curve of the two lowest singlet (solid line) and triplet (dashed line) excited states of $n\pi^*$ (red) and $\pi\pi^*$ (blue) character. The vertical arrow indicates the absorption from the $^1\pi\pi$ ground state (not shown in the figure).

Xanthone lowest energy state is a singlet 1^1A_1 state (using C_{2v} point group symmetry labeling, with the orientation as described in Fig. 2.8). At this geometry, the 1^1A_2 state is the first excited singlet, corresponding to a $19b_2 \rightarrow 6b_1$ transition (also called $^1n\pi^*$ state), which is dipole-forbidden. The

second singlet excited state is the 2^1A_1 state, which is represented by a $5b_1 \rightarrow 6b_1$ transition (more commonly referred to $^1\pi\pi^*$ state), and is dipole-allowed. In the minimum energy structure of 1^1A_1 state (Fig. 2.8), the triplets 1^3A_2 and 1^3A_1 are quasi-degenerate (0.03 eV gap), 0.166 eV below the singlet 1^1A_2 state, in good agreement with the experimental value of 0.14 eV.[22] The 1^1A_2 state is only 0.06 eV below the 2^3A_1 described mainly by a $4b_1 \rightarrow 6b_1$ transition, and the triplet 1^3B_2 described mainly by a $3a_2 \rightarrow 6b_1$ is found ~0.11 eV above 1^1A_2. The 2^1A_1 state ($5b_1 \rightarrow 6b_1$) is the highest energy state, 0.4 eV above the 1^1A_2 state. Minimal energy structures of the lowest singlet and triplet states are planar of quasi-C_{2v} symmetry. As for the state crossings, on the one hand the $2^1A_1/1^1A_2$ ($^1\pi\pi^*/^1n\pi^*$) cross in an accidental different symmetry structure of C_s resulting from the linear combination of the carbonyl symmetric stretching (essentially of a_1 symmetry) and an asymmetric stretching vibration of mostly b_1 symmetry involving the carbon atoms on the aromatic ring. On the other hand, 1^1A_2 crosses with 1^3A_1 state in a quasi-C_{2v} structure expanded through totally symmetric vibrations involving the carbonyl symmetric stretching of the aromatic rings.

The dynamic evolution of diabatic populations is shown in Fig. 2.7. The simulations started at the 2^1A_1 state. The population rapidly decays in the first 200 fs, concomitant to the 1^1A_2 population rise, indication of a fast internal conversion. This is due to the barrierless access to two $1^1A_2/2^1A_1$ accidental different symmetry intersection. In this process, 80% of the 2^1A_1 is transferred to 1^1A_2, and 20% of the population remains trapped in 2^1A_1 decaying at a slower rate. The 1^1A_2 being the major state after 200 fs rapidly decays to the triplets. Initially, the ISC is mainly due to $1^1A_2 \rightarrow 1^3A_1$ but also $1^1A_2 \rightarrow 2^3A_1$. These are the main channels for generating triplet population, consistent thus with El-Sayed's rule for ISC. The transfer between triplets slowly builds up the population on the lowest triplet 1^3A_2.

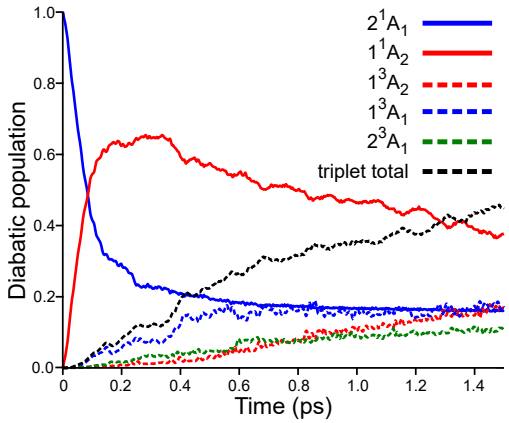

Figure 2.2: Diabatic population evolution for the singlets 2^1A_1 ($^1\pi\pi^*$, solid blue) and 1^1A_2 ($^1n\pi^*$, solid red), and triplets 1^3A_2 ($^3n\pi^*$, dashed red), 1^3A_1 ($^3\pi\pi^*$, dashed blue) and 2^3A_1 (dashed green). Black dashed line corresponds to the sum of all triplet populations. The dynamics have started from 2^1A_1.

A first-order kinetic mechanism can be extracted from the 1.5 ps population dynamics of Fig. 2.7. From the model, we can infer that the mechanism follows mainly a sequential transfer: $2^1A_1 \xrightarrow{IC} 1^1A_2 \xrightarrow{ISC} 1^3A_1 \xrightarrow{IC} 1^3A_2$. First, the 2^1A_1 state decays biexponentially to the 1^1A_2 state via internal conversion. About 80% of the population decays in a fast rate of 85 fs. This fast component is explained as the first time the wavepacket reaches the $2^1A_1/1^1A_2$ crossing with a large momentum, since the path to it is barrierless. Only activation of coupling modes of a_2 symmetry can make this transition happen, which could explain the incomplete transfer. After that, 15% of the wavepacket remains trapped in the 2^1A_1 minimum, and slowly decays to 1^1A_2 with a rate of 5 ps via the activation of coupling modes. In the 1^1A_2 state, there are three possible ISC transfers. The $1^1A_2 \rightarrow 2^3A_1$ and $1^1A_2 \rightarrow 1^3B_2$ triplet rates are obtained at 6.73 and 44.64 respectively ps. In this time, we do not observe a fast internal conversion to

the 1^3A_1 and 1^3A_2, but probably this occurs at longer times. The fastest important ISC is the $1^1A_2 \rightarrow 1^3A_1$, which is the first populated triplet in time. The rate for this transfer is given by 2.0 ps, which is probably explained by a strong spin-orbit coupling and the fact that the ISC minimum energy crossing geometry is close to the minimum of 1^1A_2 state. The internal conversion between $1^3A_1 \leftrightarrow 1^3A_2$ is the only pathway we obtained of population of the lowest triplet state, and is estimated at 602 fs for the transfer to 1^3A_2 and 803 fs for the back transfer to 1^3A_1.

In the literature, a major channel corresponding to a "non-Kasha" transfer directly from 2^1A_1 to the 1^3A_2 triplet was evoked, first by Baba and coworkers for xanthone in the gas phase,[22, 23] and later confirmed by Gilch and coworkers for xanthone in ethanol[24, 25]. Baba et al. estimated the rate of transfer from 2^1A_1 in the gas phase at ca. 100 fs,[23] while the experiments of Gilch et al. in ethanol estimated it at 1.5 ps.[24] Recently, theoretical studies using rate theory in the gas phase by Rai-Constapel and coworkers predicted a 5 ps for the $2^1A_1 \rightarrow 1^3A_1$ (El-Sayed's forbidden), while the $2^1A_1 \rightarrow 1^3A_2$ (El-Sayed's allowed) was found having a 200 ps rate.[7] In the gas phase, the main decay channel observed from 2^1A_1 is to the 1^1A_2. This is estimated at a rate of 135 fs, close to the experimental decay of 100 fs observed for 2^1A_1 in the gas phase.[23] The 2^1A_1 state has an almost negligible vibronic spin-orbit coupling with energetically close 2^3A_1 and 1^3B_2 states. The 2^3A_1 triplet receives 5-10% population, while the population to the 1^3B_2 states is negligible. This could explain the triplet coupling evoked for the 2^3A_1 state.[22] No direct transfer from 2^1A_1 is observed to 1^3A_2 nor 1^3A_1 states. Rather, the ISC channel is $1^1A_2 \rightarrow 1^3A_1$ in a rate of 2.0 ps, 10 times slower than the rate obtained by Rai-Constapel and coworkers.[7] The combined $1^1A_2 \rightarrow$triplets leads to a rate transfer of 1.5 ps. A similar rate is obtained if the dynamics are started directly from the 1^1A_2 state. Finally, the transfer between $1^3A_1 \rightarrow 1^3A_2$ is fast, estimated at 602/803 fs for the forth and back transfers (in ethanol, this was estimated at 12 ps).[24] Solvents have a strong impact on the energetic order of $n\pi^*$ and $\pi\pi^*$ states of aromatic ketones, and this has a major impact on the dynamics in the excited state. Using the vacuum model, we have shifted the vertical energies to the values obtained for xanthone in solution.

In polar solvents, the order of electronic states changes with respect to the gas phase.[24, 25] For triplets states, the $^3\pi\pi^*$ is the lowest state both in water and ethanol. For singlet states, ethanol exhibits the same ordering as in gas phase. In contrast, in water the $^1n\pi^*$ fluctuates influenced by hydrogen bonds between water and carbonyl. From 1 ps QM/MD water simulations, most snapshots exhibit an $^1n\pi^*$ state below the $^1\pi\pi^*$ state. In such state ordering, quantum dynamics show that internal conversion $^1\pi\pi^* \rightarrow ^1n\pi^*$ is within 325 fs prior to the ISC in 2.11 ps. The populated triplets are mostly the upper $2^3\pi\pi^*$ and $3^3\pi\pi^*$ at variance with the gas phase. In contrast, when $^1\pi\pi^*$ is lowest, the wavepacket stays trapped in the singlets with a negligible ISC.

Currently, I established two experimental collaborations to determine this mechanism. First, Lionel Poisson and Lou Barreau (U. Paris-Saclay) have performed time-resolved UV photoelectron spectra which seems to confirm our mechanism (manuscript in preparation). This experiments were able to clearly determine the kinetic rate of $^1\pi\pi^*$ state, and potentially a second kinetic rate that is associated to the decay of $^1n\pi^*$. These experiments are waiting for a more clear validation from time-resolved X-ray photoelectron spectra, a collaboration that I established with Markus Guhr (DESY, Germany).

2.1.4 Iron complexes

Note: Reprinted (adapted) with permission from J. Phys. Chem. Lett. 2023, 14, 38, 8571–8576. Copyright 2023 American Chemical Society.

In this work, we studied intersystem crossing on organometallic complexes using quantum dynamics. This work was done in collaboration with two post-doctoral fellows, Swarnendu Bhattacharyya, who developed the model Hamiltonian and Marc Alías-Rodríguez who finalized the analysis and performed the quantum dynamics. This project is part of the ANR PRCi project MULTICROSS (2019-2024) devoted to the combination of theoretical modeling to understand time-resolved X-ray spectroscopy produced in X-ray free electron lasers. In this particular project, we explained the time-resolved X-ray emission of $[Fe(bpy)_3]^{2+}$ (bpy=2,2'-bipyridine). The results were published in J. Phys. Chem. Lett. 2023, 14, 38, 8571–8576.[17]

Molecules containing d^4 to d^7 octahedral metal complexes exhibit magnetic bistability known as spin crossover (SCO), in which the metal center undergoes a transition from a low-spin (LS) to a high-spin (HS) electronic configuration, induced by several kinds of external stimuli such as temperature, pressure, light radiation or the application of a magnetic field.[26–33] Light-induced SCO reactions (commonly known as light-induced excited spin-state trapping, LIESST) have attracted particular interest. Such photoactive complexes can act as molecular switches due to the ultrafast conversion between two magnetic states.[34] Conversely, efficient light-harvesting and photocatalyst complexes can be produced by delaying the SCO reaction which stabilizes charge-transfer states.[35] The photochemical pathways are highly dependent on the type of metal, the ligands, the electronic band structure, and the initial absorbing state.[34] Elucidating the LIESST mechanisms is fundamental for designing complexes with controlled photoreactivity.

The current understanding of LIESST mechanisms is in most cases incomplete, especially due to the complex interplay between electronic and vibrational degrees of freedom and the ultrafast nature of the photoreaction, which challenges the interpretation of time-resolved spectra.[28–33, 36–42] Theoretical models, on the other hand, can only provide a complete model for the photoreaction when a balanced treatment of non-adiabatic and spin-orbit couplings of electronic excited states with different spin multiplicities is used, requiring state-of-the-art methodologies for electronic structure and quantum dynamics.[4] Multi-configuration time-dependent Hartree (MCTDH) wavepacket dynamics, pioneered by Pápai and Penfold, have been shown to successfully describe the photophysics of iron complexes.[43–46]

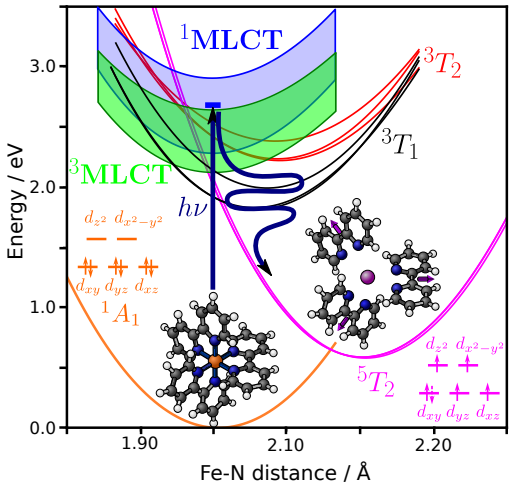

Figure 2.3: Representation of the potential energy surfaces and geometric changes during LIESST reaction in $[Fe(bpy)_3]^{2+}$, including the high-spin ($^5T_2$), the metal-centered triplets ($^3T_1$ and $^3T_2$) and the singlet/triplet metal-ligand charge transfer states ($^{1/3}$MLCT).

The LIESST reactions in organometallic iron compounds have been the focus of much research, due to the cost-effectiveness and scalability of iron complexes.[47] In the present study, we focus on the LIESST mechanism of a well-known iron complex, $[Fe(bpy)_3]^{2+}$ (bpy=2,2'-bipyridine) (see Fig. 2.8). The low-spin (LS) state of $[Fe(bpy)_3]^{2+}$ corresponds to a singlet closed-shell configuration ($^1A_1$), in which six nitrogens form a dative covalent bond with the iron center. The high-spin (HS) states are constituted by a quintet triad ($^5T_2$) with a gap of ca. 0.1 eV due to a small Jahn-Teller distortion.[48] According to our simulations, the HS is characterized by a symmetric increase of the Fe-N distances (+0.2 Å) and a slight decrease (-5.7°) of the N-Fe-N bite angle with respect to the LS equilibrium geometry. This is a consequence of populating e_g antibonding orbitals. The absorption spectrum exhibits two maximum absorbances at 520 and 350 nm corresponding to metal-to-ligand-charge-transfer (MLCT) states.[38,

39, 49, 50]

The photochemical LIESST mechanism in $[Fe(bpy)_3]^{2+}$ has been thoroughly studied both experimentally and theoretically.[16, 28–33, 38, 39, 41, 42, 51]. The $[Fe(bpy)_3]^{2+}$ photoreaction model depicted by time-resolved spectroscopy has been refined in parallel to the development of new techniques with improved time resolution.[36, 52] One of the first studies employing UV-visible transient absorption spectroscopy suggested a sub-ps ^{1}MLCT→^{5}T$_2$.[53] Time-resolved fluorescence spectroscopy of Gawelda et al. pointed out the population transfer between MLCT states (^{1}MLCT→^{3}MLCT) in 15 fs,[28] and mechanism via the MC triplets (^{3}MLCT→ ^{3}MC) in 120 fs prior to the HS transfer in 960 fs. This mechanism was confirmed and refined by Gaffney and coworkers using time-resolved X-ray K_β fluorescence spectroscopy, with 150 fs MLCT/MC triplet transfer and a faster transfer to quintets in 70 fs.[31] Combining time-resolved X-ray emission and scattering, Gaffney et al. later indicated that HS→^{3}MC back-transfer occurs prior to the final relaxation to the HS.[36] Auböck and Chergui, based on high-resolution UV-visible pump-probe spectroscopy determined a build-up of HS population in less than 50 fs, assisted by high-frequency ligand modes.[32] Lemke et al. confirmed this mechanism using time-resolved X-ray absorption spectroscopy estimating a slower transfer rate of 120 fs to the HS.[33] Finally, Moguilevski et al. using ultrafast extreme UV photoemission spectroscopy determined that both ^{3}MC→HS and ^{3}MLCT→HS were competing mechanisms.[54] From a theoretical perspective, there is no unified model of the mechanism of $[Fe(bpy)_3]^{2+}$ photoreaction. Sousa et al. computed the kinetic rates of intersystem crossing (ISC) using Fermi's golden rule, determining a dominant ^{3}MC→HS mechanism due to larger MC/HS spin-orbit coupling,[51] but later considered the direct ^{3}MLCT→HS mechanism possible from the mixing between MC and MLCT states due to thermal disorder.[41] Iuchi et al. have recently presented a trajectory surface hopping study in $[Fe(bpy)_3]^{2+}$ in aqueous solution using a constructed model Hamiltonian, proposing a dominant SCO transfer via ^{3}MC states.[55]

We construct a complete quantum dynamics model for describing the LIESST reaction in $[Fe(bpy)_3]^{2+}$ describing the SCO photodynamics upon absorption to the bright states within the MLCT band. The details of the construction of the model can be found in the Supporting Information (see further in Sec. S2). The model contains the lowest part of the excited state spectrum, which can be characterized either by d-d type transitions (MC states) or a d- to π_1^* bipyridine orbitals (MLCT states), composed of a C_2-$C_{2'}$ bonding π region and a N-C_2/N-$C_{2'}$ anti-bonding π^* region common of diimine bonds (see Fig. S1 and S2). In the D_3 geometry, the π^* orbitals have an $a_2 \oplus e$ symmetry delocalized over the three equivalent bipyridine units. The singlet bright states are found in the middle of the MLCT band and have $t_{2g} \rightarrow \pi_1^*$ character, using the O_h notation. The excitation at the ^{1}A$_1$ minimum geometry is 2.65 eV, with an oscillator strength of $8.5{\cdot}10^{-2}$ a.u. The rest of the singlet MLCT band is dark. The ^{1}T$_1$ states lie at the upper end of the MLCT band (around 3 eV) and are not accessible from the lower range of the absorption spectrum. The triplet manifold consists of an MLCT band (2.09-2.51 eV) overlapping with the ^{1}MLCT band, the ^{3}MC, and the ^{5}T$_2$ states. The ^{3}T$_1$ is found in a range of 1.91-2.13 eVs, while the ^{3}T$_2$ lies between 2.41-2.62 eV. These excited state energies are computed along 9 vibrational modes: (i) the reaction coordinate (depicted in Fig. 2.8) consisting mainly of a symmetric stretching of all Fe-N distances, (ii) two Jahn-Teller asymmetric Fe-N stretching modes that distort the complex in axial/equatorial planes, and (iii) six ligand centered modes corresponding to a C_2-$C_{2'}$ coupled with C-C and C-N inter-ring stretching modes of the bipyridine units accounting for the relaxation in the MLCT bands.

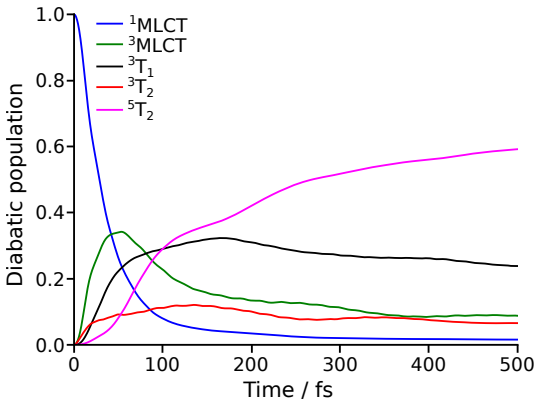

Figure 2.4: Diabatic population dynamics of ^{1,3}MLCT, ^{3}MC (^{3}T$_1$ and ^{3}T$_2$) and HS states during the first 0.5 ps using the full hamiltonian model of $[Fe(bpy)_3]^{2+}$. The singlet ^{1}T$_1$ is included in the model, but not depicted in the figure due to negligible population.

The vibronic model has been used in quantum dynamics starting from a wavepacket in the lowest bright ^{1}MLCT states. The results for the first 0.5 ps are shown in Fig. 2.9. The population on the ^{1}MLCT undergoes a rapid decay becoming negligible after 150 fs. The first decay of the ^{1}MLCT is concomitant to the rapid growth of the ^{3}MLCT population, which becomes dominant at around 50 fs. The wavepacket is then split into three different populations. The dynamic evolution of populations of the two ^{3}MC states behaves similarly. On the one hand, the ^{3}T$_1$, which receives 30% of the population, exhibits a rapid growth from the beginning of the dynamics followed by a slow decay after 150 fs. On the other hand, the ^{3}T$_2$, which receives 10% of the population has a slow decay after 100 fs. The quintet ^{5}T$_2$ has a rapid and steady growth starting at around 50 fs until the end of the dynamics, becoming the dominant population after around 120 fs.

The triplet intermediates (^{3}MLCT, ^{3}T$_1$ and ^{3}T$_2$) have been experimentally observed during the SCO photodynamics,[32, 33, 35, 54], but there is a debate on which triplet catalyzes the intersystem crossing to the HS state. Indeed, two types of intersystem crossing mechanisms can be distinguished, either via a direct intersystem crossing ("direct mechanism", ^{3}MLCT → HS) or a triplet internal conversion prior to the intersystem crossing ("indirect mechanism", ^{3}MLCT → ^{3}MC→ HS). In order to unravel the mechanism, we performed wavepacket dynamics on "reduced" model Hamiltonians, in which we deactivate certain interstate couplings or vibrational modes, allowing us to dissect the dominant pathways in the excited state.

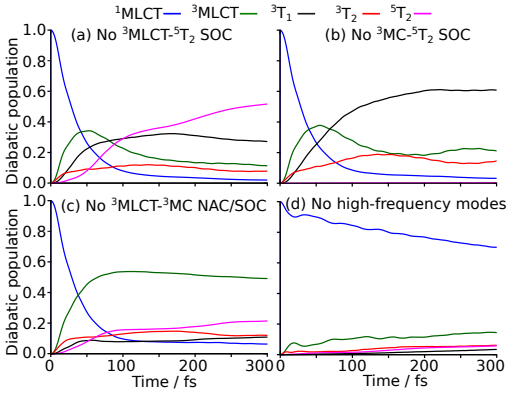

Figure 2.5: Diabatic population dynamics using different reduced models, namely (a) deactivating the spin-orbit coupling between ^{3}MLCT and $^5T_2$, (b) deactivating the spin-orbit coupling between ^{3}MC and $^5T_2$, (c) deactivating the couplings between ^{3}MC and ^{3}MLCT, and (d) not including the high-frequency bipyridine modes.

The evolution of diabatic populations from the wavepacket dynamics on reduced models are shown in Fig. 2.5. At first glance, the dynamics deactivating the ^{3}MLCT-$^5T_2$ spin-orbit coupling are equal to the full model. In contrast, the HS state is not populated when deactivating the ^{3}MC-$^5T_2$ spin-orbit coupling. This excludes the possibility of a "direct mechanism", in agreement with the weak spin-orbit coupling between ^{3}MLCT and $^5T_2$, and confirms the "indirect mechanism" as the dominant path to reach the population of the HS state.

The deactivation of the ^{3}MLCT/^{3}MC non-adiabatic and spin-orbit couplings lowers the population of the quintet state, proportional to the decrease of the population from the ^{3}MC states. This suggests, on the one hand, that part of the ^{3}MC population is transferred directly from the ^{1}MLCT via intersystem-crossing. In addition, it shows that ^{3}MC states are also populated from ^{3}MLCT in an internal conversion process. Finally, we deactivated $^3T_1$/HS or $^3T_2$/HS spin-orbit couplings (see Sec. S3.D of the supporting information). The deactivation of the $^3T_2$/HS does not exhibit significant differences in the HS population, whereas the deactivation of $^3T_1$/HS drastically reduces the HS population. Therefore, the $^3T_1$ is the main intermediate populating the $^5T_2$ state.

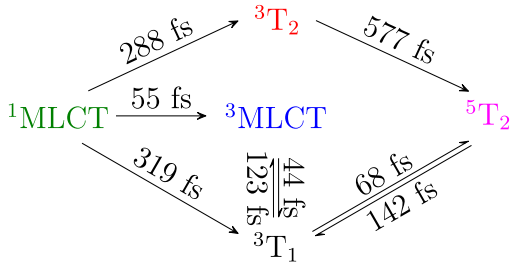

Figure 2.6: Schematic representation of the kinetic rates extracted from a first-order kinetic model.

From these quantum dynamics results, one can infer a global first-order kinetic model for the light-induced spin crossover (LISCO) reaction of $[Fe(bpy)_3]^{2+}$, summarized in Fig. 2.6. To obtain the rates for each process, the kinetic rates have been optimized to fit the evolution of diabatic populations obtained by the wavepacket dynamics with the full model (for further details, see Sec. S3.B in the supporting information). For a successful first-order fitting, the back-transfer reactions between ^{3}MLCT/$^3T_1$ and

$^3T_1/^5T_2$ are required. Alternatively, such populations can be fitted by adding a delay time in the ^{3}MC states.[36] On the one hand, the total singlet/triplet transfer takes 40 fs, slightly slower than the <30 fs transfer observed experimentally.[30] This transfer can be decomposed in a fast transfer to the triplet MLCT, which takes 55 fs, and two slower transfers directly to the $^3T_1$ and $^3T_2$ MC states in 319 fs and 288 fs, respectively. The total triplet/quintet transfer takes place in 178 fs, in good agreement with the 120-130 fs reported in the literature. [28–31, 33] An equilibrium is established in the triplet MLCT/MC, ^{3}MLCT $\leftrightarrow$ $^3T_1$ with a forward and backward kinetic rate of 44 and 123 fs respectively, thus favoring the population of $^3T_1$. The HS state is populated via a fast decay from the $^3T_1$ state (68 fs) and a slower decay from the $^3T_2$ state (577 fs), further supporting the triplet T_1 as the main state responsible of the transfer to the HS. A back transfer reaction from the HS to the $^3T_1$ states is possible, with a transfer rate of 142 fs, confirming the picture by Gaffney et al. using K_β emission.[36]

The role of the different vibrational modes in the ultrafast mechanism has been also a matter of discussion.[32, 33] Previous studies agree that the symmetric Fe-N stretching is the dominant mode activated during the LIESST photo process. We confirm this observation from wavepacket dynamics, in which the Fe-N distance is increased by ca. 0.10 Å during the dynamics due to the population of antibonding Fe-N orbitals in MC states. Axial and equatorial Fe-N distances evolve similarly, indicating weak Jahn-Teller distortions. The N-Fe-N bite angle slightly increases ($\approx 0.5°$) during the first 20 fs of the simulation decreasing steadily to reach a value around -3.0° compared to the LS. The C_2-$C_{2'}$ bond length initially decreases because of the population of the MLCT states which stabilize at shorter distances because of the π bonding character within the so-called π_1^* orbital. Afterward, it increases as a consequence of the transfer to MC states and the enlargement of Fe-N distances. As stated by Auböck et al.[32], the high-frequency modes in bipyridine play a key role in the process. These modes allow an efficient ISC and relaxation in the MLCT band. The exclusion of these modes in reduced model dynamics exhibits a trapped population in the MLCT manifold (see Fig. 2.5).

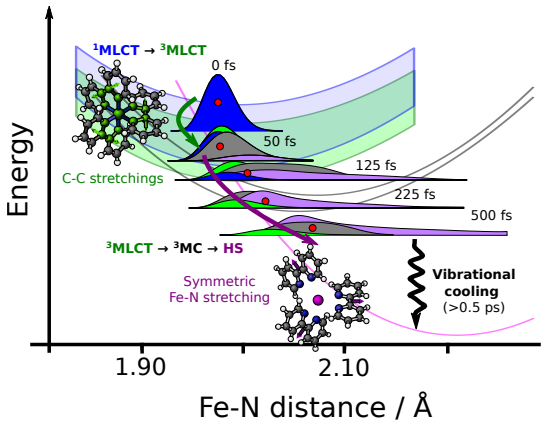

Figure 2.7: Schematic summary of the photoreaction of $[Fe^{II}(bpy)_3]^{2+}$ at key times as determined by quantum dynamics. The wavepacket density along the reaction coordinate is decomposed in the densities of ^{1}MLCT (blue), ^{3}MLCT (green), ^{3}MC (grey), and HS (magenta). The average position is shown as a red circle. The first step is the conversion between MLCTs, dominated by C-C stretchings whereas the MLCT to MC conversion is controlled by the symmetric Fe-N stretchings.

In Fig. 2.7 we summarize the picture provided by wavepacket dynamics on the LIESST reaction of $[Fe(bpy)_3]^{II}$, by showing the wavepacket density along the reaction coordinate for the first 500 fs of the photoreaction. The intersystem crossing (^{1}MLCT→^{3}MLCT) occurs very rapidly and brings the wavepacket to the bottom of the MLCT band. At this time, a ^{3}MC population is already appreciable. No

activation of the reaction coordinate is observed at this time; bipyridine stretchings exclusively dominate the MLCT relaxation. The numerous vibronic and spin-orbit couplings between the MC/MLCT triplets together with their small energy gap at the ^{3}MLCT band minimum make the transfer between the two very efficient. However, the compact Gaussian-like wavepacket at the minimum of the MLCT band generates a hot vibrational wavepacket in the direction of the reaction coordinate, as observed by the spreading of the density over a large region of Fe-N distances. This large spread implies that part of the wavepacket is always sitting in a region of efficient transfer between the ^{3}MC and the HS. After this transfer is complete, the wavepacket rephases at longer times (>0.5 ps) by cooling down by releasing vibrational energy to the environment.

2.1.5 Photolysis of carbon monoxide in myoglobin

In this project, I studied of the photophysics of carbon monoxide from a model of the heme active site in myoglobin. At that time, this was the largest quantum dynamics simulation ever done, owing to the number of electronic states and degrees of freedom. This project was part of a Humboldt fellowship in collaboration with Prof. Irene Burghardt at Goethe University Frankfurt. In this particular project, we explained the ultrafast mechanism of photolysis that was elusive for time-resolved X-ray spectroscopies in the X-ray free electron lasers.[45]

Hemeproteins containing a porphyrin-iron complex (heme) play a major role in the storage and transport of diatomic molecules.[56] The diatomic ligand dissociation occurs concurrently to a spin-crossover (SCO) transition from low-spin (LS) to high-spin (HS) of the Fe^{II} centre.[57] The heme complex with carbon monoxide (CO) in myoglobin is one of the most studied hemeproteins of this kind.[58–73] Heme–CO is initially in a singlet LS state (S=0), which transforms to a quintet HS state (S=2) upon CO dissociation.[65] The unbound CO in the myoglobin cavity along with the motions of the remaining heme initiate a “protein quake” that opens a channel for the diatomic molecule to escape.[58] Over a century ago, Halden and Lorrain discovered that the CO dissociation can be initiated photochemically,[74] by a mechanism which is still under debate. The photolysis can be initiated upon absorption to the lowest singlet porphyrin band (^{1}Q) or the second porphyrin band (^{1}B).[75] Here, we focus on the photochemistry of the heme–CO complex upon excitation to the lowest Q-band of porphyrin.

The heme-CO photolysis is an ultrafast process. Recent pump-probe X-ray experiments of myoglobin, with an initial pump pulse exciting the ^{1}Q state, seem to agree on a two-step kinetic reaction: (i) a first step taking <50-70 fs, attributed to both CO photolysis and partial SCO, and (ii) a completion of the spin transition to the HS state in ~300-400 fs.[60, 61, 75] Despite the numerous studies on heme-CO photolysis, the kinetics and mechanism of dissociation are still under debate, notably regarding the ultrafast nature of the reaction, and the spin and character of the photolytic state. The rate of photolysis has never been experimentally reported, apart from the upper bound of 50-70 fs. As far as the photolytic state is concerned, the most widely accepted hypothesis is that dissociation occurs from a metal-ligand charge-transfer (MLCT) state.[70–73, 75] Still, experiments and theory do not provide a unified picture to date. On the one hand, Franzen, Martin *et al.*, based on time-resolved absorption and Raman experiments, described a “rapid spin state change that must precede photolysis”.[75] They consider that photolysis is occurring from a triplet metal→porphyrin ring transfer (^{3}MLCT dissociation).[75, 76] In the model by Franzen et al., the ultrafast reaction is due to valence tautomerism. This mechanism implies a rapid interconversion of several quasi-degenerate electronic states involving d-transitions, some of which are dissociative for the CO bond. On the other hand, Head-Gordon *et al.*, employing time-dependent density-functional theory simulations, proposed a dissociation in a singlet metal→σ^*_{CO} state (^{1}MLCT dissociation).[70–73] In the model of Head-Gordon et al., CO photolysis occurs in a Marcus-like process, in which the initial ^{1}Q population is transferred to the photolytic state after crossing a barrier of <0.2 eV. However, this hypothesis seems in contradiction with experimental observations of absence of fluorescense emission, an ultrafast reaction and a unity quantum yield for the heme-CO complex.[77] The theoretical method used provided an incomplete description of ultrafast heme-CO photolysis, since the coupled electron-nuclear motion was neglected. Recent theoretical studies of similar iron complexes indicate the fundamental role of nuclear motions in explaining the ultrafast nature of

intersystem crossing (ISC).[40, 78, 79] Such electron-nuclear strong coupling has been experimentally observed in time-resolved X-ray absorption in a Fe(II) tris(2,2'-bipyridine) complex[32, 33] and also in ferricyanide ion.[80]

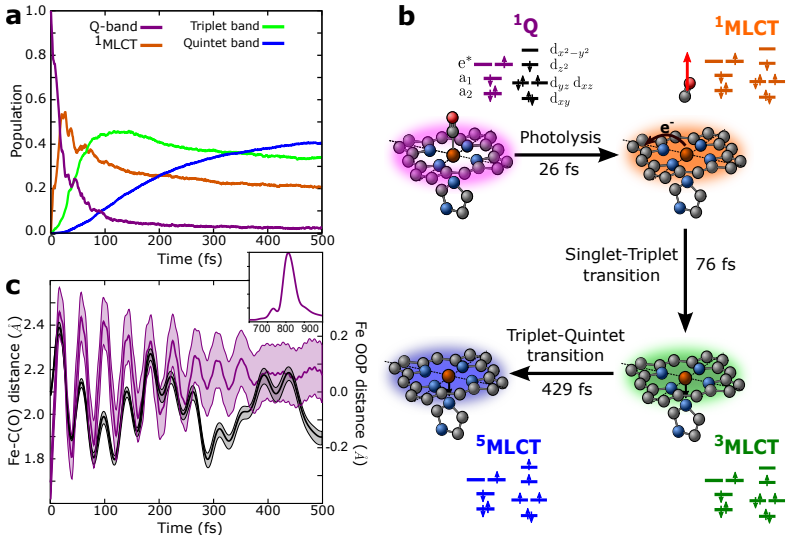

Figure 2.8: **Photodynamics of photolysis and spin-crossover.** Quantum photodynamics of heme–CO complex during the first 0.5 ps, with initial conditions averaged over 10 molecular dynamics snapshots. **(a)** Evolution of diabatic populations for states ^{1}Q (magenta), ^{1}MLCT (orange), triplet band (green) and quintet band (blue). The ^{1}Q population rapidly decays giving rise to ^{1}MLCT population dominating by 75 fs, at which point the triplet population increases. The quintet population builds up more slowly, and evolves into the dominant state at around 350 fs. **(b)** Schematic representation of the reaction mechanism and interpretation in terms of time constants. Upon initial excitation to the Q-band, the metal-to-ligand charge transfer (MLCT) state is populated in ~25 fs. In a second step, the system relaxes to the triplet (~75 fs) and to the lowest quintet state (~430 fs). Black arrows indicate the direction of the electron transfer and the main nuclear motions. **(c)** Evolution of the Fe-C(O) distance (magenta, left axis) and the Fe out-of-plane distance (black, right axis). Large amplitude motions are observed with a period of oscillation of 40 fs. The amplitude of oscillation is initially 0.9 Å and converges towards a value of 2.2 Å. At this distance, the CO is essentially photolyzed. The standard deviation of these geometric values is shown as a shaded area. In the inset, the Fourier transform of the Fe-C(O) oscillations is shown (in cm^{-1}).

The model taken as representative of the active center of the myoglobin protein consists of an Iron(II) encapsulated in a porphyin ring, and axially ligated to a CO and an imidazole. Hereafter this model is referred to as heme–CO for the complex with carbon monoxide and simply heme for the remaining ligands. The LS state of the heme–CO complex has an electronic configuration $(a_2)^2(a_1)^2(e_x^*,e_y^*)^0$ for the porphyrin and $(d_{xy})^2(d_{xz},d_{yz})^4(d_{z^2})^0(d_{x^2-y^2})^0$ for Fe. In its minimum energy structure, the iron and

porphyrin are coplanar and the CO is bound to Fe in an upright position perpendicular to the plane. The Fe-C(O) bond is 1.80 Å, around 0.26 Å shorter than the Fe-N bonds with porphyrin or imidazole, which are 2.03 Å and 2.06 Å respectively. Upon photolysis, the Fe changes into a quintet state, with electronic configuration $(d_{xy})^1(d_{xz},d_{yz})^3(d_{z^2})^1(d_{x^2-y^2})^1$. In the HS, the Fe-CO bond is unstable. The iron is displaced from the porphyrin plane, distorted to a square-pyramidal structure. The Fe-N bond length is 2.10 Å for the porphyrin nitrogens and 2.17 Å for imidazole.

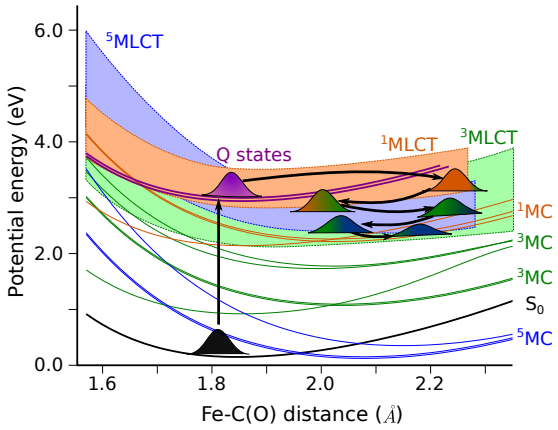

Figure 2.9: **Potential energy surface along a dissociative mode.** Plot of the potential energy surfaces along the Fe–C(O) distance. The LS state S_0, and the ^{1}Q states are shown in black and magenta respectively. The singlet manifold is shown in orange, the triplet manifold in green and the quintet manifold in blue. The metal-centered (MC) states are shown explicitly, whereas the metal-ligand charge transfer (MLCT) states are depicted as a quasi-continuous band. Further, a schematic evolution of the wavepacket dynamics is shown. After absorption to the Q-band, the wavepacket undergoes large-amplitude oscillations in the Fe-CO coordinate on the ^{1}MLCT state. Then, it cascades down acquiring more ^{3}MLCT and ^{5}MLCT character as the spin crossover transitions occur. Finally, the wavepacket disperses, and the Fe–C(O) distance oscillations decrease to a value of 2.2 Å.

The lowest valence states (up to ca. 2 eV) correspond to dark doubly-degenerate metal-centered (MC) states, involving transitions from the occupied d_{xy}, d_{xz} and d_{yz} orbitals to the unoccupied d_{z^2} and $d_{x^2-y^2}$ orbitals. The crystal field splitting of the iron orbitals corresponds to a square pyramidal complex. The MLCT band is formed by states of mainly MLCT character, although some MC and LMCT character is also observed. These bands of states have strong multi-configurational character, and were not correctly represented in previous single-reference studies based on density-functional theory.[70, 73]

Quantum wavepacket dynamics has been performed using a vibronic model containing the main vibrational coordinates (heme doming, symmetry-breaking, rotational and dissociative modes). The evolution of diabatic state populations during the first 500 fs is shown in Figure 2.8a. The results have been obtained by sampling 10 independent quantum dynamics simulations with different initial conditions. The initial conditions are obtained by projecting the heme-CO geometries extracted from molecular dynamics snapshots of a myoglobin protein onto our vibronic model Hamiltonian. In the Figure, only the states which are mainly populated are shown. Following the dynamics of each spin manifold, a sequential transfer is found to occur, first from singlet to triplet (S→T) and then from triplet

to quintet (T→Q). The time constant for S→T transfer is estimated as 76 ± 15 fs, while the T→Q decay time is 429 ± 70 fs, in perfect agreement with the experimental rates of Cammarata *et al.* and Franzen *et al.*[60, 61, 75]. In the singlet manifold, we observe an abrupt decay of the ^{1}Q population, which is mainly transferred to the singlet ^{1}MLCT manifold. The rate for this transfer is estimated to 26 ± 7 fs. The overall reaction is thus sequential ^{1}Q→ ^{1}MLCT→ ^{3}MLCT → ^{5}MLCT (see Figure 2.8b). The initial step is a complete transfer from the ^{1}Q state to the ^{1}MLCT state, resulting in a negligible ^{1}Q population after ~100 fs. During the remaining transfer steps the three spin manifolds coexist. This is because the three manifolds are close in energy and strongly mixed through spin-orbit coupling. However, a clearly dominant spin state prevails during different intervals: singlet for t < 75 fs, triplet for 75 < t < 425 fs and quintet at later times.

In Figure 2.8c, we show the evolution of the Fe–C(O) and the Fe out-of-plane distances for the first 500 fs. Clearly, we observe damped large amplitude stretching motions for the Fe-C distance, which converges to a steady value of 2.2 Å. These motions are coherent, with a period of 42 fs. The Fourier transform of this signal shows a frequency of 800 cm^{-1}, much faster than the Fe–C(O) stretching frequency of 488 cm^{-1}. In 21 fs, the Fe–CO distance oscillates between the equilibrium distance (1.7-1.8 Å) and 2.5 Å. These are the typical distances at which the ground-state dissociation occurs.[62] After the first oscillation, the wavepacket is essentially in the MLCT bands, which are repulsive for CO such that the CO does not recombine and undergoes continued oscillations. Relaxation of the structure damps these oscillations until an equilibrium value of 2.2 Å is reached. Both the equilibrium value and the coherent frequency might be disrupted by the presence of the protein, an effect not included in the present model. This would introduce a faster decoherence of the Fe and CO interactions than what we observe in our model. As for the evolution of the Fe out-of-plane motion, we observe oscillations of ±0.2 Å around the initial position, in good agreement with recent time-resolved X-ray crystallography data.[59] As expected, the iron center reacts to the elongation of the Fe-CO distance by following the CO. Very rapidly, it oscillates back to the porphyrin plane, where part of the energy is dissipated to histidine. In the second and subsequent oscillations, the oscillations of Fe and CO are out of phase, indicating that the bond is photolyzed. A large dispersion of the Fe-C distances, which is appearing after 0.2 ps, is due to the delocalization of the wavepacket over the ^{1,3,5}MLCT bands, indicating an unbound CO atom. This dispersion is less marked for the Fe out-of-plane distance due to the more localized nature of the Fe atom, bounded strongly to the heme and the proximal histidine.

Experimental evidence shows that the CO is photolyzed within 70 fs.[60, 61, 75] In order to determine whether dissociation occurs from the singlet or the triplet state, we have considered a reduced model with only the singlet manifold, in which we eliminate the coupling parameters to the triplet and quintet states. In this case, an ultrafast transfer from Q→^{1}MLCT is still observed. The Fe–C(O) distance again exhibits oscillations with an amplitude of 0.7 Å. The fact that the amplitude is smaller than in the full model can be ascribed to the absence spin-orbit couplings which introduce strong mixing of the ^{1}MLCT surfaces with ^{3}MLCT states, that extend the region of oscillations. From these results, we can infer that the transfer to the ^{1}MLCT manifold is sufficient to dissociate the CO, although the presence of ^{3}MLCT favors further the photolysis. The dissociation is thus happening between 0.5 and 1.5 periods of the Fe-C(O) oscillation (20-60 fs), when the wavepacket is mainly in the ^{1}MLCT state.

After photolysis, the SCO mechanism brings the system sequentially to a HS state. After ~75 fs, the ^{3}MLCT band is clearly dominant, although a residual ^{3}MC participation is also observed. From the triplet manifold, a population transfer on the HS states is slowly building up, until it becomes dominant at around 400 fs. At this time, the wavepacket is distributed across the ^{5}MLCT and ^{5}MC excited states, staying trapped in these states. This is consistent with the slow time constant of ~3 ps observed in myoglobin, which has been attributed to a vibrational cooling due to the protein.[75, 81] Such excited state trapping has been observed recently in similar iron complexes.[33] This trapping can be understood in terms of the potential energy surfaces depicted in Figure 2.9. Upon excitation to the ^{1}Q band, a sequential ultrafast transfer, first to ^{1}MLCT and then to ^{3}MLCT occurs. These transfers are energetically favored and therefore extremely fast. In the ^{3}MLCT manifold, the wavepacket relaxes in a distribution of ^{3}MLCT and ^{3}MC states. The ^{3}MC state can undergo direct transfer to the ^{5}MLCT state, which is, however, energetically less favorable (and thus slower) than the singlet→triplet MLCT. The transition from the lowest ^{5}MLCT to the ^{5}MC state is energetically unflavored. On the other hand,

the ^{3}MC states are energetically separated from the rest of the states, such that a transfer to the ^{5}MC manifold becomes inefficient.

The initial structure is close to a C_{4v} symmetric geometry, in which the CO is in upright position and the porphyrin ring is close to the square planar conformation. The origin of the heme–CO bond is the typical σ-donation π-back-donation mechanism. A partial electron transfer from an occupied σ orbital of CO to an empty d_{z^2} orbital of Fe occurs simultaneously to a partial back transfer of electron density from the occupied d_{yz} and d_{xz} of Fe to the empty $\pi_y^{*,CO}$ and $\pi_x^{*,CO}$ orbital, respectively. At this geometry, the π orbitals of porphyrin do not overlap with the d-orbitals.

Activation of the dissociative vibration is fundamental for releasing the CO from the heme. This vibration is of a_g symmetry, as it is a vibration along the principal symmetry axis. However, the initial photon is absorbed exclusively in the porphyrin moiety. The porphyrin optical Q-state is E-symmetric, thus localized in the perpendicular plane with respect to the principal axis. This implies that the dissociative vibration is not activated in the quasi-C_{4v} initial geometry. The dissociation of CO thus requires an initial energy transfer from the porphyrin plane to the Fe center, which can only be possible by populating symmetry breaking vibrations. In the excited states, strong symmetry breaking of Jahn-Teller (JT) and pseudo Jahn-Teller (pJT) type occurs.[82, 83] The JT effect is the sudden increase of inter-state couplings between an E-degenerate state along symmetry breaking vibrational coordinates. These JT couplings induce a double-well minimum in the potential energy surfaces at elongated coordinates, while the energy is maximum at the initially symmetric structure. The pJT effect is analogous to the JT effect but applies to non-degenerate states, usually requiring more than a single vibration and more than one electronic state. Both mechanisms are characterized by strong vibronic couplings. In the particular case of the heme–CO complex, the E-symmetry of the Q-band can be broken by b_1 and b_2 vibrations, in the so-called E⊗b JT mechanism.[82] A representative vibration of this type is depicted in Figure 2.7d. Such a vibration is not directly coupled to the Fe–CO bond, but is fundamental to induce the interstate coupling between the Q-band and the MLCT band. The relaxation energy induced by such vibrations can be as large as 0.5 eV, which rapidly leads the wavepacket far from the Franck-Condon region. Large amplitude motions have been experimentally observed in similar iron complexes.[32]

In the heme–CO complex, the initially populated Q-band of porphyrin exhibits a negligible SOC with any other state. In general, SOC is strong when metal density is present in the electronic state. Therefore, the wavepacket is initially dominated by the symmetry breaking vibronic couplings in the singlet manifold, leading to the transition ^{1}Q→^{1}MLCT and ^{1}Q→^{1}MC. Both the ^{1}MLCT and ^{1}MC have strong spin-orbit coupling strength with ^{3}MLCT and ^{3}MC states respectively. In general, the SOC is strong when the selection rules $\Delta S = 1$ and $\Delta L = 1$ are obeyed. The latter condition implies that one of the d orbitals changes orientation between the triplet and the singlet state. For example, a strong coupling occurs between the singlet state of character $d_{xy} \rightarrow d_{x^2-y^2}$ with the triplet state of character $d_{xz} \rightarrow d_{x^2-y^2}$. We observe that singlet-triplet transitions occur at a faster rate in the MLCT band than within the MC states. At around 50 fs, the ^{3}MLCT population becomes dominant, at the expense of the singlet manifold populations. This is because there are a larger number of crossing points between MLCT states of different multiplicity than between MC states (see Figure 2.9). This results in a dominant population of ^{3}MLCT and ^{5}MLCT states during the spin-crossover transitions. The ^{3}Q band triplets, which were pointed out as playing a role in the photophysics of heme–CO, contribute negligibly to the dynamics.[75] The ^{1}MC state exhibits a residual population after 100 fs, following prevalent transfer to the ^{3}MC state, with a population which is two times smaller than the ^{3}MLCT population. Finally, the ^{3}MLCT→^{5}MLCT transfer builds up population in the quintet band. A ^{3}MC→^{5}MC transfer, however, is not observed, due to the fact that the ^{3}MC and ^{5}MC states do not cross in an accessible region. Our results show rather that the wavepacket remains trapped in the ^{5}MLCT band. The trapping occurs in regions of the energy surface where relaxation to lower states (in this case MC states) is slow due to large gaps and small vibronic couplings, whereas a band of electronic states acts as an energy dissipation force, thus localizing the wavepacket in an excited state. Such observation for heme–CO is in line with the valence tautomerism model of Franzen, Martin *et al.*[75] In summary, the existence of quasi-continuous MLCT bands degenerate to the ^{1}Q state and strong vibronic couplings are at the origin of the ultrafast photolysis and spin-crossover in the heme-CO complex.

Experimental confirmation: The predictions on the photochemical mechanism of myoglobin carbon monoxide (MbCO) photolysis, especially in respect to the structural changes induced by the photochemical reaction, have been confirmed by time-resolved serial femtosecond crystallography (TR-SFX).[19] In this work, it is shown also that the reaction of the protein scaffold reacts immediately to the dissociation of the gas and, therefore, energy dissipation due to the protein environment starts at the ultrashort timescale. This work is part of a big consortium lead by Prof. Ilme Schlichting, involving researchers from UK, USA, Germany, France and Switzerland. Experiments were performed at the SwissFEL. In my case, I performed new simulations of the structural deformations after photoabsorption including the protein environment, matching the experimental observations. These results have been published in Nature, 626, pages 905-911 (2024).

The hallmarks of MbCO photolysis are the observation of an unbound CO accompanied by changes in the iron's spin states and position. Since CO photodissociates from the haem iron within 70 fs, and in line with our previous TR-SFX experiment that showed full occupancy of CO* within the first time point, we did not anticipate any changes in CO* occupancy with time, given our time resolution. Unexpectedly, however, our electron density maps show an apparent increase of the occupancy of CO* with time for the 5 and 23 mJ cm^{-2} data and, to a lesser extent of the 101 mJ cm^{-2} data (see Fig. 2.10). Since the data series were collected during two beam times using different batches of crystals, different dark-state data and different laser settings, it is very unlikely that this finding is a product of experimental errors. Of note, at 5 and 23 mJ cm^{-2} the apparent increase of CO* occupancy occurs with time constants of approximately 350 and 450 fs, respectively, and are reminiscent of the damping constant of a coherent nuclear oscillation of CO* that was predicted by recent computational wavepacket analysis.[45] Since the time resolution of our experiment does not allow the predicted 1 Åamplitude, approximately 42 fs period oscillations to be resolved, they would manifest themselves simply as disorder due to distribution of the electron density over a large volume, resulting in an apparently low occupancy. As the oscillation damps, the CO* position "narrows" and its apparent occupancy converges to the value observed for the respective laser fluences at approximately 10 ps. According to this interpretation, at short time delays the crystallographic occupancy, which we determined from density peaks for the CO molecule, does not reflect the true yield of the photolysis reaction. Rather, the plateau value of the apparent crystallographic occupancy reflects the real photolysis yield. Accordingly, the time delay structures were all refined using the plateau value of the apparent crystallographic occupancy for the respective fluences.

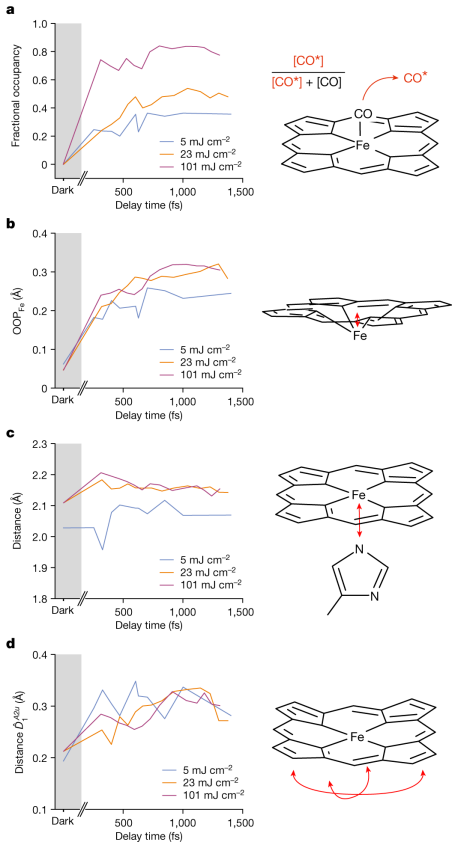

Figure 2.10: a, Apparent CO* occupancy (Fracc. occ.). Whereas at 5 and 23 mJ cm^{-2} there is a smooth, slow increase, at 101 mJ cm^{-2} there is a rapid initial rise, followed by an equally slow increase to the final amplitude. The 101 mJ cm^{-2} curve can be understood as a superposition of contributions from the multiphoton-excited "front end" of the crystals with the few-photon excited "rear end" of the crystals, resulting in almost instantaneous and apparently increasing occupancies of CO*, respectively. b, The iron-out-of-plane distance (OOP_{FE}) shows a larger amplitude with increasing fluence. c, The distance (Dist.) between haem iron and proximal His93 Nϵ2 atom, too shows differences between the fluences used, with the lowest fluence showing an oscillation and the highest fluence first going up and then settling at a lower amplitude. d, The haem doming ($\hat{D}_1^{A2u}$) also varies with the fluence, with again the lowest fluence showing an oscillation and the higher fluences do not.

2.2 Energy dissipation in photoactive proteins

2.2.1 Introduction

Absorption of a photon induces a photoreaction of the chromophore in the prosthetic group of photoactive proteins, which rapidly dissipates in the protein. The photon energy usually is transformed into chemical energy thanks to vibrations, an effect commonly known as vibrational energy redistribution. A clear example is myoglobin, that after photon absorption increases its volume by 100 Å^3 as determined by time-resolved X-ray scattering.[60] There is currently no methods that can connect the non-adiabatic dynamics induced by the electromagnetic field with the dissipation to the environment.

An important aspect in understanding dissipation is to classify the modes that induce reactivity (usually the QM atoms that undergo the photochemical reaction) and the modes that are part of the bath. Dissipation will thus occur between the "hot" modes of the QM system to the "cold" modes of the bath. A way to characterize this coupling is by computing the so-called total spectral density,

$$J_I(\omega) = \sum_i c_{i,I}^2 \delta(\omega - \omega_i). \tag{2.17}$$

This function contains all the information about the linear electron-nuclear couplings, the so-called vibronic couplings $c_{i,I}$. In the harmonic approximation, they can be easily computed with the so-called vertical gradient approach,

$$c_{i,I} = -\frac{(\nabla E_I | L_i)}{\omega_i^2}, \tag{2.18}$$

in which the ∇E_I is the mass-weighted gradient of electronic state I, L_i is the ith normal mode coordinate, and ω_i the corresponding frequency. Applying the separation into fragment local modes, we can split the total normal modes into two contributions for the QM subsystem (L_i^{QM}) and the MM subsystem (L_i^{MM})

$$L_i = L_i^{QM} + L_i^{MM}. \tag{2.19}$$

The local normal mode coordinates for the QM and MM subspaces have the same same dimension as L_i. This allows to separate the vibronic coupling in two contributions,

$$c_{i,I} = q_{i,I} + m_{i,I}, \tag{2.20}$$

in which the vibronic couplings projected on the QM and MM subspaces are defined as

$$\begin{aligned} q_{i,I} &= -\frac{\left(\nabla E_I | L_i^{QM}\right)}{\omega_i^2} \\ m_{i,I} &= -\frac{\left(\nabla E_I | L_i^{MM}\right)}{\omega_i^2}. \end{aligned} \tag{2.21}$$

We can thus partition the total spectral density, Eq. 2.17, to obtain

$$J_I(\omega) = J_I^{QM}(\omega) + J_I^{MM}(\omega) + 2J_I^{mix}(\omega), \tag{2.22}$$

in which we defined

$$\begin{aligned} J_I^{QM}(\omega) &= \sum_i q_i^2 \delta(\omega - \omega_i) \\ J_I^{MM}(\omega) &= \sum_i m_i^2 \delta(\omega - \omega_i) \\ J_I^{mix}(\omega) &= 2\sum_i q_i m_i \delta(\omega - \omega_i). \end{aligned} \tag{2.23}$$

The spectral densities $J_I^{QM}(\omega)$ and $J_I^{MM}(\omega)$ can be interpreted as the local dissipative functions for QM and MM respectively, i.e., the contribution of each subsystem to the initial dissipation of the photoexcited chromophore. The $J_I^{mix}(\omega)$ measures the degree of dissipation from one subsystem to the other. The application of this method requires on the one hand a localization of normal modes that I developed in 2016,[84] and on the other hand the analytic Hessian at the QM/MM level that I developed for electrostatic embedding in 2019-2021.[85–87] Despite the analytic Hessian is useful for many applications like the computation of infrared spectra of proteins or the vibrationally resolved absorption spectra, the main problem of applying this methodology for energy dissipation is that it requires a minimum of the internal energy, for which is not always easy to define in extended systems, or the definition of instantaneous normal modes.[88] In recent developments, I worked on an alternative formulation of dissipation based on QM/MM molecular dynamics in periodic boundary conditions.[89, 90] Despite not yet finished, I will show the developments based on an efficient formulation of electrostatic embedding QM/MM based on electrostatic potential fitted charge operators. In the final chapter, I will sketch the plans for simulating vibrational energy redistribution in photoactive proteins as part of my future research.

2.2.2 Electrostatic potential fitted charge operators

The electrostatic potential fitted method allows for an efficient account of the embedding interaction energy via the electrostatic interaction between the moments of a multipolar expansion of the electronic density of each fragment.[91] This is particularly suited for defining QM/MM interaction energy, since the non-bonded interactions in most MM forcefields are expressed by fixed multipolar moments. The advantage of having a representation of the QM density also in molecular moments is that all the QM/MM interaction terms are expressed like classical-like expressions, which facilitates the derivation and implementation of different QM/MM frameworks. In general, the energy is expressed as

$$E = E_{QM} + E_{MM} + E_{QM/MM}\,, \tag{2.24}$$

in which E_{QM} is the energy contribution from the gas phase Hamiltonian, E_{MM} is the classical contributions (comprising bonded and non-bonded interactions involving MM atoms only) and $E_{QM/MM}$ comprises all energy terms involving a QM and and MM centers (typically electrostatics, van der Waals, and angle, and torsions involving at least a QM center). For practicality, all purely classical terms involving a QM and MM centers are included in the MM energy definition hereafter, and the $E_{QM/MM}$ is only left with the non-bonded electrostatic interactions between QM and MM fragments. The QM/MM interaction can be written in many ways. Here, and without lose of generality, I will restrict the it to

$$E^1_{QM/MM} = \sum_A q_A \Phi_A\,, \tag{2.25}$$

in which $q_A = Z_A - Q_A$ is the atomic partial charge on center A, Z_A is the nuclear charge, A_A is the gross electronic population, and the potential Φ_A is the external potential on center A. Giving an analytic formula to q_A and Φ_A leads to different formulations of the QM/MM interaction energy and the associated Hamiltonian. For the charge operator, there are many possible choices for the atomic charges. For *ab initio* QM/MM, the usual choice is to take the electrostatic potential fitted (ESP) charges, which are used to parametrize most forcefields. For semi-empirical QM/MM implementations, especially for DFTB, we use Mulliken charges instead which are straightforwardly obtained from the overlap matrix expressed in an atomic basis. The ESP charges, instead, a numerical grid is constructed around the molecule on which one computes the electrostatic integrals

$$V_k = \sum_{\mu\nu} P_{\mu\nu} \int d\boldsymbol{r}\, \chi^*_\mu(\boldsymbol{r}) \frac{1}{|\boldsymbol{r} - \boldsymbol{r}_k|} \chi_\nu(\boldsymbol{r})\,, \tag{2.26}$$

where $P_\mu\nu$ is the density matrix, $\chi_\mu(\boldsymbol{r})$ are the atomic orbitals, and $\boldsymbol{r}_k$. In Ref. [87], we showed that it is particularly advantageous to define an atom-centered numerical grid $\boldsymbol{r}_k = \boldsymbol{r}_A + \boldsymbol{r}_l$, where $\boldsymbol{r}_A$ and $\boldsymbol{r}_l$ are

the QM atom coordinates and the coordinates of the points in a Lebedev sphere around A. Cut-offs are applied to exclude the grid points inside the van der Waals spheres of any atom in the molecule. This introduces some numerical noise (during molecular dynamics, for example) due to an inequivalent construction of grids during molecular dynamics, that can be partially remediated by using a dynamic restricted ESP procedure.[92] Alternatively, dynamic weights used in the fitting procedure might avoid the restriction of the ESP procedure with a definition of an arbitrary reference for each atomic charge. Including the analytic derivatives of the grid is important to conserve properties of the charge and the translational and rotational invariances of the energy and its gradients. The electrostatic integrals are then fitted via a least square procedure to be approximated by a point-charge based potential defined from the gross net charge on atom QM (Q_A) and the electrostatic kernel $\boldsymbol{T}_{k,A}$,

$$V_k = \sum_A T_{k,A} Q_A \,. \tag{2.27}$$

The solution of the least square problem leads to the optimal charges by the expression using the pseudo-inverse of $\boldsymbol{T}$,

$$Q_A = \sum_k \left[\left(\boldsymbol{T}^\dagger \boldsymbol{T} \right)^{-1} \boldsymbol{T}^\dagger \right]_{A,k} V_k \,. \tag{2.28}$$

This is an overdetermined system of equations, since usually the number of grid points is much larger than the number of QM atoms. Still, the use of Cholesky decomposition for performing the inversion of $\boldsymbol{T}^\dagger \boldsymbol{T}$ leads to stable solutions even during molecular dynamics. The resulting charges do not conserve the total number of electrons (N_{el}), but we showed that this can be easily corrected *a posteriori* without the need to constraint the linear system of equations,

$$Q'_A = Q_A - \sum_B \frac{(Q_B - N_{el})}{N_{QM}} \,. \tag{2.29}$$

Deriving the last two equations with respect to the density matrix, lead to the necessary information for building the interaction hamiltonian, namely

$$Q_{\mu\nu,A} = \sum_k \left[\left(\boldsymbol{T}^\dagger \boldsymbol{T} \right)^{-1} \boldsymbol{T}^\dagger \right]_{A,k} V_{\mu\nu,k} \,, \tag{2.30}$$

and

$$Q'_{\mu\nu,A} = Q_{\mu\nu,A} - \sum_B \frac{\left(Q_{\mu\nu,B} - S_{\mu\nu}\right)}{N_{QM}} \,, \tag{2.31}$$

leading to a very simple form of the interaction Hamiltonian when using the corrected charges,

$$H_{\mu\nu}^{QM/MM} = - \sum_A^{N_{QM}} \sum_{n=1} Q_{\mu\nu,A} \left(\Phi_A - \Phi_{av}\right) - S_{\mu\nu}\Phi_{av} \,, \tag{2.32}$$

where we defined the average potential $\Phi_{av} = N_{QM}^{-1} \sum_A^{N_{QM}} \Phi_A$.

2.2.3 Analytic derivatives

NOTE: Reprinted (adapted) with permission from J. Chem. Theory Comput. 2021, 17, 1, 538–548. Copyright 2021 American Chemical Society.

The analytic derivatives of the total energy (Eq. 2.24) are fundamental for the routine application of QM/MM methods. On the one hand, the first derivative (gradient) of the energy provides an efficient way to optimize geometries and to perform molecular dynamics (MD) at the QM/MM level. On the other hand, the analytic Hessians provide information on the topology of the minimum energy points, accelerate the optimization via second-order algorithms, provide a framework to search for transition

states, an analysis of the motions of the system based on vibrational normal modes, vibrational spectroscopies (such as infrared, Raman, vibrational circular dichroism or rotational optical activity) and allow to compute electron-vibrational couplings. During the Ph.D. project of Karno Schwinn, we performed several developments in that direction that I summarize in this chapter.[85, 86, 93, 94] Here, we will focus on the derivative of the QM/MM interaction energy, since the purely MM terms have simple analytic derivatives from the classical expressions and QM terms have been lengthy discussed in the literature.[95] In addition, we will only focus on the derivative of the first-order interaction term (Eq. 2.64).

Gradient: The derivative with respect to QM and MM centers is given by

$$E^{x}_{QM/MM} = -\sum_A Q^{(x)}_A \Phi_A - \sum_A Q_A \Phi^x_A \tag{2.33}$$

$$E^{\tilde{x}}_{QM/MM} = -\sum_A Q_A \Phi^{\tilde{x}}_A, \tag{2.34}$$

where we used the short-hand notation of $E^x = \partial E/\partial x$. The first equation correspond to QM center derivative, whereas the second is the derivative with respect to an MM center. The parenthesis in a derivatives implies that the density matrix is maintained fixed in the derivative. Such a derivative can be avoided in the energy gradient of self-consistent field wavefunctions as shown in Ref. [95].

Hessian: The construction of the second derivative requires the full derivative of the atomic charge operators with respect to QM and MM centers, since the Hessian is given by the QM-QM, QM-MM, MM-QM and MM-MM blocks given by

$$\begin{aligned}
E^{xy}_{QM/MM} &= -\sum_A Q^{(xy)}_A \Phi_A - \sum_A Q^{(x)}_A \Phi^y_A - \sum_A Q^y_A \Phi^x_A + \sum_A q_A \Phi^{xy}_A \\
E^{x\tilde{y}}_{QM/MM} &= -\sum_A Q^{(x)}_A \Phi^{\tilde{y}}_A + \sum_A q_A \Phi^{x\tilde{y}}_A \\
E^{\tilde{x}y}_{QM/MM} &= -\sum_A Q^{y}_A \Phi^{\tilde{x}}_A + \sum_A q_A \Phi^{xy}_A \\
E^{\tilde{x}\tilde{y}}_{QM/MM} &= -\sum_A Q^{\tilde{y}}_A \Phi^{\tilde{x}}_A + \sum_A q_A \Phi^{\tilde{x}\tilde{y}}_A .
\end{aligned} \tag{2.35}$$

To construct the full Hessian, the first and second derivatives of the electrostatic potential are required, which have straightforward classical expressions. The derivative of the ESPF charge operators are constructed by first and second derivatives of the operators at fixed density matrix (symbolized as a derivative superscript in parenthesis). We found that deriving Eq. 2.28 before the inversion of $\boldsymbol{T}$ lead to computationally more compact and efficient equations to implement,

$$Q^x_A = \sum_k \left[\left(\boldsymbol{T}^\dagger \boldsymbol{T} \right)^{-1} \boldsymbol{T}^\dagger \right]_{A,k} \left[V^x_k - \sum_B \boldsymbol{T}^x_{k,B} Q_B \right]. \tag{2.36}$$

$$Q^{xy}_A = \sum_k \left[\left(\boldsymbol{T}^\dagger \boldsymbol{T} \right)^{-1} \boldsymbol{T}^\dagger \right]_{A,k} \left[V^{xy}_k - \sum_B T^{xy}_{k,B} Q_B + T^x_{k,B} Q^y_B + T^y_{k,B} Q^x_B \right]_k . \tag{2.37}$$

Finally, the first derivative of the density matrix with respect to QM and MM centers is needed, that requires the solution of auxiliary coupled-perturbed equations to make the computations tractable as described in the next section.

Atomic charge derivatives: The derivative of the density matrix with respect to MM centers ($\boldsymbol{P}^{\tilde{x}}$) would require the solution of several thousands of coupled perturbed equations. At the time we performed our study, only approximate solutions were given.[96, 97] Thanks to the use of Eq. 2.64, we managed to workaround the computation of MM coupled-perturbed equations, by defining an auxiliary set of coupled-perturbed equations, the Q-vector method. The derivative of the atomic charge with respect to MM atoms reads

$$Q^{\tilde{x}}_A = -\sum_{\mu\nu} P^{\tilde{x}}_{\mu\nu} Q_{\mu\nu,A}. \tag{2.38}$$

in which $\boldsymbol{P}^{\tilde{x}} = \boldsymbol{C}^{*,\tilde{x}}\boldsymbol{C} + \boldsymbol{C}^{*}\boldsymbol{C}^{\tilde{x}}$. The derivative of the molecular orbital coefficients by solving the coupled-perturbed Kohn-Sham equation

$$\sum_{jb}(A+B)_{ai,jb}U_{jb} = -F^{\tilde{x}}_{ai}. \tag{2.39}$$

The interaction Hamiltonian derivative with respect to MM atoms is simply

$$F^{\tilde{x}}_{ai} = -\sum_{A} Q_{ai,A}\Phi^{\tilde{x}}_{A}. \tag{2.40}$$

This allows to solve an auxiliary coupled perturbed equation for each of the charge operators $Q_{ai,A}$. The Q-vector coupled perturbed equations scale with the number of QM atoms (which is much smaller than the MM) and reads thus

$$\sum_{jb}(A+B)_{ai,jb}\tilde{Q}_{jb,A} = -Q^{\tilde{x}}_{ai,A}. \tag{2.41}$$

From the solution of these equations, we can straightforwardly construct Eq. 2.42 exactly

$$Q^{\tilde{x}}_{A} = -\sum_{ai}\sum_{B}\tilde{Q}_{ai,B}\tilde{Q}_{ai,A}\Phi^{\tilde{x}}_{B}. \tag{2.42}$$

From this equation and the coupled-perturbed equation (with respect to QM atoms), the full "polarization" terms of the Hessian (terms that depend of derivative of the density matrix) in Eq. 2.35.

2.2.4 Vibrationally resolved absorption spectra

NOTE: Reprinted (adapted) with permission from J. Chem. Theory Comput. 2020, 16, 6, 3816–3824. Copyright 2020 American Chemical Society.

In Fig. 2.11, I showed that the normal modes and the vibrationally resolved absorption spectrum that we computed for plant crypthochrome. For analyzing the normal modes, we employed the participation ratio, which measures the degree of delocalization of normal modes. In this case, most normal modes are localized, besides the low frequency modes, which span the whole protein. In addition, we added a second measure, the QM character measure, defined as

$$QM(\omega_i) = \sum_{j\in QM}^{3N}\left({}^{0}L^{\dagger}_{i,j}\right)^2. \tag{2.43}$$

With that measure, we observe that most modes are pure protein modes, not involving the QM fragment. However, between 1000 and 2000 cm^{-1} have mixed QM and MM character. This has an effect when computing the vibrationally resolved spectrum. The comparison between the experimental and theoretical vibrationally resolved absorption spectrum shows a perfect agreement. The first peak is composed of a single $\pi \rightarrow \pi^*$ transition, whereas the second peak is composed of three higher energy transitions of mainly $\pi \rightarrow \pi^*$ character also.

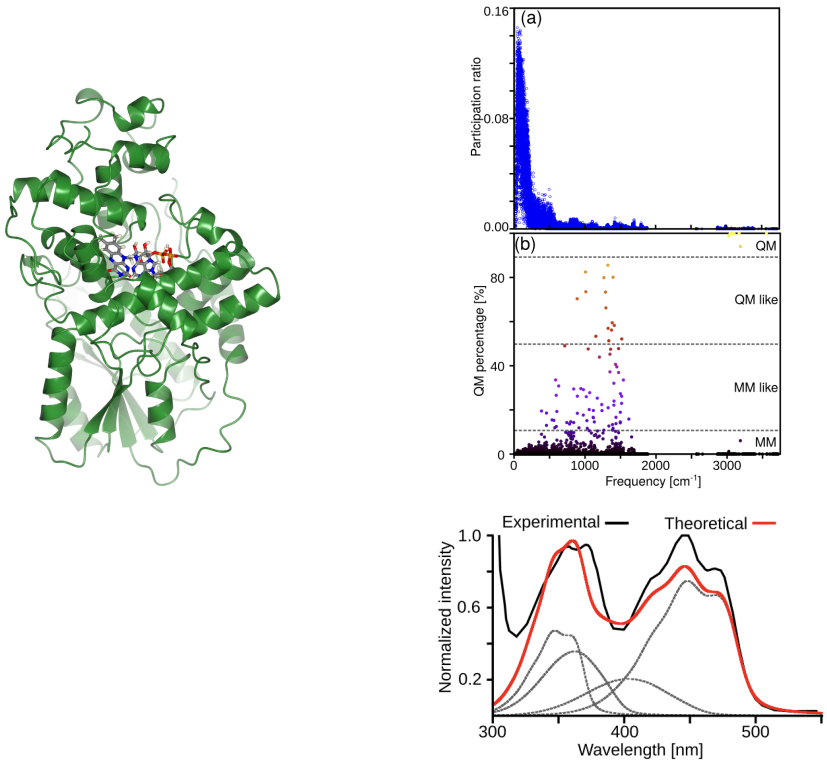

Figure 2.11: (left) Schematic representation of *Arabidopsis thaliana* plant cryptochrome; (middle) normal mode analysis and partition ratio; (right) vibrationally resolved spectrum.

2.2.4.1 Infrared spectrum

NOTE: Reproduced from Ref. M. Huix-Rotllant, K. Schwinn and N. Ferré, Phys. Chem. Chem. Phys., 2021, 23, 1666 DOI: 10.1039/D0CP06070D with permission from the PCCP Owner Societies.

The construction of the Hessian allowed to perform several applications. An obvious example is the analysis of infrared spectra, which can be computed as,[98]

$$A = \frac{N_A}{6c^2\epsilon_0\hbar}\sum_k^{N_{\text{vib}}}\omega_k\left|\langle\nu_i|\frac{\partial\boldsymbol{\mu}}{\partial\Delta X}_k|\nu_f\rangle\right|^2, \tag{2.44}$$

in which i and f refer to the initial and final state, ω is the normal mode harmonic frequency, c is the light velocity, ϵ_0 is the permittivity in vacuum. The induced dipole with respect to a normal mode displacement $\Delta\boldsymbol{X}$ is given by,

$$\frac{\partial\boldsymbol{\mu}}{\partial\Delta\boldsymbol{X}}_k = \boldsymbol{L}_k^\dagger\boldsymbol{M}^{-1/2}\frac{\partial\boldsymbol{\mu}}{\partial\boldsymbol{R}}. \tag{2.45}$$

Here, $\boldsymbol{\mu}$ is the induced dipole moment from an external electric field. Indeed, in the presence of an external static electric field $\vec{\mathscr{E}}$, the total energy can be expanded in the Taylor series

$$E(\vec{\mathscr{E}};\boldsymbol{R}) = E(\boldsymbol{0};\boldsymbol{R}) - \sum_f \mu_f(\boldsymbol{R})\vec{\mathscr{E}}_f + \mathscr{O}(\vec{\mathscr{E}}^2) \tag{2.46}$$

in which $f = x, y, z$ indicates the direction of the electric field. Many derivations of electric field

derivative using analytic derivative method exist in the literature. Here, we follow the derivation of Amos.[**Amos85**] The induced electric dipole moment can be defined as the derivative with respect to the induced electric field operator $\boldsymbol{e}^f$

$$\mu_f(\boldsymbol{R}) = -\sum_{\mu\nu} P_{\mu\nu}\langle\mu|\boldsymbol{r}_f|\nu\rangle = \sum_{\mu\nu} P_{\mu\nu}(\boldsymbol{R})\, e^f_{\mu\nu}(\boldsymbol{R}_{\mathrm{QM}})\,, \tag{2.47}$$

in which the atomic orbital density matrix $\boldsymbol{P}$ is defined as $P_{\mu\nu} = \sum_i C_{\mu,i} C^*_{i,\nu}$, where $C_{\mu,i}$ is the molecular orbital coefficient. Hereafter, indexes $i, j, \ldots$ are used for occupied orbitals, $a, b, \ldots$ are used for virtual orbitals and $p, q, \ldots$ are unspecified. The dipole moment derivatives with respect to a QM atom are given by

$$\mu_f^{X_C} = 4\sum_{pi} U_{pi}^{X_C} e^f_{pi} + \sum_{\mu\nu} P_{\mu\nu} e^{fX_C}_{\mu\nu} \tag{2.48}$$

The derivatives of the induced dipole with respect to an MM atom are simply given by

$$\mu_f^{X_I} = 4\sum_{pi} U_{pi}^{X_I} e^f_{pi}\,. \tag{2.49}$$

This equation would require the solution of a set of coupled-perturbed equations for each MM perturbation, which would make the simulation intractable. Similar to the atomic charge derivatives, we can workaround this by solving an auxiliary set of equations, the $\tilde{Q}$-vector technique,[0] to obtain

$$\mu_f^{X_I} = 4\sum_{A}^{\mathrm{N_{QM}}}\sum_{ai} \tilde{Q}_{A,ai}\left(\Phi_{av} - \phi_A\right)^{X_I} e^f_{ai} \tag{2.50}$$

It is to be noted that this corresponds to the dipole response contribution due to MM motions, but does not lead to the full IR spectrum of the MM subsystem. The main contribution is usually obtained from the Fourier transform of the real-time dipole-dipole autocorrelation function.[99] The presented method here is rather useful to represent the QM frequencies with the steric and electrostatic effects of the MM environment taken into account in addition to the mode-mixing between the QM and MM systems.

In Ref. [84], we described a strategy to decompose normal modes in fragments. The method is based on the fact that submatrices of a positive semi-definite matrix are also positive semi-definite. The total Hessian at a true minimum is positive semi-definite, the frequencies of which are interpreted as the characteristic frequencies of vibration. Therefore, the submatrices grouping the atoms of a pre-defined fragment can be interpreted as the local modes of the fragment. The local normal modes can be obtained from the fragment Hessians, defined from the total Hessian as $[H_F]_{A,B} = \delta_{A\in F, B\in F}\partial^2 E/\partial\boldsymbol{R}_A\partial\boldsymbol{R}_B$. Here, the total Hessian is organized in such a way that the atoms of a fragment are consecutively appearing in the Hessian blocks. From the fragment Hessians, we obtained the local normal modes and frequencies,

$$\boldsymbol{L}_F^\dagger \boldsymbol{H}_F \boldsymbol{L}_F = \boldsymbol{\omega}_F^2\,. \tag{2.51}$$

Note that the local Hessian and the local normal modes have the dimension of the total Hessian. The sum $\boldsymbol{L}_{loc} = \sum_F^{N_{\mathrm{frag}}} \boldsymbol{L}_F$ gives a block diagonal transformation for the total Hessian,

$$\boldsymbol{H}_{loc} = \boldsymbol{L}_{loc}^\dagger \boldsymbol{H} \boldsymbol{L}_{loc}\,. \tag{2.52}$$

The transformed local Hessian $\boldsymbol{H}_{loc}$ consists of block diagonal matrices for the fragments that are simply the fragment frequencies, and the off-diagonal blocks lead to the fragment vibrational couplings. In addition, the total normal modes can be decomposed as a linear combination of local modes

$$\boldsymbol{L}_i = \sum_j \alpha^i_j \left[\boldsymbol{L}_{loc}\right]_j\,. \tag{2.53}$$

Finally, the local normal modes can be used in Eq. 2.45 to decompose the IR spectrum in terms of

fragments.

In Fig. 2.12, a summary of the main results obtained from these infrared spectra of *arabidopsis thaliana* plant cryptochrome are summarized. The total infrared spectrum of the oxidized form of flavin adenine dinucleotide (FAD) has been decomposed in its subunits. This analysis simplifies the interpretation of the infrared spectrum, from which one can clearly distinguish the adenine and isoalloxazine vibrations in the high frequency zone from the diphosphate region between 1000-1200 cm^{-1}. Experimentally, the difference infrared spectrum is frequently used for studying the spectroscopic signals of a protein before and after a reaction. This allows to exclude the fixed parts of the spectrum (the amide peaks) and focus only on the vibrations that significantly change. In the case of cryptochrome, after blue light absorption, the prosthetic group is reduced with one electron and neutralized with a proton from the protein. The main signals come from the $N-H$ vibrations (bending in lower frequency and stretching in higher frequency) that we were able to accurately reproduce.

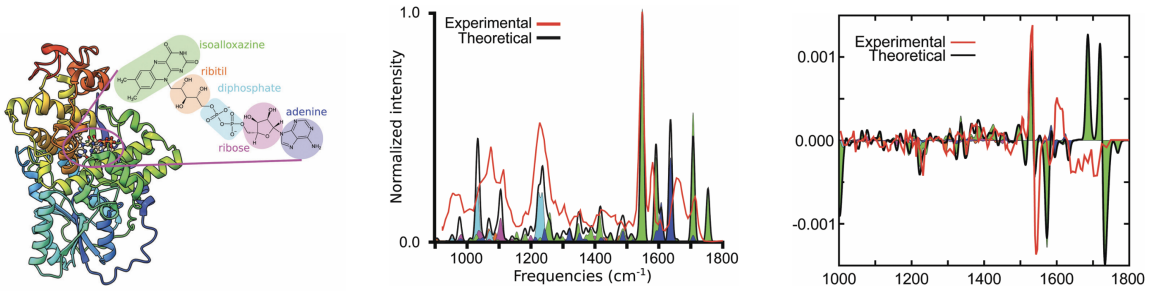

Figure 2.12: (left) Schematic representation of *Arabidopsis thaliana* plant cryptochrome with inlay on its prosthetic group and its decompoposition on fragments; (middle) Infrared spectrum of cryptochrome decomposed in the local normal mode contributions of each subunit; (right) Difference infrared spectrum between the neutral reduced and the oxidized forms.

2.2.5 Non-adiabatic dynamics of thymine

NOTE: Reprinted (adapted) with permission from J. Chem. Theory Comput. 2023, 19, 1, 147–156. Copyright 2023 American Chemical Society.

Here we formulate an electrostatic embedding QM/MM method for excited states, combining the strengths of MRSF-TDDFT and electrostatic embedding QM/MM using electrostatic potential fitted (ESPF) charges. We recently developed the ESPF QM/MM method including total charge conservation and grid derivative effects up to the second derivative of the energy for ground-state single-determinant wavefunctions solutions of a set of Fock equations, showing an overall linear scaling with respect to MM subsystem size.[86, 87, 93] A particular transformation to spinor-like mixed spin functions combines $|\alpha\alpha\rangle$ ($M_S = +1$) and $|\beta\beta\rangle$ ($M_S = -1$) of a restricted open Hartree-Fock (ROHF) triplet into a *hypothetical* single reference[100, 101] in the MRSF-TDDFT formulation.

The total energy of an excited state I with a total spin S at the QM/MM level is given by,

$$E_I^{[S]} = E_{I,\mathrm{QM}}^{[S]} + E_{\mathrm{MM}}\,. \tag{2.54}$$

in which the QM energy is $E_{I,QM}^{[S]} = E_{\mathrm{ref}} + \Omega_I^{[S]}$ is the sum of the reference state energy and the MRSF excitation energy $\Omega_I^{[S]}$. In an electrostatic embedding QM/MM formulation these energies are obtained from the solution of a hamiltonian containing the interaction term between the QM and MM systems.

Using electrostatic potential fitting charges, we can define such interaction as a one-electron operator

$$h_{\mu\nu}^{\mathrm{ESPF}} = \sum_{A}^{N_{\mathrm{QM}}} \left(\Phi^{\mathrm{av}} - \phi_A\right) Q_{A,\mu\nu} - \Phi^{\mathrm{av}} S_{\mu\nu}\,, \tag{2.55}$$

in which ϕ_A is the external electrostatic field generated by the MM charges on QM center A, the average external field is defined as $\Phi^{\mathrm{av}} = N_{\mathrm{QM}}^{-1} \sum_A \phi_A$, $\mathbf{S}$ is the overlap matrix and $\mathbf{Q}_A$ is the net charge population of QM center A, which is defined as

$$Q_{A,\mu\nu} = \sum_{k}^{N_{\mathrm{grid}}} T_{A,k}^{+} \langle \chi_\mu | \frac{1}{|\mathbf{r} - \mathbf{r}_k|} | \chi_\nu \rangle\,. \tag{2.56}$$

Here, $\mathbf{r}_k = \mathbf{R}_A + \alpha \cdot \mathbf{r}_l$ refers to a Lebedev grid point, constructed on the QM centers by adding a Lebedev points $\mathbf{r}_l$ multiplied by a factor α that ensures that the grid points lay outside the Van der Waals surface of the molecule. The matrix $\mathbf{T}^+$ is defined as $\mathbf{T}^+ = (\mathbf{T}^\dagger \mathbf{T})^{-1} \mathbf{T}^\dagger$ and corresponds to the pseudoinverse of the electrostatic kernel $\mathbf{T}_{k,A} = |\mathbf{r}_k - \mathbf{R}_A|^{-1}$. The electrostatic one-electron integrals are constructed on a grid around the QM atoms. To respect the symmetry properties of the Hamiltonian in an electrostatic embedding formulation, it is advantageous that the grid is atom-centred.[0]

The MRSF excitation energies are obtained from poles of the response function of the mixed reference (within the Tamm-Dancoff approximation)

$$\sum_{rs} A_{pq,rs}^{[S]} X_{rs,I}^{[S]} = X_{pq,I}^{[S]} \Omega_I^{[S]}\,, \tag{2.57}$$

for the singlet ($S = 0$) and the triplet ($S = 1$) states. The orbital Hessian matrix consists of two matrices, i.e. $\mathbf{A}^{[S]} = \mathbf{A}^{[S](0)} + \mathbf{A}^{'[S]}$. On the one hand, the spin-pairing coupling matrix ($\mathbf{A}^{'[S]}$) is a *posteriori* coupling between the responses from the two references. This coupling is given by a series of two-electron integrals, and thus, remains equivalent in the ESPF QM/MM formulation. On the other hand, $\mathbf{A}^{[S](0)}$ is given by

$$\begin{aligned} A_{pq,rs}^{[S](0)} &= U_{pq}^{[S]} \Big[\delta_{pr} F_{qs}^{\mathrm{p}} \\ &- \delta_{qs} F_{pr}^{\mathrm{h}} - c_H (pr|sq) \Big] U_{rs}^{[S]} \end{aligned} \tag{2.58}$$

in which

$$\begin{aligned} F_{pr}^{\mathrm{h}} &= h_{pq}^{0} + h_{pq}^{\mathrm{ESPF}} + \sum_i \left[2(pq|ii) - c_H (pi|iq) \right] + \sum_x \left[(pq|xx) - c_H (px|xq) \right] \\ F_{pr}^{\mathrm{p}} &= h_{pq}^{0} + h_{pq}^{\mathrm{ESPF}} + \sum_i \left[2(pq|ii) - c_H (pi|iq) \right] + \sum_x (pq|xx), \end{aligned} \tag{2.59}$$

h_{pq}^0 and $(pq|rs)$ are the one- and two-electron integrals, respectively, c_H is the mixing coefficient for the exact Hartree-Fock exchange, and $U_{pq}^{[S]}$ is the dimensional-transformation matrix introduced previously.[101] in such a manner that a majority of existing SF-TDDFT codes can be utilized for the implementation of MRSF-TDDFT. We can find the ESPF contribution in the Fock matrix as an additional mean-field contribution. For these expressions, the analytic gradients were also implemented.

MRSF-QM/MM calculations for four excited states were performed on the 478 snapshots from the QM/MM-MD trajectories at S_0 state, which was utilized to produce a simulated UV spectrum and the results, where distinct two bands of near ~ 220 and ~ 260 nm are observed, faithfully reproducing previous studies of two bands in aqueous conditions. (comparison with experiments requires a red-shifted of the theoretical spectrum by 40 nm.) In the case of thymine in gas phase, the S_1 and S_2 are dark $n\pi^*$ and bright $\pi\pi^*$ states, respectively.[102] The relative order of bright and dark states tends to be reversed in QM/MM scheme with the bright S_1 and bright S_2 ratio of 7:3. The lowering bright state energy in a polar solution can be understood by its polar zwitterionic character.

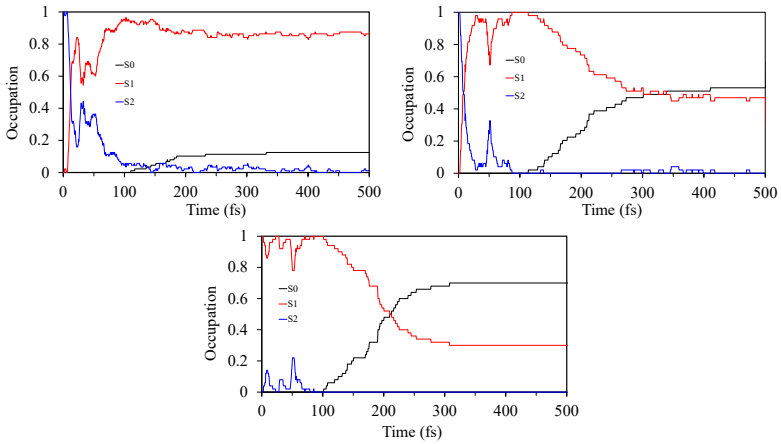

Figure 2.13: Time evolution of thymine populations from gas phase NAMD from initial excitation to S_2 state (left). The middle and right are the same population changes of solution QM/MM-NAMD. The former and the latter are initially excited to S_2 and S_1, respectively.

Therefore, contrasting to the NAMD simulation in gas phase[102], the three state (S_0, S_1 and S_2) TSH QM/MM-NAMD simulations with MRSF/BH&HLYP were initiated in the bright S_1 state on the 30 randomly selected snapshots of ground state QM/MM-MD. This particular bright S_1 state corresponds to the lower energy bright state of the two distinct bands.

The time evolution of the three state populations up to 500 fs are presented in the Fig. 2.13, where the corresponding NAMD results in gas phase are also shown. The initial S_2 population is quickly transferred to S_1 in the gas phase by the characteristic BLA (bond-length alternation) vibrations in about ~ 100 fs. On the other hand, the same change is not observed in the solution phase except for minor $S_1 \rightarrow S_2$ internal conversions, since the NAMD was started from S_1 state. In both cases, the ground state populations start to appear after ~ 100 fs. Contrasting to the slow S_0 population increase in gas phase, an abrupt changes are seen in solution reaching 50% ~ 70% of the total population in 300 fs, regardless of initial excitation of S_2 or S_1. This QM/MM-NAMD result is consistent with recent liquid jet time-resolved photoelectron spectroscopy[103], where the lower lying $\pi\pi^*$ (S_1) state is found to decay in ~ 400 fs independent of pump photon energy.

2.2.6 Periodic boundary conditions

NOTE: Reprinted (adapted) with permission from J. Chem. Theory Comput. 2024, 20, 10, 4338–4349. Copyright 2024 American Chemical Society.

The periodic boundary condition (PBC)-adapted electrostatic interaction energy between the QM and MM subsystems can be written in simple terms from electrostatic potentials as

$$E_{\text{int}} = \sum_{A}^{N_{\text{QM}}} q_A \left(\Phi_A^{MM} + \frac{1}{2} \Phi_A^{\text{QM}} \right). \tag{2.60}$$

The ESPF charges q_A interact with two external potentials: Φ^{MM} originating from all the permanent MM point charges and Φ^{QM} originating from the ESPF point charges located in the images of the original cell (replica cells). Deriving E_{int} with respect to the density matrix results in a compact form of

the interaction Hamiltonian,

$$h_{\mu\nu}^{\mathrm{ESPF}} = -\sum_{A}^{N_{\mathrm{QM}}} Q_{A,\mu\nu}\left(\Phi_A^{\mathrm{MM}} + \Phi_A^{\mathrm{QM}}\right), \tag{2.61}$$

to be added in the gas phase Fock operator of the QM subsystem. Using standard Ewald sums, the QM and MM electrostatic potentials have the following expressions. The MM potential is

$$\Phi_A^{\mathrm{MM}} = \sum_{\mathbf{n}=\mathbf{0}} \sum_{i=1}^{N_{\mathrm{MM}}} \frac{q_i}{|\mathbf{r}_{Ai\mathbf{n}}|}\mathrm{erfc}\left(\beta|\mathbf{r}_{Ai\mathbf{n}}|\right) + \frac{1}{\pi V}\sum_{\mathbf{m}\neq\mathbf{0}} \frac{e^{-\frac{\pi^2\mathbf{m}^2}{\beta^2}}}{\mathbf{m}^2}\mathrm{Re}\left[e^{-2\pi i\mathbf{m}\cdot\mathbf{r}_A} S_{\mathrm{MM}}(\mathbf{m})\right],$$

in which V is the volume of the cell, β is the Ewald range-separation parameters, N_{MM} is the total number of atoms in the MM region, $\mathbf{r}_{Ai\mathbf{n}} = |\mathbf{r}_A - \mathbf{r}_i + \mathbf{n}L|$ is the distance between QM atom A in the original cell and any MM atom i, and $S_{\mathrm{MM}}(\mathbf{m})$ is the structure factor (vide infra). The sum $\boldsymbol{n}$ runs over all the original and replica cells, while the sum $\boldsymbol{m}$ runs over the reciprocal space vectors.

The QM potential has a similar expression which is

$$\begin{aligned}\Phi_A^{\mathrm{QM}} = &\sum_{\mathbf{n}\neq\mathbf{0}} \sum_{B=1}^{N_{\mathrm{QM}}} \frac{q_B}{|\mathbf{r}_{AB\mathbf{n}}|}\mathrm{erfc}\left(\beta|\mathbf{r}_{AB\mathbf{n}}|\right) + \frac{1}{\pi V}\sum_{\mathbf{m}\neq\mathbf{0}} \frac{e^{-\frac{\pi^2\mathbf{m}^2}{\beta^2}}}{\mathbf{m}^2}\mathrm{Re}\left[e^{-2\pi i\mathbf{m}\cdot\mathbf{r}_A} S_{\mathrm{QM}}(\mathbf{m})\right] \\ &- \frac{2\beta}{\sqrt{\pi}} q_A - {\sum_{B=1}^{N_{\mathrm{QM}}}}' \frac{q_B}{|\mathbf{r}_{AB\mathbf{0}}|}\mathrm{erf}\left(\beta|\mathbf{r}_{AB\mathbf{0}}|\right).\end{aligned} \tag{2.62}$$

The last two terms in Eq. 2.62 arise to correct respectively for the spurious self-interaction and the double-counting of long-range QM-QM interactions in the original cell.[104] In the previous equations, the structure factors S_{QM} and S_{MM} are given by

$$\begin{aligned} S_{\mathrm{QM}}(\boldsymbol{m}) &= \sum_{A}^{N_{\mathrm{QM}}} q_A e^{2\pi i\mathbf{m}\mathbf{r}_A} \\ S_{\mathrm{MM}}(\boldsymbol{m}) &= \sum_{i}^{N_{\mathrm{MM}}} q_i e^{2\pi i\mathbf{m}\mathbf{r}_i}. \end{aligned} \tag{2.63}$$

Analytic gradient: The derivative of the total QM/MM energy (Eq. **??**) with respect to any parameter x is given by $d^x E = d^x E_{\mathrm{QM}} + d^x E_{\mathrm{MM}} + d^x E_{int}$. Hereafter, we use the shorthand notation for derivatives as a superscript, which represents a partial derivative ($\partial^x E = \partial E/\partial x$) or a total derivative ($d^x E = dE/dx$). Both derivatives are expressed as E^x if there is no need to specify the type of derivative. The expression for the $d^x E_{\mathrm{QM}}$, that is, the gas phase QM energy, depends on the methodology used, but for most common electronic structure methods, there exist analytic formulas for computing it.[105] Similarly, the $d^x E_{\mathrm{MM}}$ contains classical terms with simple analytic formulas for the computation of gradients. Therefore, here we focus on the derivative of the QM/MM interaction energy. In the following, firstly, we discuss the derivatives of the ESPF atomic charges, a quantity that is important for all further development. Then, we detail the computation of the interaction energy partial derivatives with respect to QM and MM centers. In the last part, we describe also the partial derivatives with respect to the lattice parameters, necessary to compute for example the pressure.[106]

The derivation of the interaction energy with respect to a generic atom (i.e., QM or MM) is reported in detail in SI Section 1. If we consider a QM atom B, the derivative can be written as

$$E_{int}^{x_B} = -\sum_{A}^{N_{\mathrm{QM}}} q_A^{x_B}\left(\Phi_A^{MM} + \Phi_A^{\mathrm{QM}}\right) + \sum_{A}^{N_{\mathrm{QM}}} q_A\left(\Phi_A^{MM,x_B} + \frac{1}{2}\Phi_A^{QM,(x_B)}\right). \tag{2.64}$$

where the first term contains the derivative of the ESPF charges and the QM and MM Ewald potentials defined in Eqs. **??** and 2.62. The second term requires, instead, the derivatives of the Ewald potentials with respect to a QM atom coordinate. In the following, we give explicit expressions for constructing the derivative of the total energy. The general expression of the QM potential on QM atom center A

derivative with respect to the coordinate of QM atom B is given by

$$\Phi_A^{QM,(x_B)} = -\sum_{B=1}^{N_{\mathrm{QM}}}{}' q_B\, d^{x_B}\left(\frac{1}{|\mathbf{r}_{AB\mathbf{0}}|}\right) + \sum_{\mathbf{n}=0}\sum_{B=1}^{N_{\mathrm{QM}}}{}' q_B\, d^{x_B}\left[\frac{\mathrm{erfc}\left(\beta|\mathbf{r}_{AB\mathbf{n}}|\right)}{|\mathbf{r}_{AB\mathbf{n}}|}\right] + \frac{1}{\pi V}\sum_{\mathbf{m}\neq 0}\frac{e^{-\frac{\pi^2\mathbf{m}^2}{\beta^2}}}{\mathbf{m}^2}\, d^{(x_B)}\left\{\mathrm{Re}[e^{-2\pi i\mathbf{m}\cdot\mathbf{r}_A}S_{\mathrm{QM}}(\mathbf{m})]\right\}. \tag{2.65}$$

The derivatives of QM potentials with respect to MM displacements are zero since the potential only depends on QM coordinates. Therefore, the first derivative with respect to an MM atom coordinate x_i reduces to

$$E_{int}^{x_i} = \sum_{A}^{N_{\mathrm{QM}}} q_A \Phi_A^{\mathrm{MM},x_i}, \tag{2.66}$$

where the derivative of the MM potential on center A with respect to an MM atom i, is given by,

$$\Phi_A^{\mathrm{MM},x_i} = \sum_{\mathbf{n}=\mathbf{0}}\sum_{i=1}^{N_{\mathrm{MM}}} q_i\, d^{x_i}\left[\frac{\mathrm{erfc}\left(\beta|\mathbf{r}_{Ai\mathbf{n}}|\right)}{|\mathbf{r}_{Ai\mathbf{n}}|}\right] + \frac{1}{\pi V}\sum_{\mathbf{m}\neq\mathbf{0}}\frac{e^{-\frac{\pi^2\mathbf{m}^2}{\beta^2}}}{\mathbf{m}^2}\, d^{x_i}\left\{\mathrm{Re}\left[e^{-2\pi i\mathbf{m}\cdot\mathbf{r}_A}S_{\mathrm{MM}}(\mathbf{m})\right]\right\}. \tag{2.67}$$

The coordinate transformation $\boldsymbol{r} = \boldsymbol{hu}$ transforms fractional ($\boldsymbol{u}$) into Cartesian coordinates ($\boldsymbol{r}$) through the cell tensor $\boldsymbol{h}$, which is defined by its transpose as

$$\boldsymbol{h}^{\mathrm{T}} = \begin{pmatrix} a & b\cdot\cos(\gamma) & c\cdot\cos(\beta) \\ 0 & b\cdot\sin(\gamma) & -c\cdot\sin(\beta)\cdot\cos(\alpha^*) \\ 0 & 0 & c\cdot\sin(\beta)\cdot\sin(\alpha^*) \end{pmatrix}, \tag{2.68}$$

where a, b and c are the lattice vector lengths, α, β and γ the lattice angles. The superscript * denotes the reciprocal lattice angles, which are related to the real lattice angles through the relation,

$$\cos(\alpha^*) = \frac{\cos(\beta)\cos(\gamma) - \cos(\alpha)}{\sin(\beta)\sin(\gamma)}. \tag{2.69}$$

The total derivatives of the QM/MM energy (Eq. **??**) with respect to a lattice parameter a is given by $d^aE = d^aE_{\mathrm{QM}} + d^aE_{\mathrm{MM}} + d^aE_{int}$. The total derivative concerning lattice parameters can be written as the

$$d^aE = \partial^aE + \sum_{p}^{\mathrm{N}}(\partial^pE)\cdot(\partial^a\boldsymbol{hu}_p). \tag{2.70}$$

The first term vanishes for interactions accounted for only in the original cell, namely, the E_{QM} and classical bonded terms in E_{MM}. The second term depends on the derivative of the total energy with respect to the QM or MM coordinates and the derivatives of the atom Cartesian coordinates.

The partial derivative of the QM/MM interaction energy can be written as,

$$\partial^aE_{int} = \sum_{A=1}^{N_{\mathrm{QM}}} q_A\left(\Phi_A^{MM,a} + \frac{1}{2}\Phi_A^{QM,a}\right) \tag{2.71}$$

The only term within Φ_A^{QM} that has non-zero derivatives with respect to the lattice parameters is the long-range potential in the reciprocal space (second term in Eq. 2.62), containing an explicit dependence on the volume of the simulation cell. Considering a cubic box, the derivatives with respect to cell length are written as

$$\Phi_A^{QM,a} = -\frac{3a^2}{\pi V^2} \sum_{\mathbf{m}\neq 0} \frac{e^{-\frac{\pi^2\mathbf{m}^2}{\beta^2}}}{\mathbf{m}^2} \mathrm{Re}\left[e^{-2\pi i \mathbf{m}\cdot\mathbf{r}_A} S_{\mathrm{QM}}(\mathbf{m})\right] \tag{2.72}$$

while the derivatives with respect to cell angles are equal to zero, as the volume in the cubic cell is expressed as $V = a^3$.

2.2.6.1 Free energy from QM/MM

The isomerization of peptidyl bonds in proline is a fundamental step of the protein folding process which often coincides with the rate-limiting step of the process,[107, 108] catalyzed by prolyl cis-trans isomerase (PPIase) enzymes.[109, 110] Considering the numerous experimental and computational studies available on the isomerization of proline-containing peptides,[111–117] the cis-trans isomerization reaction involving proline (Ace-Pro-NHMe) and a proline-containing peptide (succinyl-Ala-Ala-Pro-Phe-p-nitroanilide) were chosen in a previous study as a benchmark for our PBC-adapted QM/MM MD methodology.[0] The aforementioned systems are employed again in the current study as a benchmark of the proposed PBC-adapted DFTB/MM method and of DFTB parameters.

In Fig. 2.14 we reported the trans-to-cis free energy profiles in proline computed at the DFTB2-MIO (depicted in light blue), DFTB2-OB2 (depicted in green), and DFTB3-3OB (depicted in red) levels of theory. For the sake of comparison, we reproduced also the profiles computed at the MM level of theory, using a modified set of Amber99sb parameters reported in the literature,[118–120] where the heights of the barrier associated with the peptidyl bond torsion were adjusted to match the experimental data (reported in dark blue), and at the B3LYP/6-31G* level of theory (reported in violet), which underestimates the height of the barrier, probably due to the self-interaction error.[90]. To compare the profiles, the zero has been arbitrarily set to the free energy value of the trans isomer.

Experimentally, the free energy for the trans-cis isomerization barrier is 20.40 kcal·mol^{-1}, and a cis/trans $\Delta\Delta G$ is 0.57 kcal·mol^{-1}.[111] While DFTB2-MIO/MM free energy profile recovers correctly the position of the transition state and the relative energies of the cis and trans isomers ($\Delta\Delta G$ = 0.05 kcal·mol^{-1}), it underestimates the height of the barrier with a $\Delta\Delta G^{\ddagger}$ of 3.43 kcal·mol^{-1}. On the one hand, the DFTB2-OB2 profile reproduces correctly the relative energies of the cis and trans isomers although it slightly underestimates the cis/trans energy ($\Delta\Delta G$ = 0.32 kcal·mol^{-1}). In that case, the position of the transition state is correctly described, and the height of the trans-to-cis barrier is correctly reproduced albeit overestimated, with a $\Delta\Delta G^{\ddagger}$ of 1.49 kcal·mol^{-1}. Similar results have been obtained for the DFTB3-3OB profile, where the height of the barrier is overestimated with a $\Delta\Delta G^{\ddagger}$ of 1.51 kcal·mol^{-1}. However, contrarily to the two profiles computed at the DFTB2 level, the DFTB3 profile wrongly reproduces the relative energies of the cis and trans isomers, with the cis conformation which is predicted to be the more stable one ($\Delta\Delta G$ = 1.64 kcal·mol^{-1}). Based on these benchmarks, we decided to use DFTB2 in combination with OB2 parameters set as the default options for the other studied reactions.

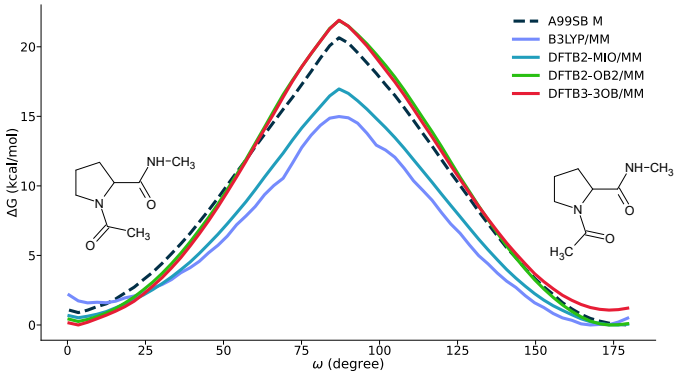

Figure 2.14: Isomerization free energy profile for proline, showing the profile obtained applying the new DFTB/MM PBC-adapted model described in this article using DFTB2 with two different sets of parameters (MIO in light blue, and OB2 in green) and DFTB3 with 3OB parameters (in red). Profiles obtained at *ab initio* B3LYP/MM level (reported in violet) and pure MM level using a modified version of Amber99sb force field (depicted in dark blue), are reported as well. The Amber99sb and B3LYP results have been adapted from literature.[90]

3 Research proposal

Vibrational energy redistribution in photoactive proteins is usually mediated by an initial fast out-of-equilibrium process.[121] The advent of X-ray free electron lasers, have made possible to observe such processes with a time resolution of the order of few femtoseconds, with experimental techniques such as time-resolved serial femtosecond crystallography and time-resolved X-ray scattering.[122, 123] In the specific case of myoglobin, for example, we demonstrated that few femtosecond coherent oscillations spanning multiple residues within the cavity enables efficient energy transfer across the protein.[14, 19] Energy redistribution in myoglobin flows in specific pathways, directing energy from the active side to the F and E alpha helices, and subsequently to D and C alpha helices in a few picoseconds, which allows the gas to escape.[124] This targeted redistribution is essential for the maintaining biological activity and is closely linked to a protein's evolutionary adaptability.[125]

My research proposal aims at developing a general strategy to simulate energy flow in photoactive proteins. This requires multi-scale modelling strategies to describe: (i) the shortest-time non-adiabatic dynamics, (ii) the middle time range, in which out-of-equilibrium energy redistribution happens in the ground state, and (iii) the long time at which a new equilibrium is reached. For non-adiabatic dynamics, *nuclear quantum effects* are fundamental for describing strong coupling between electrons and nuclear motions. Still, for the middle and longer times, nuclear quantum effects can become important, especially electron-coupled proton transfer reactions, or out-of-equilibrium energy redistribution in condensed phase.[126] Indeed, nuclear quantum phenomena such as tunneling and especially zero-point energy (ZPE) are central to the redistribution of energy in proteins.[127] The ZPE significantly influences vibrational modes and their coupling within the protein matrix. In classical mechanics, ZPE leakage (artificial transfer from localized high-frequency modes to lower-frequency modes) can affect the flow and dissipation of energy throughout the protein.

In the previous chapter, I showed the developments we have performed up to the computation of free energies in NVE, NVT and NPT ensembles using an efficient QM/MM approach in periodic boundary conditions, using *ab initio* and semi-empirical methods. These development will be central to describe condensed-phase energy redistribution in photoactive proteins including nuclear quantum effects. Nuclear effects will be implemented in an incremental way. First, I will only treat quantum hydrogen atoms in proton-transfer electron coupled reaction, by extending the ESPF QM/MM description with the nuclear electron orbital method. Second, I will combine QM/MM PBC with path integral molecular dynamics (PIMD), which will generalizes the description of quantum effects for all atoms in the system. This will require several parallel developments, that will allow in a single framework to describe the photoexcitation from the initial photon absorption to the dissipation of energy at longer times.

This project faces a technical problem, which is the computational cost of treating the quantum effects of nuclei, both for ground and excited states. Computational cost limits molecular size, simulation timescale and sampling. In the ANR MAPPLE project, we have been focusing on bringing polarizable embedding QM/MM (QM/MMPol) molecular dynamics to the nanosecond timescale. Despite the efforts of defining a new QM/MMPol interaction that scales linearly with the number of MM atoms,[128] most of the computational cost comes from the *ab initio* QM calculations. Several strategies in the literature have been focusing on reducing the cost of two-electron integrals.[129–134] Still, the computational cost of energy, gradients, and non-adiabatic couplings makes the computation of long-time energy dissipation with the sampling that is required. In the case of QM/MM PBC, we demonstrated that semi-empirical DFTB/MM was accurately reproducing free energy profiles of molecules in solution. For the excited states, I will explore the accuracy of a tight-binding version of mixed-reference spin-flip TDDFT.

3.1 Proton-coupled electron transfer in condensed phase

Proton-coupled electron transfer (PCET) reactions are a fundamental kind of reaction for catalysis and energy transformation, both in synthetic and biological systems. For example, photoinduced PCET has been shown to activate C-H bonds by hydrogen atom transfer (HAT).[135] In a redox process, coupling the movement of a proton with that of an electron can provide an energetic advantage over electron transfer alone by reducing both the activation barrier and the driving force of the reaction. Simulation of such reactions requires (at least) a quantum treatment of the proton that is coupled to the electron motion. The inclusion of tunneling effects and zero-point energy has a dramatic effect on pKas, with the nuclear quantum effects downshift 4.5 pKa units in liquid water.[136]

A simple approach to include the quantum effects on protons is the nuclear-electron orbital (NEO) approach,[137] in which the NEO wavefunction can be written with the *Ansatz* $\Psi_{\text{NEO}} = \Phi^e \Phi^p$. In that case, both electrons and quantum nuclei wavefunctions are expressed in a Gaussian atomic basis set, leading to two coupled Fock operators for electron and proton,

$$\mathbf{F}^e \mathbf{C}^e = \epsilon^e \mathbf{S}^e \mathbf{C}^e \tag{3.1}$$

$$\mathbf{F}^p \mathbf{C}^p = \epsilon^p \mathbf{S}^p \mathbf{C}^p \tag{3.2}$$

Incorporating this approach to our developed ESPF QM/MM scheme in periodic boundary conditions is simple. Indeed, the NEO Hamiltonian can be complemented with the QM/MM interaction in a usual way $\hat{H} = \hat{H}^{\text{NEO}} + \hat{H}^{QM/MM}$.[138, 139] In this case, the QM/MM Hamiltonian interacts both with classical nuclei, quantum nuclei and the electrons. For non-periodic boundary conditions and simple electrostatics,

$$\hat{H}^{\text{QM/MM}} = \sum_{i=1}^{N_{\text{MM}}} q_i \left(\sum_{\alpha=1}^{N_e} \frac{-1}{|\mathbf{r}_\alpha^e - \mathbf{r}_i|} + \sum_{a=1}^{N_p} \frac{1}{|\mathbf{r}_a^p - \mathbf{r}_i|} + \sum_{A=1}^{N_c} \frac{Z_A}{|\mathbf{R}_A - \mathbf{r}_i|} \right), \tag{3.3}$$

in which N_{MM}, N_{QM}, N_p and N_c are respectively the number of MM atoms, the number of QM atoms, the number of quantum nuclear centers and the number of classical centers. We can take advantage of the ESPF approach to define a charge operator for electrons and quantum protons. The ESPF approach is applied with no modifications, in which two grids, one for electron electrostatic integrals and one for quantum nuclei integrals will be constructed and fitted in the usual way,

$$\hat{Q} = \left(\mathbf{T}_e^\dagger \mathbf{T}_e \right) \mathbf{T}_e^\dagger \hat{V}^e \tag{3.4}$$

$$\hat{Z} = \left(\mathbf{T}_p^\dagger \mathbf{T}_p \right) \mathbf{T}_p^\dagger \hat{V}^p, \tag{3.5}$$

leading to the simplified NEO ESPF QM/MM Hamiltonian,

$$\hat{H}^{\text{QM/MM}} = \sum_c^{N_c} \left(Z_c - \hat{Q}_c \right) \phi_c + \sum_p^{N_p} \left(\hat{Z}_p - \hat{Q}_p \right) \phi_p, \tag{3.6}$$

with the usual definition of the MM electrostatic potential (which depends on the treatment of electrostatics). The first term is equivalent to the ESPF interaction Hamiltonian. The second term steams from the quantum treatment of protons. As I showed in the applications, this will simplify the computation of energy and gradients, in addition to simplify the definition of a NEO QM/MM approach in periodic boundary conditions and the extension to polarizable forcefields.

The NEO ESPF QM/MM approach will be applied to study several types of reactions. To show the usefulness of this approach, several applications with incremental complexity will be developed. First, the computation of pKas and redox potentials of nucleobases in explicit water solvation,[140] by developing a thermodynamic integration approach. Second, the computation of excited state pKas of photoswitches in the excited state.[141] Finally, this approach along with molecular dynamics will be used to study the light-induced PCET reaction of a dye, which induces the appearance of

fluorescence.[142]

3.2 Energy redistribution in condensed phase

Energy distribution in condensed phase, especially when it is photoinitiated, is still lacking from solid simulation protocols that can model the strong electron-nuclear coupling effects in short time, and the coupling with low-frequency modes in longer timescales.[143] In the past, I have attempted to apply the instantaneous normal mode approach by developing efficient electrostatic embedding QM/MM Hessian calculations and localization of normal modes.[84, 85, 93] This approach corresponds to a posteriori analysis of non-equilibrium molecular dynamics simulations. However, it is too costly to be applied to large molecular systems.

Treating both the long-time energy distribution and the short-time electron-nuclear coupling for non-adiabatic dynamics requires that atoms are treated quantum mechanically. The NEO QM/MM approach is one practical possibility, but it only introduces QM effects on selected nuclei in the QM region, whereas most of the system is still treated classically. There have been simple solutions to add quantum effects by employing quantum thermal baths along with Langevin dynamics. This is indeed a practical solution, but suffers still from the well-known zero-point energy leakage problem that affects classical mechanics and prevents, for example, the study of energy redistribution.

In this project, I will explore new models for describing photoinduced electron distribution treating all nuclear quantum mechanically by means of path integral molecular dynamics (PIMD). The main problem of PIMD is to efficiently span the space of all possible pathways. A simple and approximate way to implement the PIMD approach is the so-called ring-polymer molecular dynamics (RPMD) theory. The RPMD approach it is based on a discretization of the canonical partition function,

$$Z = \mathrm{Tr}\left[e^{-\beta\hat{H}}\right] = \lim_{n\to\infty}\left(\frac{n}{2\pi\hbar}\right)^n \int d\mathbf{x}\, d\mathbf{p}\, e^{-\beta_n \hat{H}_n^{RP}(\mathbf{x},\mathbf{p})}, \tag{3.7}$$

in which β is the reduced temperature, and H^{RP} is the ring-polymer Hamiltonian,

$$H_n^{RP}(\mathbf{x},\mathbf{p}) = \sum_{\alpha}^{n} \frac{p_\alpha^2}{2m} + \frac{1}{2} m\omega_n^2 \left(x_\alpha - x_{\alpha+1}\right)^2 + V(x_\alpha), \tag{3.8}$$

where $\beta_n = \beta/n$ and $\omega_n = (\beta_n\hbar)^{-1}$. In this Hamiltonian, the kinetic and potential energies are the usual ones in classical dynamics. However, each particle has several simultaneous representations (called beads) that can exchange energy due to the bead spring terms. Performing thus approximate quantum dynamics with the RPMD Hamiltonian, one recovers quantum effects in classical trajectories integrating the equation of motion defined as

$$\dot{x}_\alpha = \frac{\partial H^{RP}(\mathbf{x},\mathbf{p})}{\partial p_\alpha} = \frac{p_\alpha}{m} \tag{3.9}$$

$$\dot{p}_\alpha = \frac{\partial H^{RP}(\mathbf{x},\mathbf{p})}{\partial x_\alpha} = m\omega_n^2(x_{\alpha+1} + x_{\alpha-1} - 2x_\alpha) - \frac{\partial V(x_\alpha)}{\partial x_\alpha}. \tag{3.10}$$

This approach allows to define more rigorously a QM/MM molecular dynamics simulation. Indeed, we can partition the total QM/MM Hamiltonian in the following way,

$$\hat{H}^{QM/MM}(\mathbf{x},\mathbf{p}) = \hat{H}^{MM}(\mathbf{p}_{MM},\mathbf{x}_{MM}) + \hat{H}^{QM}(\mathbf{p}_{QM},\mathbf{x}_{QM}) + \hat{V}_{QM/MM}(\mathbf{x}_{QM},\mathbf{x}_{MM}), \tag{3.11}$$

where

$$H^{QM}(\mathbf{p}_{QM},\mathbf{x}_{QM}) = \hat{T}^{QM}(\mathbf{p}_{QM}) + \hat{V}_{QM}(\mathbf{x}_{QM}) \tag{3.12}$$

$$H^{MM}(\mathbf{p}_{MM},\mathbf{x}_{MM}) = \hat{T}^{MM}(\mathbf{p}_{MM}) + \hat{V}_{MM}(\mathbf{x}_{MM}). \tag{3.13}$$

Taking now the definition of the Boltzmann operator,

$$Z = Tr\left[e^{-\beta \hat{H}^{QM/MM}}\right] \tag{3.14}$$

we can approximately write

$$Z \approx \mathrm{Tr}\left[\prod_{i=1}^{N} e^{-\frac{\beta_N}{2}\left(\hat{V}_{QM}+\hat{V}_{MM}+\hat{V}_{QM/MM}\right)} e^{-\beta_N\left(\hat{T}_{MM}+\hat{T}_{QM}\right)} e^{-\frac{\beta_N}{2}\left(\hat{V}_{QM}+\hat{V}_{MM}+\hat{V}_{QM/MM}\right)}\right]. \tag{3.15}$$

The trace here traces on QM and MM nuclear positions as well as electronic degrees of freedom. If one performs the nuclear trace $|\mathbf{x}_{MM}\rangle$ and $|\mathbf{x}_{QM}\rangle$ positions and a single electronic state $|i\langle$, one obtains

$$Z \approx \frac{1}{(2\pi\hbar)^n}\int d\mathbf{p}^{MM}\int d\mathbf{p}^{QM}\int d\mathbf{x}^{MM}\int d\mathbf{x}^{QM} e^{\left(-\beta H_n^{RP,QM/MM}(\mathbf{x}_{QM},\mathbf{x}_{MM},\mathbf{p}_{QM},\mathbf{p}_{MM})\right)}, \tag{3.16}$$

in which the QM/MM ring-polymer Hamiltonian has the usual form as in Eq. 3.8. In this project, I will first test the validity of the ESPF approach for RPMD QM/MM in electrostatic and polarizable embedding. For each set of bead coordinates, an electrostatic potential is generated, which generates in turn a set of charges. The effect of this approximation for computing the QM/MM interaction will assessed, especially focusing on the average charge at each QM center, the average electrostatic interaction between QM/MM and the stability of NVE dynamics. The correct implementation of this approach, will allow to reconstruct free energy profiles, especially when proton transfer is involved. We will re-examine the pterine and S_N2 reactions at the DFTB/MM level, comparing the results of PIMD with purely classical dynamics.

The main interest for using RPMD is however the use of non-adiabatic dynamics for excited states.[144] Indeed, the trace over electronic states in 3.15 can be done over several electronic (adiabatic) states and nuclei waveunctions. For each bead, a stochastic hop can occur renormalized by an overlap term between the different adiabatics added to the RP Hamiltonian. This overlap term can be related to the nuclear decoherence. If adjacent beads are on the same adiabatic surface, they only interact through the ring-polymer potential, whereas if adjacent beads are on different diabatic surfaces, the contribution to the partition function (and to the averages) decreases. Implementing PIMD coupled to surface hopping in the adiabatic picture is simple. As a test case, I have performed a simulation of a trajectory on which all beads start on the same initial surface of a model for a conical intersection, in which the potentials are

$$V_1(X,Y) = \frac{1}{2}k\left((X-X_0)^2+(Y-Y_0)^2\right) \tag{3.17}$$

$$V_2(X,Y) = \frac{1}{2}k\left((X+X_0)^2+(Y+Y_0)^2\right) \tag{3.18}$$

$$V_{12}(X,Y) = \alpha e^{-(X-X_0)^2-(Y+Y_0)^2} \tag{3.19}$$

in which the parameters have been chosen as $X_0 = 1$, $Y_0 = 0$, $k = 1.0$, and $\alpha = 0.1$. For the PIMD, 15 beads have been propagated using Verlet algorithm, with $\beta = 1.0$ for 1 ps, starting from $X_0 = Y_0 = -2$ and initial random velocities for each bead. The results are shown in Fig. 3.1 for a single trajectory, in which all beads start in the first potential energy surface. Each bead hops independently, following a compact path around a well-defined centroid shown in black. Statistics of all possible combinations of beads in all possible adiabatic states, when the number of beads tend to infinity, one should be able to reconstruct the exact quantum probability of the nuclear wavepacket. In this second part of the project, I will explore strategies to implement and especially accelerate ring-polymer non-adiabatic dynamics in the excited state.

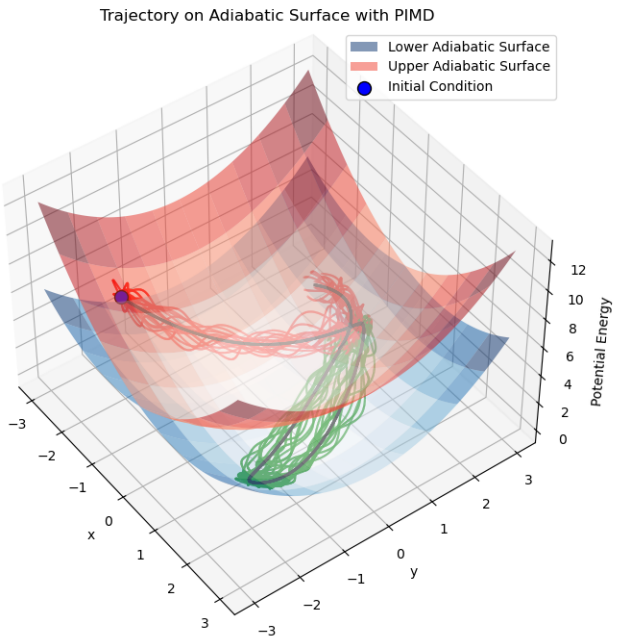

Figure 3.1: Non-adiabatic path-integral molecular dynamics simulation on a model conical intersection defined in Eq. 3.17
for 15 beads. The potential energy surface is shown for both first and second adiabatic states. The initial condition for all beads is shown as a blue circle. The path of the centroid is shown in black, and the independent bead path in color depending on the surface in which it is found.

Merging the QM/MM in periodic boundary conditions and non-adiabatic path integral molecular dynamics will provide a computational framework to study energy dissipation not only of photoactive proteins, but also electron-transfer proteins. The final part of this project will be to provide an analysis of the energy flow in protein from dynamic trajectories. A way to do it is to compute the energy flow from an atomic decomposition of thermodynamic work,

$$\Delta W_i(t_1,t_2) = \int_{\mathbf{q}_i(t_1)}^{\mathbf{q}_i(t_2)} \mathrm{F}_i \cdot \mathrm{v}_i \, dt\,, \tag{3.20}$$

which describes the change in potential energy for atom i along the trajectory from t_1 to t_2.[145] A similar equation can be derived for the kinetic energy flow per atom.[146] These quantities allow to make a map of the energy flow in protein. I will reformulate these quantities for QM/MM, in order to map the energy flow due to the photon energy.

As a test case, I will study the fluorescence loss of GFP chromophore in water,[147] which has been shown by time-resolved Raman spectroscopy to reach a twisted intramolecular charge transfer state in 3 ps and a loss of the photon energy in the solvent in 250 ps. The described simulations will provide the first picture of the energy dissipation in water, with a full account of long-range electrostatics and quantum effects both in the ground and excited states.

3.3 Semi-empirical methods for excited states

Spin-flip linear-response time-dependent density-functional theory (SF-TDDFT) has been proposed as a cost-effective way of capturing multi-configurational correlation effects in the ground- and excited

states.[148, 149] In the usual formulation, the reference density is obtained from a Kohn-Sham (KS) wavefunction for the lowest open-shell triplet ($M_s = +1$), from which response functions are expanded in the basis of spin-flip excitations ($\Delta M_s = \pm 1$). Despite some successful examples for describing ground- and excited-state conical intersections,[150] the spin contamination of electronic states described by configurations outside the open-shell orbitals limited its applications. This problem has been recently solved by formulating a spin-flip approach on a mixed-reference triplet of $M_s = \pm 1$, a method dubbed mixed-reference spin-flip TDDFT (MRSF-TDDFT). It nearly eliminates the spin contamination of SF-TDDFT by expanding the electron configuration space while still maintaining a favorable computational cost.[101, 151–167]

In order to reduce the cost of the QM calculations, I will derive, implement and test the use of density functional based tight binding version of SF-TDDFTB and MRSF-TDDFTB. I have performed a preliminary implementation of SF-TDDFTB, showing surprisingly accurate results with respect to all-electron MRSF-TDDFT.[168] As a test case, I tested the photoisomerisation connecting all-trans retinal protonated Schiff base (rPSB) to 11-cis rPSB is the main reaction in visual rhodopsin proteins. The main isomerisation reaction is initiated in the S_1 excited state, for which a conical instersection S_0/S_1 at approximately 90° twisting. In Figure 3.2, the potential energy surface interpolating the 11-cis, the conical intersection (CX) and the all-trans rPSB computed at the SF-TDDFTB is shown. A comparison with all-electron MRSF-TDDFT is added as reference on the same interpolated geometries. Overall, the topology of the surfaces at the MRSF-TDDFT and SF-TDDFTB level are very similar. The ground state average difference between MRSF-TDDFT and SF-TDDFT is 2.04 kcal/mol, with a standard deviation of 1.90 kcal/mol. For the excited state it is 5.23 kcal/mol with a standard deviation of 1.53 kcal/mol. The main changes come at the the CX. The CX is computed at the SF-TDDFTB level and features a 99° twist between the two moieties. At this geometry, MRSF-TDDFT has an energy gap of 6.03 kcal/mol. This is indicating that the MRSF-TDDFT CX is not exactly at the same geometry as SF-TDDFTB. The 11-cis conformer is 4.17 kcal/mol less stable than the all-trans conformer in SF-TDDFTB, in good agreement with the 5.42 kcal/mol of MRSF-TDDFT.In the excited state, the all-trans to CX SF-TDDFTB features a barrier of 9.03 kcal/mol, in comparison with the 10.39 kcal/mol in MRSF. For the 11-cis to CX the barrier is slightly larger, with 14.36 kcal/mol in SF-TDDFTB compared to 10.39 kcal/mol in MRSF-TDDFT.

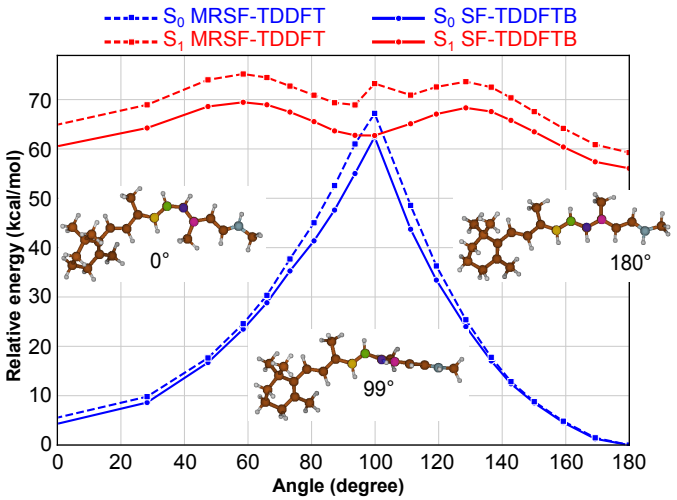

Figure 3.2: Comparison of SF-TDDFTB (solid line) and MRSF-TDDFT (dashed line) for the ground- (blue lines) and first excited (red lines) state potential energy surfaces along an interpolation coordinate for a protonated Schiff base model. The structures correspond to the interpolated coordinates. The dihedral angle (yellow, green, blue and magenta carbon atoms) is specified as an offset on each structure.

Alternatively, machine learning potentials become especially suitable for summarizing costly electronic structure calculations on a model machine learning potential. This kind of potentials can be useful for MCTDH, accelerating the development of model Hamiltonians for studying reactivity of gas-phase molecules, but also for coupling these to an electrostatic environment via a QM/MM coupling. In the former case, only the energies are required along selected nuclear distortions to produce an accurate potential energy surface. This can nowadays be routinely done. I show in Fig. 3.3 a trained ML potential that diabatizes a model for a conical intersection represented as displaced harmonic oscillators. The neural network takes 2 inputs (x and y coordinates), and output three values (diabatic energy of state 1 and 2 and the coupling). A single hidden layer is used with 64 neurons and ReLU filtering to add non-locality. A training set of 1000 random points have been generated to train the neural network.

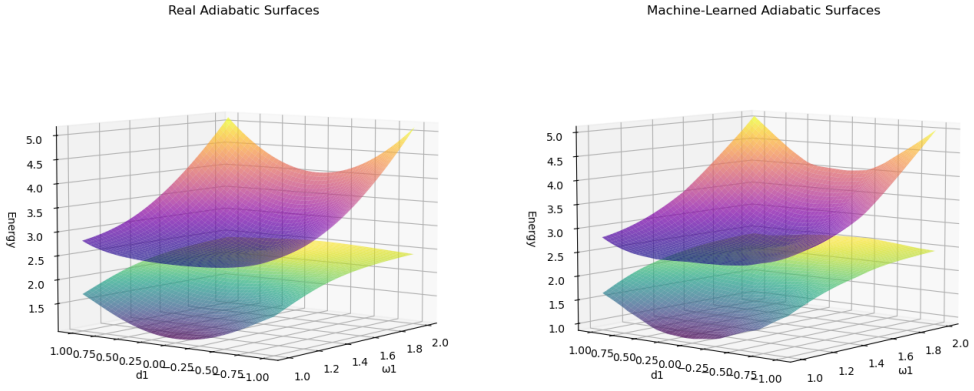

Figure 3.3: Neural network fitting of a diabatic model Hamiltonian from an adiabatic surface. The reference surface (left) is compared to the fitted adiabatic surface (right).

Bibliography

[1] J. W. Verhoeven. “Glossary of terms used in photochemistry (IUPAC Recommendations 1996)”. In: *Pure and Applied Chemistry* 68.12 (Jan. 1996), pp. 2223–2286. DOI: 10.1351/pac199668122223 (cit. on p. 16).

[2] Christel M. Marian. “Spin–orbit coupling and intersystem crossing in molecules”. In: *WIREs Computational Molecular Science* 2 (2012), pp. 187–203. DOI: 10.1002/wcms.83 (cit. on p. 16).

[3] Kenneth G. Dyall. “Interfacing relativistic and nonrelativistic methods. I. Normalized elimination of the small component in the modified Dirac equation”. In: *The Journal of Chemical Physics* 106 (1997), pp. 9618–9626. DOI: 10.1063/1.473860 (cit. on p. 16).

[4] Thomas J. Penfold, Etienne Gindensperger, Chantal Daniel, and Christel M. Marian. “Spin-Vibronic Mechanism for Intersystem Crossing”. In: *Chemical Reviews* 118.15 (2018), pp. 6975–7025. DOI: 10.1021/acs.chemrev.7b00617 (cit. on pp. 16, 22).

[5] Bryan R. Henry and Willem Siebrand. “Spin–Orbit Coupling in Aromatic Hydrocarbons. Analysis of Nonradiative Transitions between Singlet and Triplet States in Benzene and Naphthalene”. In: *The Journal of Chemical Physics* 54 (1971), pp. 1072–1085. DOI: 10.1063/1.1674940 (cit. on p. 16).

[6] S. E. Braslavsky. “Glossary of terms used in photochemistry, 3rd edition (IUPAC Recommendations 2006)”. In: *Pure and Applied Chemistry* 79.3 (2007), pp. 293–465. ISSN: 0033-4545. DOI: 10.1351/pac200779030293 (cit. on p. 16).

[7] Vidisha Rai-Constapel, Mihajlo Etinski, and Christel M. Marian. “Photophysics of Xanthone: A Quantum Chemical Perusal”. In: *J. Phys. Chem. A* 117 (2013), pp. 3935–3944. DOI: 10.1021/jp401755j (cit. on pp. 16, 21).

[8] Jörg Tatchen, Natalie Gilka, and Christel M. Marian. “Intersystem crossing driven by vibronic spin–orbit coupling: a case study on psoralen”. In: *Phys. Chem. Chem. Phys.* 9 (38 2007), pp. 5209–5221. DOI: 10.1039/B706410A (cit. on p. 17).

[9] Mihajlo Etinski and Christel M. Marian. “Overruling the energy gap law: fast triplet formation in 6-azauracil”. In: *Phys. Chem. Chem. Phys.* 12 (48 2010), pp. 15665–15671. DOI: 10.1039/C0CP00106F (cit. on p. 17).

[10] Angela Rodriguez-Serrano, Vidisha Rai-Constapel, Martha C. Daza, Markus Doerr, and Christel M. Marian. "Internal heavy atom effects in phenothiazinium dyes: enhancement of intersystem crossing via vibronic spin–orbit coupling". In: *Phys. Chem. Chem. Phys.* 17 (17 2015), pp. 11350–11358. DOI: 10.1039/C5CP00194C (cit. on p. 17).

[11] Mihajlo Etinski and Christel M. Marian. "A theoretical study of low-lying singlet and triplet excited states of quinazoline, quinoxaline and phthalazine: insight into triplet formation". In: *Phys. Chem. Chem. Phys.* 19 (2017), pp. 13828–13837. DOI: 10.1039/C7CP02022H (cit. on p. 17).

[12] Angela Rodriguez-Serrano, Fabian Dinkelbach, and Christel M. Marian. "Intersystem crossing processes in the 2CzPN emitter: a DFT/MRCI study including vibrational spin–orbit interactions". In: *Phys. Chem. Chem. Phys.* 23 (5 2021), pp. 3668–3678. DOI: 10.1039/D0CP06011A (cit. on p. 17).

[13] Miquel Huix-Rotllant, Irene Burghardt, and Nicolas Ferré. "Population of triplet states in acetophenone: A quantum dynamics perspective". In: *Comptes Rendus Chimie* 19.1-2 (2016), pp. 50–56. DOI: 10.1016/j.crci.2015.10.002 (cit. on p. 17).

[14] Konstantin Falahati, Hiroyuki Tamura, Irene Burghardt, and Miquel Huix-Rotllant. "Ultrafast carbon monoxide photolysis and heme spin-crossover in myoglobin via nonadiabatic quantum dynamics". In: *Nature Communications* 9.1 (2018). DOI: 10.1038/s41467-018-06615-1 (cit. on pp. 17, 48).

[15] Marc Alías-Rodríguez, Coen de Graaf, and Miquel Huix-Rotllant. "Ultrafast Intersystem Crossing in Xanthone from Wavepacket Dynamics". In: *Journal of the American Chemical Society* 143.51 (2021), pp. 21474–21477. DOI: 10.1021/jacs.1c07039 (cit. on pp. 17, 19).

[16] Marc Alías-Rodríguez, Miquel Huix-Rotllant, and Coen de Graaf. "Quantum dynamics simulations of the thermal and light-induced high-spin to low-spin relaxation in $Fe(bpy)_3$ and $Fe(mtz)_6$". In: *Faraday Discussions* (2022). DOI: 10.1039/d2fd00027j (cit. on pp. 17, 23).

[17] Marc Alías-Rodríguez, Swarnendu Bhattacharyya, and Miquel Huix-Rotllant. "Ultrafast Spin Crossover Photochemical Mechanism in $[Fe^{II}(2,2\prime\text{-bipyridine})_3]^{2+}$ Revealed by Quantum Dynamics". In: *The Journal of Physical Chemistry Letters* (2023), pp. 8571–8576. DOI: 10.1021/acs.jpclett.3c02201 (cit. on pp. 17, 21).

[18] Marc Alías-Rodríguez and Miquel Huix-Rotllant. "Control of the iron-tris(2,2-bipyridine) light-induced excited-state trapping via external electromagnetic fields". In: *ChemPhysChem* (2024). DOI: 10.1002/cphc.202400471 (cit. on p. 17).

[19] Thomas R.M. Barends, Swarnendu Bhattacharyya, Alexander Gorel, Giorgio Schiro, Camila Bacellar, et al. "Influence of pump laser fluence on ultrafast structural changes in myoglobin". In: *Nature* 626 (2024), pp. 905–911. DOI: 10.1038/s41586-024-07032-9 (cit. on pp. 17, 32, 48).

[20] G. A. Worth, H.-D. Meyer, H. Köppel, L. S. Cederbaum, and I. Burghardt. "Using the MCTDH wavepacket propagation method to describe multimode non-adiabatic dynamics". In: *International Reviews in Physical Chemistry* 27.3 (2008), pp. 569–606. DOI: 10.1080/01442350802137656 (cit. on p. 17).

[21] Bernd A. Heßand Christel M. Marian, Ulf Wahlgren, and Odd Gropen. "A mean-field spin-orbit method applicable to correlated wavefunctions". In: *Chemical Physics Letters* 251.5 (1996), pp. 365–371. DOI: 10.1016/0009-2614(96)00119-4 (cit. on p. 18).

[22] Masaaki Baba, Toshihiro Kamei, Masahide Kiritani, Seigo Yamauchi, and Noboru Hirota. "A phosphorescence study of jet-cooled xanthone". In: *Chem. Phys. Lett.* 185 (1991), pp. 354–358. DOI: 10.1016/S0009-2614(91)85074-7 (cit. on pp. 20, 21).

[23] Yukio Ohshima, Teruyuki Fujii, Takanori Fujita, Daisuke Inaba, and Masaaki Baba. "$S_1\ ^1A_2(n\pi^*)$ and $S_2\ ^1A_1(\pi\pi^*)$ States of Jet-Cooled Xanthone". In: *J. Phys. Chem. A* 107 (2003), pp. 8851–8855. DOI: 10.1021/jp030260d (cit. on p. 21).

[24] H. Satzger, B. Schmidt, C. Root, W. Zinth, B. Fierz, et al. "Ultrafast Quenching of the Xanthone Triplet by Energy Transfer: New Insight into the Intersystem Crossing Kinetics". In: *J. Phys. Chem. A* 108 (2004), pp. 10072–10079. DOI: 10.1021/jp047583+ (cit. on p. 21).

[25] B. Heinz, B. Schmidt, C. Root, H. Satzger, F. Milota, et al. "On the unusual fluorescence properties of xanthone in water". In: *Phys. Chem. Chem. Phys.* 8 (29 2006), pp. 3432–3439. DOI: 10.1039/B603560D (cit. on p. 21).

[26] Ionela Rusu, Ioan Cozmin Manolache-Rusu, Andrei Diaconu, Oleg Palamarciuc, Il'ya A. Gural'skiy, et al. "Pressure Gradient Effect on Spin-crossover Materials: Experiment Vs Theory". In: *J. Appl. Phys.* 129 (2021), p. 064501. DOI: 10.1063/5.0042582 (cit. on p. 22).

[27] Volodymyr M. Hiiuk, Sergiu Shova, Aurelian Rotaru, Vadim Ksenofontov, Igor O. Fritsky, et al. "Room Temperature Hysteretic Spin Crossover in a New Cyanoheterometallic Framework". In: *Chem. Commun.* 55 (2019), pp. 3359–3362. DOI: 10.1039/C8CC10260K (cit. on p. 22).

[28] Wojciech Gawelda, Andrea Cannizzo, Van-Thai Pham, Frank van Mourik, Christian Bressler, et al. "Ultrafast Nonadiabatic Dynamics of $[Fe^{II}(bpy)_3]^{2+}$ in Solution". In: *J. Am. Chem. Soc.* 129.26 (2007), pp. 8199–8206. DOI: 10.1021/ja070454x (cit. on pp. 22, 23, 26).

[29] Ch. Bressler, C. Milne, V.-T. Pham, A. ElNahhas, R. M. van der Veen, et al. "Femtosecond XANES Study of the Light-Induced Spin Crossover Dynamics in an Iron(II) Complex". In: *Science* 323.5913 (2009), pp. 489–492. DOI: 10.1126/science.1165733 (cit. on pp. 22, 23, 26).

[30] A. Cannizzo, C.J. Milne, C. Consani, W. Gawelda, Ch. Bressler, et al. "Light-induced Spin Crossover in Fe(II)-based Complexes: The Full Photocycle Unraveled by Ultrafast Optical and X-ray Spectroscopies". In: *Coord. Chem. Rev.* 254 (2010), pp. 2677–2686. DOI: 10.1016/j.ccr.2009.12.007 (cit. on pp. 22, 23, 26).

[31] Wenkai Zhang, Roberto Alonso-Mori, Uwe Bergmann, Christian Bressler, Matthieu Chollet, et al. "Tracking Excited-state Charge and Spin Dynamics in Iron Coordination Complexes". In: *Nature* 509 (2014), pp. 345–348. DOI: 10.1038/nature13252 (cit. on pp. 22, 23, 26).

[32] G. Aubock and M. Chergui. "Sub–50–fs photoinduced spin crossover in $[Fe(bpy)_3]^{2+}$". In: *Nat. Chem.* 7 (2015), pp. 629–633. DOI: 10.1038/nchem.2305 (cit. on pp. 22–24, 26, 28, 31).

[33] H. T. Lemke, K. S. Kjaer, R. Hartsock, T. B. van Driel, M. Chollet, et al. "Coherent structural trapping through wave packet dispersion during photoinduced spin state switching". In: *Nat. Comm.* 6 (2017), p. 6772. DOI: 10.1038/ncomms15342 (cit. on pp. 22–24, 26, 28, 30).

[34] Guillaume Chastanet, Maciej Lorenc, Roman Bertoni, and Cédric Desplanches. "Light-Induced Spin Crossover – Solution and Solid-state Processes". In: *C. R. Chim.* 21 (2018), pp. 1075–1094. DOI: 10.1016/j.crci.2018.02.011 (cit. on p. 22).

[35] Wenkai Zhang, Kasper S. Kjær, Roberto Alonso-Mori, Uwe Bergmann, Matthieu Chollet, et al. "Manipulating Charge Transfer Excited State Relaxation and Spin Crossover in Iron Coordination Complexes with Ligand Substitution". In: *Chem. Sci.* 8 (2017), pp. 515–523. DOI: 10.1039/C6SC03070J (cit. on pp. 22, 24).

[36] Kasper S. Kjær, Tim B. Van Driel, Tobias C. B. Harlang, Kristjan Kunnus, Elisa Biasin, et al. "Finding Intersections Between Electronic Excited State Potential Energy Surfaces with Simultaneous Ultrafast X-ray Scattering and Spectroscopy". In: *Chem. Sci.* 10 (2019), pp. 5749–5760. DOI: 10.1039/C8SC04023K (cit. on pp. 22, 23, 26).

[37] Malte Oppermann, Francesco Zinna, Jérôme Lacour, and Majed Chergui. "Chiral Control of Spin-Crossover Dynamics in Fe(II) Complexes". In: *Nat. Chem.* 14 (2022), pp. 739–745. DOI: 10.1038/s41557-022-00933-0 (cit. on p. 22).

[38] Coen de Graaf and Carmen Sousa. "Study of the Light-Induced Spin Crossover Process of the $[Fe^{II}(bpy)_3]^{2+}$ Complex". In: *Chem. Eur. J.* 16 (2010), pp. 4550–4556. DOI: 10.1002/chem.200903423 (cit. on pp. 22, 23).

[39] Alex Domingo, Carmen Sousa, and Coen de Graaf. "The Effect of Thermal Motion on the Electron Localization in Metal-to-Ligand Charge Transfer Excitations in $[Fe(bpy)_3]^{2+}$". In: *Dalton Trans.* 43 (2014), pp. 17838–17846. DOI: 10.1039/C4DT02294G (cit. on pp. 22, 23).

[40] C. Sousa, C. de Graaf, A. Rudavskyi, R. Broer, J. Tatchen, et al. "Ultrafast Deactivation Mechanism of the Excited Singlet in the Light-Induced Spin Crossover of $[Fe(2,2'\text{-bipyridine})_3]^{2+}$". In: *Chem. Eur. J.* 19 (2013), pp. 17541–17551. DOI: 10.1002/chem.201302992 (cit. on pp. 22, 28).

[41] Carmen Sousa, Miquel Llunell, Alex Domingo, and Coen de Graaf. "Theoretical Evidence for the Direct ^{3}MLCT-HS Deactivation in the Light-induced Spin Crossover of Fe(II)-polypyridyl Complexes". In: *Phys. Chem. Chem. Phys.* 20 (2018), pp. 2351–2355. DOI: 10.1039/C7CP08098K (cit. on pp. 22, 23).

[42] Lai Chung Liu. "Photoinduced Spin Crossover in Iron(II) Systems". In: Chemistry in Action: Making Molecular Movies with Ultrafast Electron Diffraction and Data Science. Cham, Switzerland: Springer International Publishing, 2020, pp. 105–161. ISBN: 978-3-030-54851-3. DOI: 10.1007/978-3-030-54851-3_5 (cit. on pp. 22, 23).

[43] Mátyás Pápai, Thomas J. Penfold, and Klaus B. Møller. "Effect of tert-Butyl Functionalization on the Photoexcited Decay of a Fe(II)-N-Heterocyclic Carbene Complex". In: *J. Phys. Chem. C* 120 (2016), pp. 17234–17241. DOI: 10.1021/acs.jpcc.6b05023 (cit. on p. 22).

[44] Mátyás Pápai, Gyorgy Vankó, Tamás Rozgonyi, and Thomas J. Penfold. "High-Efficiency Iron Photosensitizer Explained with Quantum Wavepacket Dynamics". In: *J. Phys. Chem. Lett.* 7 (2016), pp. 2009–2014. DOI: 10.1021/acs.jpclett.6b00711 (cit. on p. 22).

[45] Konstantin Falahati, Carsten Hamerla, Miquel Huix-Rotllant, and Irene Burghardt. "Ultrafast photochemistry of free-base porphyrin: a theoretical investigation of B $\rightarrow$ Q internal conversion mediated by dark states". In: *Phys. Chem. Chem. Phys.* 20 (2018), pp. 12483–12492. DOI: 10.1039/C8CP00657A (cit. on pp. 22, 27, 32).

[46] Mátyás Pápai, Mostafa Abedi, Gianluca Levi, Elisa Biasin, Martin M. Nielsen, et al. "Theoretical Evidence of Solvent-Mediated Excited-State Dynamics in a Functionalized Iron Sensitizer". In: *J. Phys. Chem. C* 123.4 (2019), pp. 2056–2065. DOI: 10.1021/acs.jpcc.8b10768 (cit. on p. 22).

[47] Yamen Al-Salka, Luis I. Granone, Wegdan Ramadan, Amer Hakki, Ralf Dillert, et al. "Iron-based Photocatalytic and Photoelectrocatalytic Nano-structures: Facts, Perspectives, and Expectations". In: *Appl. Catal. B* 244 (2019), pp. 1065–1095. DOI: 10.1016/j.apcatb.2018.12.014 (cit. on p. 22).

[48] Latévi Max Lawson Daku, Alfredo Vargas, Andreas Hauser, Antony Fouqueau, and Mark Earl Casida. "Assessment of Density Functionals for the High-Spin/Low-Spin Energy Difference in The Low-Spin Iron(II) Tris(2,2'-bipyridine) Complex". In: *Chemphyschem* 6 (2005), pp. 1393–1410. DOI: 10.1002/cphc.200400584 (cit. on p. 22).

[49] Robert M. Berger and David R. McMillin. "Ultraviolet and Visible Resonance Raman Spectroscopy of tris-(2,2'-bipyridyl) Iron(II): Intensity Considerations and Band Assignments". In: *Inorg. Chim. Acta* 177 (1990), pp. 65–69. DOI: 10.1016/S0020-1693(00)91911-X (cit. on p. 22).

[50] Paul S. Braterman, Jae-Inh Song, and Robert D. Peacock. "Electronic Absorption Spectra of the Iron(II) Complexes of 2,2'-Bipyridine, 2,2'-Bipyrimidine, 1,10-Phenanthroline, and 2,2':6',2"-Terpyridine and their Reduction Products". In: *Inorg. Chem.* 31 (1992), pp. 555–559. DOI: 10.1021/ic00030a006 (cit. on p. 23).

[51] Carmen Sousa, Coen de Graaf, Andrii Rudavskyi, Ria Broer, Jorg Tatchen, et al. "Ultrafast Deactivation Mechanism of the Excited Singlet in the Light-Induced Spin Crossover of $[Fe(2,2\text{-bipyridine})_3]^{2+}$". In: *Chem. Eur. J.* 19.51 (2013), pp. 17541–17551. DOI: 10.1002/chem.201302992 (cit. on p. 23).

[52] Kaili Zhang, Ryan Ash, Gregory S. Girolami, and Josh Vura-Weis. "Tracking the Metal-Centered Triplet in Photoinduced Spin Crossover of $Fe(phen)_{32}^{+}$ with Tabletop Femtosecond M-Edge X-ray Absorption Near-Edge Structure Spectroscopy". In: *J. Am. Chem. Soc.* 141 (2019), pp. 17180–17188. DOI: 10.1021/jacs.9b07332 (cit. on p. 23).

[53] James K. McCusker, Kevin N. Walda, Robert C. Dunn, John D. Simon, Douglas Magde, et al. "Subpicosecond ^{1}MLCT $\rightarrow$ $^5T_2$ Intersystem Crossing of Low-Spin Polypyridyl Ferrous Complexes". In: *J. Am. Chem. Soc.* 115.1 (1993), pp. 298–307. DOI: 10.1021/ja00054a043 (cit. on p. 23).

[54] Alexandre Moguilevski, Martin Wilke, Gilbert Grell, Sergey I. Bokarev, Saadullah G. Aziz, et al. "Ultrafast Spin Crossover in $[Fe^{II}(bpy)_3]^{2+}$: Revealing Two Competing Mechanisms by Extreme Ultraviolet Photoemission Spectroscopy". In: *Chem. Phys. Chem.* 18 (2017), pp. 465–469. DOI: 10.1002/cphc.201601396 (cit. on pp. 23, 24).

[55] Satoru Iuchi and Nobuaki Koga. "Ultrafast Electronic Relaxation in Aqueous $[Fe(bpy)_3]^{2+}$: A Surface Hopping Study". In: *J. Phys. Chem. Lett.* 14.18 (2023), pp. 4225–4232. DOI: 10.1021/acs.jpclett.3c00686 (cit. on p. 23).

[56] A. Messerschmidt, R. Huber, T. Poulos, and K. Wieghardt, eds. *Handbooks of metalloproteins*. Vol. 1. John Wiley and Sons, 2001 (cit. on p. 27).

[57] L. W. Chung, Xi Li, and K. Morokuma. "Modeling Enzymatic Reactions in Metalloenzymes and Photobiology by Quantum Mechanics (QM) and Quantum Mechanics/Molecular Mechanics (QM/MM) Calculations". In: ed. by C. F. Matta. Quantum Biochemistry. Wiley–VCH Verlag GmbH, 2010. Chap. 3. DOI: 10.1002/9783527629213.ch3 (cit. on p. 27).

[58] A. Ansari, J. Berendzen, S. F. Bowne, H. Frauenfelder, I. E. T. Iben, et al. "Protein states and proteinquakes". In: *Proc. Natl. Acad. Sci. USA* 82 (1985), pp. 5000–5004. DOI: 10.1073/pnas.82.15.5000 (cit. on p. 27).

[59] T. R. Barends, L. Foucar, A. Ardevol, K. Nass, A. Aquila, et al. "Direct observation of ultrafast collective motions in CO myoglobin upon ligand dissociation". In: *Science* 350 (2015), pp. 445–450. DOI: 10.1126/science.aac5492 (cit. on pp. 27, 30).

[60] M. Levantino, G. Schiro, H. T. Lemke, and G. Cottone. "Ultrafast myoglobin structural dynamics observed with an X–ray free–electron laser". In: *Nat. Comm* 6 (2015), p. 6772. DOI: 10.1038/ncomms7772 (cit. on pp. 27, 30, 34).

[61] M. Levantino, H. T. Lemke, G. Schiro, M. Glownia, A. Cupane, et al. "Observing heme doming in myoglobin with Femtosecond X–ray absorption spectroscopy". In: *Struc. Dynam.* 2 (2015), p. 041713. DOI: 10.1063/1.4921907 (cit. on pp. 27, 30).

[62] J. N. Harvey. "DFT Computation of the Intrinsic Barrier to CO Geminate Recombination with Heme Compounds". In: *J. Am. Chem. Soc.* 122 (2000), pp. 12401–12402. DOI: 10.1021/ja005543n (cit. on pp. 27, 30).

[63] T. G. Spiro and P. M. Kozlowski. "Is the CO Adduct of Myoglobin Bent, and Does it Matter?" In: *Acc. Chem. Res.* 34 (2001), pp. 137–144. DOI: 10.1021/ar000108j (cit. on p. 27).

[64] C. Rovira, B. Schulze, M. Eichinger, J. D. Evanseck, and M. Parrinello. "Influence of the Heme Pocket Conformation on the Structure and Vibrations of the Fe–CO Bond in Myoglobin: A QM/MM Density Functional Study". In: *Biophys. J.* 81 (2001), pp. 435–445. DOI: 10.1016/S0006-3495(01)75711-6 (cit. on p. 27).

[65] J. N. Harvey. "Spin–forbidden CO ligand recombination in myoglobin". In: *Faraday Discuss.* 127 (2004), pp. 165–177. DOI: 10.1039/B314768A (cit. on p. 27).

[66] C. Meier. "Laser control of vibrational excitation in carboxyhemoglobin: a quantum wavepacket study". In: *J. Chem. Phys.* 123 (2005), p. 044504. DOI: 10.1063/1.1946737 (cit. on p. 27).

[67] Arunangshu Debnath, Cyril Falvo, and Cristoph Meier. "State-selective excitation of the CO stretch in carboxyhemoglobin by mid-IR laser pulse shaping: a theoretical investigation". In: *J. Phys. Chem. A* 117 (2013), pp. 12884–12888. DOI: 10.1021/jp410473u (cit. on p. 27).

[68] O. Kuhn. "Multidimensional vibrational quantum dynamics of CO-heme compounds: ultrafast IVR mediated Fe-CO bond–breaking after CO excitation?" In: *Chem. Phys. Lett.* 402 (2005), pp. 48–53. DOI: 10.1016/j.cplett.2004.12.012 (cit. on p. 27).

[69] A. Waleh and G. H. Loew. "Quantum Mechanical Studies of the Photodissociation of Carbonylheme Complexes". In: *J. Am. Chem. Soc.* 104 (1982), pp. 2346–2351. DOI: 10.1021/ja00373a002 (cit. on p. 27).

[70] A. Dreuw, B. D. Dunletz, and M. Head–Gordon. "Characterization of the Relevant Excited States in the Photodissociation of CO–Ligated Hemoglobin and Myoglobin". In: *J. Am. Chem. Soc.* 124 (2002), pp. 12070–12071. DOI: 10.1021/ja026916i (cit. on pp. 27, 29).

[71] F. De Angelis, R. Car, and T. G. Spiro. "Role of Ligand Bending in the Photodissociation of O_2 vs CO–heme: a Time–Dependent Density Functional Study". In: *J. Am. Chem. Soc.* 125 (2003), pp. 15710–15711. DOI: 10.1021/ja037373v (cit. on p. 27).

[72] T. Ohta, B. Pal, and T. Kitagawa. "Excited State Property of Hardly Photodissociable Heme–CO Adduct Studied By Time–Dependent Density Functional Theory". In: *J. Phys. Chem. B* 109 (2005), pp. 21110–21117. DOI: 10.1021/jp052158h (cit. on p. 27).

[73] B. D. Dunietz, A. Dreuw, and M. Head–Gordon. "Initial Steps of the Photodissociation of the CO Ligated Heme Group". In: *J. Phys. Chem. B* 107 (2003), pp. 5623–5629. DOI: 10.1021/jp0226376 (cit. on pp. 27, 29).

[74] J Halden and S. J. Lorrain. "The Oxygen Tension of Arterial Blood". In: *J. Physiol.* 20 (1896), pp. 497–520. DOI: 10.1113/jphysiol.1896.sp000634 (cit. on p. 27).

[75] S. Franzen, L. Kiger, C. Poyart, and J. Martin. "Heme photolysis occurs by ultrafast excited state metal–to–ring charge transfer". In: *Biophys. J.* 80 (2001), p. 2372. DOI: 10.1016/S0006-3495(01)76207-8 (cit. on pp. 27, 30, 31).

[76] J. W. Petrich, C. Poyart, and J. L. Martin. "Photophysics and Reactivity of Heme Proteins: A Femtosecond Absorption Study of Hemoglobin, Myoglobin, and Protoheme". In: *Biochem.* 27 (1988), pp. 4049–4060. DOI: 10.1021/bi00411a022 (cit. on p. 27).

[77] F. Adar, M. Gouterman, and S. Aronowitz. "Fluorescence, Resonance Raman, and Raditionless Decay in Several Hemoproteins". In: *J. Phys. Chem.* 80 (1976), pp. 2184–2191. DOI: 10.1021/j100561a010 (cit. on p. 27).

[78] J. Eng, C. Gourlaouen, E. Gindensperger, and C. Daniel. "Spin-Vibronic Quantum Dynamics for Ultrafast Excited-State Processes". In: *Acc. Chem. Res.* 48 (2015), pp. 809–817. DOI: 10.1021/ar500369r (cit. on p. 28).

[79] M. Pápai, T. J. Penfold, and K. B. Moller. "Effect of tert-Butyl Functionalization on the Photoexcited Decay of a Fe(II)-N-Heterocyclic Carbene Complex". In: *J. Phys. Chem. C* 120 (2016), pp. 17234–17241. DOI: 10.1021/acs.jpcc.6b05023 (cit. on p. 28).

[80] Nicholas Engel, Sergey I. Bokarev, Alexandre Moguilevski, Azhr A. Raheem, Ruba Al-Obaidi, et al. "Light-induced relaxation dynamics of the ferricyanide ion revisited by ultrafast XUV photoelectron spectroscopy". In: *Phys. Chem. Chem. Phys.* 19 (2017), pp. 14248–14255. DOI: 10.1039/C7CP01288H (cit. on p. 28).

[81] T. Mizutani Y .and Kitagawa. "Direct Observation of Cooling of Heme Upon Photodissociation of Carbonmonoxy Myoglobin". In: *Science* 278 (1997), pp. 443–446. DOI: 10.1126/science.278.5337.443 (cit. on p. 30).

[82] I. Bersuker. *The Jahn-Teller Effect and Vibronic Interactions in Modern Chemistry*. Ed. by J. P. Fackler Jr. Modern Inorganic Chemistry. Springer Verlag, 1984 (cit. on p. 31).

[83] I. Bersuker. "Pseudo-Jahn-Teller Effect–A Two-State Paradigm in Formation, Deformation, and Transformation of Molecular Systems and Solids". In: *Chem. Rev.* 113 (2013), pp. 1351–1390. DOI: 10.1021/cr300279n (cit. on p. 31).

[84] Miquel Huix-Rotllant and Nicolas Ferr'e. "An Effective Procedure for Analyzing Molecular Vibrations in Terms of Local Fragment Modes". In: *Journal of Chemical Theory and Computation* 12.10 (2016), pp. 4768–4777. DOI: 10.1021/acs.jctc.6b00514 (cit. on pp. 35, 40, 50).

[85] Karno Schwinn, Nicolas Ferr'e, and Miquel Huix-Rotllant. "Analytic QM/MM atomic charge derivatives avoiding the scaling of coupled perturbed equations with the MM subsystem size". In: *The Journal of Chemical Physics* 151.4 (2019), p. 041102. DOI: 10.1063/1.5115125 (cit. on pp. 35, 37, 50).

[86] Karno Schwinn, Nicolas Ferr'e, and Miquel Huix-Rotllant. "UV-visible absorption spectrum of FAD and its reduced forms embedded in cryptochrome protein". In: *Phys. Chem. Chem. Phys.* (2020), pp. 12447–12455. DOI: 10.1039/D0CP01714K (cit. on pp. 35, 37, 41).

[87] Miquel Huix-Rotllant and Nicolas Ferr'e. "Analytic Energy, Gradient, and Hessian of Electrostatic Embedding QM/MM Based on Electrostatic Potential-Fitted Atomic Charges Scaling Linearly with the MM Subsystem Size". In: *Journal of Chemical Theory and Computation* 17.1 (2021). PMID: 33284620, pp. 538–548. DOI: 10.1021/acs.jctc.0c01075 (cit. on pp. 35, 41).

[88] Adolfo Bastida, Miguel A. Soler, José Zúñiga, Alberto Requena, Adrián Kalstein, et al. "Molecular Dynamics Simulations and Instantaneous Normal Mode Analysis of the Vibrational Relaxation of the C H Stretching Modes of N methylacetamide d in Liquid Deuterated Water". In: *The Journal of Physical Chemistry A* 114 (2010), pp. 11450–11461. DOI: 10.1021/jp106998h (cit. on p. 35).

[89] Simone Bonfrate, Nicolas Ferré, and Miquel Huix-Rotllant. "An efficient electrostatic embedding QM/MM method using periodic boundary conditions based on particle-mesh Ewald sums and electrostatic potential fitted charge operators". In: *The Journal of Chemical Physics* 158.2 (2023). DOI: 10.1063/5.0133646 (cit. on p. 35).

[90] Simone Bonfrate, Nicolas Ferré, and Miquel Huix-Rotllant. "Analytic gradients for the electrostatic embedding QM/MM in periodic boundary conditions using particle-mesh Ewald sums and electrostatic potential fitted charge operators". In: *Journal of Chemical Theory and Computation* 20 (2024), pp. 4338–4349. DOI: 10.1021/acs.jctc.4c00201 (cit. on pp. 35, 46, 47).

[91] Nicolas Ferré and János G. Ángyán. "Approximate electrostatic interaction operator for QM/MM calculations". In: *Chem. Phys. Lett.* 356 (2002), pp. 331–339. DOI: 10.1016/S0009-2614(02)00343-3 (cit. on p. 35).

[92] Alessandro Laio, Joost VandeVondele, and Ursula Rothlisberger. "D-RESP: Dynamically Generated Electrostatic Potential Derived Charges from Quantum Mechanics/Molecular Mechanics Simulations". In: *The Journal of Physical Chemistry B* 106.29 (2002), pp. 7300–7307. DOI: 10.1021/jp0143138 (cit. on p. 36).

[93] Karno Schwinn, Nicolas Ferré, and Miquel Huix-Rotllant. "Efficient Analytic Second Derivative of Electrostatic Embedding QM/MM Energy: Normal Mode Analysis of Plant Cryptochrome". In: *Journal of Chemical Theory and Computation* 16.6 (2020), pp. 3816–3824. DOI: 10.1021/acs.jctc.9b01145 (cit. on pp. 37, 41, 50).

[94] Miquel Huix-Rotllant, Karno Schwinn, and Nicolas Ferr'e. "Infrared spectroscopy from electrostatic embedding QM/MM: local normal mode analysis of infrared spectra of arabidopsis thaliana plant cryptochrome". In: *Phys. Chem. Chem. Phys.* 23 (2021), pp. 1666–1674. DOI: 10.1039/D0CP06070D (cit. on p. 37).

[95] J. A. Pople, R. Krishnan, H. B. Schlegel, and J. S. Binkley. "Derivative studies in Hartree-Fock and Moller-Plesset theories". In: *International Journal of Quantum Chemistry* 16 (1979), pp. 225–241. DOI: 10.1002/qua.560160825 (cit. on p. 37).

[96] Qiang Cui and Martin Karplus. "Molecular properties from combined QM/MM methods. I. Analytical second derivative and vibrational calculations". In: *The Journal of Chemical Physics* 112 (2000), pp. 1133–1149. DOI: 10.1063/1.480658 (cit. on p. 37).

[97] An Ghysels, H. Lee III Woodcock, Joseph D. Larkin, Benjamin T. Miller, Yihan Shao, et al. "Efficient Calculation of QM/MM Frequencies with the Mobile Block Hessian". In: *Journal of Chemical Theory and Computation* 7 (2011), pp. 496–514. DOI: 10.1021/ct100473f (cit. on p. 37).

[98] E Bright Wilson. *Molecular vibrations*. Dover Books on Chemistry. Dover Publications, 1980 (cit. on p. 39).

[99] Jean Pierre Boon and Michel Kohler. "Calculation of the Dipole Autocorrelation Function for a System of Weakly Coupled Electric Dipoles". In: *The Journal of Chemical Physics* 51 (1969), pp. 3681–3688. DOI: 10.1063/1.1672578 (cit. on p. 40).

[100] Seunghoon Lee, Michael Filatov, Sangyoub Lee, and Cheol Ho Choi. "Eliminating spin-contamination of spin-flip time dependent density functional theory within linear response formalism by the use of zeroth-order mixed-reference (MR) reduced density matrix". In: *The Journal of chemical physics* 149 (2018), p. 104101. DOI: 10.1063/1.5044202 (cit. on p. 41).

[101] Seunghoon Lee, Emma Eunji Kim, Hiroya Nakata, Sangyoub Lee, and Cheol Ho Choi. "Efficient implementations of analytic energy gradient for mixed-reference spin-flip time-dependent density functional theory (MRSF-TDDFT)". In: *J. Chem. Phys.* 150.18 (2019). DOI: 10.1063/1.5086895 (cit. on pp. 41, 42, 53).

[102] Woojin Park, Seunghoon Lee, Miquel Huix-Rotllant, Michael Filatov, and Cheol Ho Choi. "Impact of the Dynamic Electron Correlation on the Unusually Long Excited-State Lifetime of Thymine". In: *J. Phys. Chem. Lett.* 12 (2021), pp. 4339–4346. DOI: 10.1021/acs.jpclett.1c00712 (cit. on pp. 42, 43).

[103] Blake A Erickson, Zachary N Heim, Elisa Pieri, Erica Liu, Todd J Martinez, et al. "Relaxation dynamics of hydrated thymine, thymidine, and thymidine monophosphate probed by liquid jet time-resolved photoelectron spectroscopy". In: *The Journal of Physical Chemistry A* 123 (2019), pp. 10676–10684. DOI: 10.1021/acs.jpca.9b08258 (cit. on p. 43).

[104] Simone Bonfrate, Nicolas Ferré, Miquel, and Huix-Rotllant. "An efficient electrostatic embedding QM/MM method using periodic boundary conditions based on particle-mesh Ewald sums and electrostatic potential fitted charge operators". In: *J. Chem. Phys.* 158 (2023), p. 021101. DOI: 10.1063/5.0133646 (cit. on p. 44).

[105] Peter Pulay. "Analytical derivatives, forces, force constants, molecular geometries, and related response properties in electronic structure theory". In: *Wiley Interdiscip. Rev. Comput. Mol. Sci.* 4 (2014), pp. 169–181. DOI: 10.1002/wcms.1171 (cit. on p. 44).

[106] D. H. Tsai. "The virial theorem and stress calculation in molecular dynamics". In: *J. Chem. Phys.* 70.3 (1979), pp. 1375–1382. DOI: 10.1063/1.437577 (cit. on p. 44).

[107] F. X. Schmid, L. M. Mayr, M. Mucke, and E. R. Schonbrunner. "Prolyl Isomerases: Role in Protein Folding". In: *Adv. Protein Chem.* 44 (1993), pp. 25–66. DOI: 10.1016/S0065-3233(08)60563-X (cit. on p. 46).

[108] R. L. Stein. "Mechanism of Enzymatic and Nonenzymatic Prolyl Cis-Trans Isomerization". In: *Adv. Protein Chem.* 44 (1993), pp. 1–24. DOI: 10.1016/S0065-3233(08)60562-8 (cit. on p. 46).

[109] G. Fischer, H. Bang, and C. Mech. "Nachweis einer Enzymkatalyse fur die cis-trans-Isomerisierung der Peptidbindung in prolinhaltigen Peptiden". In: *Biomed. Biochim. Acta* 43.10 (1984), pp. 1101–1111 (cit. on p. 46).

[110] D. Hamelberg and J. A. McCammon. “Mechanistic Insight into the Role of Transition-State Stabilization in Cyclophilin A”. In: *J. Am. Chem. Soc.* 131.1 (2009), pp. 147–152. DOI: 10.1021/ja806146g (cit. on p. 46).

[111] E. Beausoleil and W. D. Lubell. “Steric Effects on the Amide Isomer Equilibrium of Prolyl Peptides. Synthesis and Conformational Analysis of N-Acetyl-5-tert-butylproline N‘-Methylamides”. In: *J. Am. Chem. Soc.* 118.51 (1996), pp. 12902–12908. DOI: 10.1021/ja962013b (cit. on p. 46).

[112] Y. K. Kang, J. S. Jhon, and S. J. Han. “Conformational study of Ac-Xaa-Pro-NHMe dipeptides: proline puckering and trans/cis imide bond”. In: *J. Pept. Res.* 53.1 (1999), pp. 30–40. DOI: 10.1111/j.1399-3011.1999.tb01614.x (cit. on p. 46).

[113] S. Hur and T. C. Bruice. “The Mechanism of Cis-Trans Isomerization of Prolyl Peptides by Cyclophilin”. In: *J. Am. Chem. Soc.* 124.25 (2002), pp. 7303–7313. DOI: 10.1021/ja020222s (cit. on p. 46).

[114] P. K. Agarwal, A. Geist, and A. Gorin. “Protein Dynamics and Enzymatic Catalysis: Investigating the Peptidyl-Prolyl Cis-Trans Isomerization Activity of Cyclophilin A”. In: *Biochemistry* 43.33 (2004), pp. 10605–10618. DOI: 10.1021/bi0495228 (cit. on p. 46).

[115] Y. K. Kang. “Ab initio and DFT conformational study of proline dipeptide”. In: *J. Mol. Struct. THEOCHEM* 675.1-3 (2004), pp. 37–45. DOI: 10.1016/j.theochem.2003.12.031 (cit. on p. 46).

[116] G. P. Di Martino, M. Masetti, A. Cavalli, and M. Recanatini. “Mechanistic insights into Pin1 peptidyl-prolyl cis-trans isomerization from umbrella sampling simulations”. In: *Proteins* 82.11 (2014), pp. 2943–2956. DOI: 10.1002/prot.24650 (cit. on p. 46).

[117] P. Wapeesittipan, A. S. J. S. Mey, M. D. Walkinshaw, and J. Michel. “Allosteric effects in cyclophilin mutants may be explained by changes in nano-microsecond time scale motions”. In: *Comm. Chem.* 2 (2019), p. 41. DOI: 10.1038/s42004-019-0136-1 (cit. on p. 46).

[118] J. Wang, P. Cieplak, and P. A. Kollman. “How well does a restrained electrostatic potential (RESP) model perform in calculating conformational energies of organic and biological molecules?” In: *J. Comput. Chem.* 21 (2000), pp. 1049–1074. DOI: 10.1002/1096-987X(200009)21:12<1049::AID-JCC3>3.0.CO;2-F (cit. on p. 46).

[119] V. Hornak, R. Abel, A. Okur, B. Strockbine, A. Roitberg, et al. “Comparison of multiple Amber force fields and development of improved protein backbone parameters”. In: *Proteins* 65 (3 2006), pp. 712–725. DOI: 10.1002/prot.21123 (cit. on p. 46).

[120] U. Doshi and D. Hamelberg. "Reoptimization of the AMBER Force Field Parameters for Peptide Bond (Omega) Torsions Using Accelerated Molecular Dynamics". In: *J. Phys. Chem. B* 113 (52 2009), pp. 16590–16595. DOI: 10.1021/jp907388m (cit. on p. 46).

[121] Jessica L. Ramsay, Fabian Schuhmann, Ilia A. Solov'yov, and Daniel R. Kattnig. "Cryptochrome magnetoreception: Time course of photoactivation from non-equilibrium coarse-grained molecular dynamics". In: *Computational and Structural Biotechnology Journal* 26 (2024), pp. 58–69. DOI: 10.1016/j.csbj.2024.11.001 (cit. on p. 48).

[122] Gisela Brändén and Richard Neutze. "Advances and challenges in time-resolved macromolecular crystallography". In: *Science* 373.6558 (2021), eaba0954. DOI: 10.1126/science.aba0954 (cit. on p. 48).

[123] Matteo Levantino, Giorgio Schirò, Henrik Till Lemke, Grazia Cottone, James Michael Glownia, et al. "Ultrafast myoglobin structural dynamics observed with an X-ray free-electron laser". In: *Nature Communications* (2015). DOI: 10.1038/ncomms7772 (cit. on p. 48).

[124] Huiyu Li, Shanshan Wu, and Ao Ma. "Origin of Protein Quake: Energy Waves Conducted by a Precise Mechanical Machine". In: *Journal of Chemical Theory and Computation* 18.9 (2022), pp. 5692–5702. DOI: 10.1021/acs.jctc.2c00514 (cit. on p. 48).

[125] R. J. Dwayne Miller, J. Deak, S. Palese, M. Pereira, L. Richard, et al. "Energy Transduction and Deterministic Protein Motions". In: *Future Directions of Nonlinear Dynamics in Physical and Biological Systems*. Ed. by P. L. Christiansen, J. C. Eilbeck, and R. D. Parmentier. Springer US, 1993, pp. 435–444. DOI: 10.1007/978-1-4899-1609-9_69 (cit. on p. 48).

[126] Scott Habershon and David E. Manolopoulos. "Zero point energy leakage in condensed phase dynamics: An assessment of quantum simulation methods for liquid water". In: *The Journal of Chemical Physics* 131.24 (2009), p. 244518. DOI: 10.1063/1.3276109 (cit. on p. 48).

[127] Johan E. Runeson and David E. Manolopoulos. *Nuclear quantum effects slow down the energy transfer in biological light-harvesting complexes*. 2025. arXiv: 2501.02212 [physics.chem-ph] (cit. on p. 48).

[128] Thomas Fay, Nicolas Ferré, and Miquel Huix-Rotllant. "Efficient Polarizable QM/MM Using the Direct Reaction Field Hamiltonian with Electrostatic Potential Fitted Multipole Operators". In: *J. Chem. Theory Comput.* (2024). DOI: 10.1021/acs.jctc.4c01219 (cit. on p. 48).

[129] Richard A. Friesner. "Solution of self-consistent field electronic structure equations by a pseudospectral method". In: *Chemical Physics Letters* 116 (1985), pp. 39–43. DOI: 10.1016/0009-2614(85)80121-4 (cit. on p. 48).

[130] Frank Neese, Frank Wennmohs, Andreas Hansen, and Ute Becker. "Efficient, approximate and parallel Hartree–Fock and hybrid DFT calculations. A 'chain-of-spheres' algorithm for the Hartree–Fock exchange". In: *Chemical Physics* 356.1 (2009), pp. 98–109. DOI: 10.1016/j.chemphys.2008.10.036 (cit. on p. 48).

[131] Róbert Izsák and Frank Neese. "An overlap fitted chain of spheres exchange method". In: *The Journal of Chemical Physics* 135.14 (2011), p. 144105. DOI: 10.1063/1.3646921 (cit. on p. 48).

[132] Daniel Mejía-Rodríguez, Xiaomin Huang, Jorge M. del Campo, and Andreas M. Köster. "Chapter Four - Hybrid Functionals with Variationally Fitted Exact Exchange". In: ed. by John R. Sabin and Remigio Cabrera-Trujillo. Vol. 71. Advances in Quantum Chemistry. 2015, pp. 41–67. DOI: 10.1016/bs.aiq.2015.03.009 (cit. on p. 48).

[133] Benjamin Helmich-Paris, Bernardo de Souza, Frank Neese, and Róbert Izsák. "An improved chain of spheres for exchange algorithm". In: *The Journal of Chemical Physics* 155 (2021), p. 104109. DOI: 10.1063/5.0058766 (cit. on p. 48).

[134] Thomas Bondo Pedersen, Susi Lehtola, Ignacio Fdez. Galván, and Roland Lindh. "The versatility of the Cholesky decomposition in electronic structure theory". In: *WIREs Computational Molecular Science* 14 (2024), e1692. DOI: 10.1002/wcms.1692 (cit. on p. 48).

[135] Maraia E. Ener, Julia W. Darcy, Fabian S. Menges, and James M. Mayer. "Base-Directed Photoredox Activation of C–H Bonds by PCET". In: *The Journal of Organic Chemistry* 85.11 (2020), pp. 7175–7180. DOI: 10.1021/acs.joc.0c00333 (cit. on p. 49).

[136] Bo Thomsen and Motoyuki Shiga. "Nuclear quantum effects on autoionization of water isotopologs studied by ab initio path integral molecular dynamics". In: *The Journal of Chemical Physics* 154 (2021), p. 084117. DOI: 10.1063/5.0040791 (cit. on p. 49).

[137] Sharon Hammes-Schiffer. "Nuclear–electronic orbital methods: Foundations and prospects". In: *The Journal of Chemical Physics* 155 (2021). DOI: 10.1063/5.0053576 (cit. on p. 49).

[138] Mathew Chow, Eleftherios Lambros, Xiaosong Li, and Sharon Hammes-Schiffer. "Nuclear–Electronic Orbital QM/MM Approach: Geometry Optimizations and Molecular Dynamics". In: *Journal of Chemical Theory and Computation* 19.13 (2023), pp. 3839–3848. DOI: 10.1021/acs.jctc.3c00361 (cit. on p. 49).

[139] Mathew Chow, Tao E. Li, and Sharon Hammes-Schiffer. "Nuclear–Electronic Orbital Quantum Mechanical/Molecular Mechanical Real-Time Dynamics". In: *The Journal of Physical Chemistry Letters* 14.43 (2023), pp. 9556–9562. DOI: 10.1021/acs.jpclett.3c02275 (cit. on p. 49).

[140] Bishnu Thapa and H. Bernhard Schlegel. "Calculations of pKa's and Redox Potentials of Nucleobases with Explicit Waters and Polarizable Continuum Solvation". In: *The Journal of Physical Chemistry A* 119.21 (2015), pp. 5134–5144. DOI: 10.1021/jp5088866 (cit. on p. 49).

[141] Laura Wimberger, Shyamal K. K. Prasad, Martin D. Peeks, Joakim Andréasson, Timothy W. Schmidt, et al. "Large, Tunable, and Reversible pH Changes by Merocyanine Photoacids". In: *Journal of the American Chemical Society* 143.49 (2021), pp. 20758–20768. DOI: 10.1021/jacs.1c08810 (cit. on p. 49).

[142] Kai-Hsin Chang, Yu-Hsuan Yang, Kuan-Hsuan Su, Yi Chen, Ta-Chun Lin, et al. "Light Induced Proton Coupled Charge Transfer Triggers Counterion Directional Translocation". In: *Angewandte Chemie International Edition* 63.23 (2024), e202403317. DOI: 10.1002/anie.202403317 (cit. on p. 50).

[143] Marwa H. Farag, Adolfo Bastida, Manuel F. Ruiz-López, Gérald Monard, and Francesca Ingrosso. "Vibrational Energy Relaxation of the Amide I Mode ofN-Methylacetamide in D2O Studied through Born–Oppenheimer Molecular Dynamics". In: *The Journal of Physical Chemistry B* 118.23 (2014), pp. 6186–6197. ISSN: 1520-5207. DOI: 10.1021/jp500304z (cit. on p. 50).

[144] J. R. Schmidt and John C. Tully. "Path-integral simulations beyond the adiabatic approximation". In: *The Journal of Chemical Physics* 127.9 (2007). DOI: 10.1063/1.2757170 (cit. on p. 51).

[145] Wenjin Li and Ao Ma. "Reaction mechanism and reaction coordinates from the viewpoint of energy flow". In: *The Journal of Chemical Physics* 144 (2016), p. 114103. DOI: 10.1063/1.4943581 (cit. on p. 52).

[146] Huiyu Li and Ao Ma. "Kinetic energy flows in activated dynamics of biomolecules". In: *The Journal of Chemical Physics* 153 (2020), p. 094109. DOI: 10.1063/5.0020275 (cit. on p. 52).

[147] Miles A. Taylor, Liangdong Zhu, Nikita D. Rozanov, Kenneth T. Stout, Cheng Chen, et al. "Delayed vibrational modulation of the solvated GFP chromophore into a conical intersection". In: *Physical Chemistry Chemical Physics* 21 (2019), pp. 9728–9739. DOI: 10.1039/c9cp01077g (cit. on p. 52).

[148] Noriyuki Minezawa and Mark S. Gordon. "Optimizing Conical Intersections by Spin-Flip Density Functional Theory: Application to Ethylene". In: *J. Phys. Chem. A* 113.46 (2009), pp. 12749–12753. DOI: 10.1021/jp908032x (cit. on p. 53).

[149] Miquel Huix-Rotllant, Bhaarathi Natarajan, Andrei Ipatov, C. Muhavini Wawire, Thierry Deutsch, et al. "Assessment of noncollinear spin-flip Tamm–Dancoff approximation time-dependent density-functional theory for the photochemical ring-opening of oxirane". In: *Phys. Chem. Chem. Phys.* 12 (39 2010), pp. 12811–12825. DOI: 10.1039/C0CP00273A (cit. on p. 53).

[150] Max Winslow, Warren B. Cross, and David Robinson. "Comparison of Spin-Flip TDDFT-Based Conical Intersection Approaches with XMS-CASPT2". In: *J. Chem. Theory Comput.* 16.5 (2020), pp. 3253–3263. DOI: 10.1021/acs.jctc.9b00917 (cit. on p. 53).

[151] Woojin Park, Jun Shen, Seunghoon Lee, Piotr Piecuch, Michael Filatov, et al. "Internal Conversion between Bright (11Bu+) and Dark (21Ag–) States in s-trans-Butadiene and s-trans-Hexatriene". In: *J. Phys. Chem. Lett.* 12.39 (2021), pp. 9720–9729. DOI: 10.1021/acs.jpclett.1c02707 (cit. on p. 53).

[152] Seunghoon Lee, Svetlana Shostak, Michael Filatov, and Cheol Ho Choi. "Conical Intersections in Organic Molecules: Benchmarking Mixed-Reference Spin–Flip Time-Dependent DFT (MRSF-TD-DFT) vs Spin–Flip TD-DFT". In: *J. Phys. Chem. A* 123.30 (2019), pp. 6455–6462. DOI: 10.1021/acs.jpca.9b06142 (cit. on p. 53).

[153] Seunghoon Lee, Eunji Kim, Sangyoub Lee, and Cheol Ho Choi. "Fast Overlap Evaluations for Nonadiabatic Molecular Dynamics Simulations: Applications to SF-TDDFT and TDDFT". In: *J. Chem. Theory Comput.* 15.2 (2019), p. 882. DOI: 10.1021/acs.jctc.8b01049 (cit. on p. 53).

[154] Yevhen Horbatenko, Seunghoon Lee, Michael Filatov, and Cheol Ho Choi. "Performance Analysis and Optimization of Mixed-Reference Spin-Flip Time-Dependent Density Functional Theory (MRSF-TDDFT) for Vertical Excitation Energies and Singlet–Triplet Energy Gaps". In: *J. Phys. Chem. A* 123.37 (2019), pp. 7991–8000. DOI: 10.1021/acs.jpca.9b07556 (cit. on p. 53).

[155] Seunghoon Lee, Yevhen Horbatenko, Michael Filatov, and Cheol Ho Choi. "Fast and Accurate Computation of Nonadiabatic Coupling Matrix Elements Using the Truncated Leibniz Formula and Mixed-Reference Spin-Flip Time-Dependent Density Functional Theory". In: *J. Phys. Chem. Lett.* 12 (2021), pp. 4722–4728. DOI: 10.1021/acs.jpclett.1c00932 (cit. on p. 53).

[156] Yong Su Baek, Seunghoon Lee, Michael Filatov, and Cheol Ho Choi. "Optimization of Three State Conical Intersections by Adaptive Penalty Function Algorithm in Connection with the Mixed-Reference Spin-Flip Time-Dependent Density Functional Theory Method (MRSF-TDDFT)". In: *J. Phys. Chem. A* 125.9 (2021), pp. 1994–2006. DOI: 10.1021/acs.jpca.0c11294 (cit. on p. 53).

[157] Vladimir Pomogaev, Seunghoon Lee, Sason Shaik, Michael Filatov, and Cheol Ho Choi. "Exploring Dyson's Orbitals and Their Electron Binding Energies for Conceptualizing Excited States from Response Methodology". In: *J. Phys. Chem. Lett.* 12.40 (2021), pp. 9963–9972. DOI: 10.1021/acs.jpclett.1c02494 (cit. on p. 53).

[158] Yevhen Horbatenko, Seunghoon Lee, Michael Filatov, and Cheol Ho Choi. "How Beneficial Is the Explicit Account of Doubly-Excited Configurations in Linear Response Theory?" In: *J. Chem. Theory Comput.* 17.2 (2021), pp. 975–984. DOI: 10.1021/acs.jctc.0c01214 (cit. on p. 53).

[159] Yevhen Horbatenko, Saima Sadiq, Seunghoon Lee, Michael Filatov, and Cheol Ho Choi. "Mixed-Reference Spin-Flip Time-Dependent Density Functional Theory (MRSF-TDDFT) as a Simple yet Accurate Method for Diradicals and Diradicaloids". In: *J. Chem. Theory Comput.* 17.2 (2021), pp. 848–859. DOI: 10.1021/acs.jctc.0c01074 (cit. on p. 53).

[160] Heechan Kim, Woojin Park, Younghun Kim, Michael Filatov, Cheol Ho Choi, et al. "Relief of excited-state antiaromaticity enables the smallest red emitter". In: *Nat. Commun.* 12.1 (2021), pp. 1–9. DOI: 10.1038/s41467-021-25677-2 (cit. on p. 53).

[161] Seunghoon Lee, Woojin Park, Hiroya Nakata, Michael Filatov, and Cheol Ho Choi. "Recent advances in ensemble density functional theory and linear response theory for strong correlation". In: *Bull. Korean Chem. Soc.* 43.1 (2022), pp. 17–34. DOI: 10.1002/bkcs.12429 (cit. on p. 53).

[162] Achini Japahuge, Seunghoon Lee, Cheol Ho Choi, and Tao Zeng. "Design of singlet fission chromophores with cyclic (alkyl)(amino) carbene building blocks". In: *J. Chem. Phys.* 150.23 (2019), p. 234306. DOI: 10.1063/1.5099062 (cit. on p. 53).

[163] Ekadashi Pradhan, Seunghoon Lee, Cheol Ho Choi, and Tao Zeng. "Diboron- and diaza-doped anthracenes and phenanthrenes: their electronic structures for being singlet fission chromophores". In: *J. Phys. Chem. A* 124.40 (2020), pp. 8159–8172. DOI: 10.1021/acs.jpca.0c06915 (cit. on p. 53).

[164] Dylan James, Ekadashi Pradhan, Seunghoon Lee, Cheol Ho Choi, and Tao Zeng. "Dicarbonyl anthracenes and phenanthrenes as singlet fission chromophores". In: *Can. J. Chem.* 99.999 (2022), pp. 1–10. DOI: 10.1139/cjc-2021-0241 (cit. on p. 53).

[165] Konstantin Komarov, Woojin Park, Seunghoon Lee, Tao Zeng, and Cheol Ho Choi. "Accurate Spin–Orbit Coupling by Relativistic Mixed-Reference Spin-Flip-TDDFT". In: *J. Chem. Theory Comput.* (2023). DOI: 10.1021/acs.jctc.2c01036 (cit. on p. 53).

[166] Woojin Park, Konstantin Komarov, Seunghoon Lee, and Cheol Ho Choi. "Mixed-Reference Spin-Flip Time-Dependent Density Functional Theory: Multireference Advantages with the Practicality of Linear Response Theory". In: *J. Phys. Chem. Lett.* 14 (2023), pp. 8896–8908. DOI: 10.1021/acs.jpclett.3c02296 (cit. on p. 53).

[167] Seunghoon Lee, Woojin Park, and Cheol Ho Choi. "Expanding Horizons in Quantum Chemical Studies: The Versatile Power of MRSF-TDDFT". In: *Acc. Chem. Res.* (2025), pp. 104101–8908. DOI: 10.1021/acs.accounts.4c00640 (cit. on p. 53).

[168] Miquel Huix-Rotllant, Woojin Park, and Cheol Ho Choi. “Assessing Spin-flip Time-Dependent Density-Functional Based Tight-Binding For Describing Photoisomerisation Reactions”. In: *Theoretical Chemistry Accounts* (2025) (cit. on p. 53).